Synthesis and Characterization of Advanced Nuclear Fuels

Synthesis and Characterization of Advanced Nuclear Fuels

Proefschrift

ter verkrijging van de graad van doctor

aan de Technische Universiteit Delft,

op gezag van de Rector Magnificus prof. ir. K.C.A.M. Luyben,

voorzitter van het College voor Promoties,

in het openbaar te verdedigen op 02 dag juni 2014 om 12.30 uur

door

Ursula CARVAJAL NUÑEZ

Master of Science in Material Engineering, Universidad Complutense de Madrid

geboren te Madrid, Spain

Dit proefschrift is goedgekeurd door de promotor:

Prof. dr. R.J.M. Konings

Samenstelling promotiecommissie:

Rector Magnificus,	voorzitter
Prof. dr. R.J.M. Koning,	Technische Universiteit Delft, promotor
Prof.dr. F. Livens,	University of Manchester, Verenigd Koninkrijk
Prof.dr. N. Dacheaux,	University of Montpellier, Frankrijk
Prof.dr. H.T. E.H. Brück,	Technische Universiteit Delft
Prof.dr. H.T. Wolterbeek,	Technische Universiteit Delft
Dr. Ir. J.L. Kloosterman,	Technische Universiteit Delft
Dr. J. Somers,	Joint Research Center, Duitsland

Keywords: Nuclear fuel, XRD, NMR, XAS, sol-gel, melting point.

Contents

Chapter 6

Coupling XRD, EXAFS and 13C NMR to Study the Effect of the Carbon Stoichiometry on the Local Structure of UC1±x. **79**

Chapter 7

Chapter 8

Hoofdstuk 8

Chapter 1

Introduction

Over the decades, economic and political priorities change continuously and currently have led to a renewed interest in the commercial fast reactor technology [1]. There are many reasons and in particular, this can be understood by considering the rapid increase of the world´s energy consumption, the low contribution of the nuclear energy to the greenhouse effect, the limited uranium resources, the growth of the spent nuclear fuel (SNF) stock and the global pressure to reduce the life time, and potential environmental impact, of the highly radioactive wastes. These aspects have been reinforced since the accident at Fukushima and the emphasis on the safety of nuclear reactors and nuclear fuel cycle operations has been enhanced considerably.

Spent nuclear fuel is the primary waste resulting from the production of nuclear energy. It is composed of 94% of uranium and 1% of plutonium. Since these elements are valuable energy bearing resources, they can be recycled through the irradiation of uranium-plutonium mixed oxides (MOX) fuels. The remaining 5% of the SNF is composed of 4.9% of fission products (^{129}I, ^{99}Tc, ^{93}Zr, ^{135}Cs, etc.) and 0.1% of minor actinides (MAs) such as Np, Am and Cm. The latter elements are created in the reactors by successive neutron capture, and α and β decays. Although the MAs represent only 0.1% of the SNF, they are the major contributor, after Pu, to the long term radiotoxic inventory of the spent fuel (see Figure 1.1). Amongst the MAs, Am is the major contributor to the radiotoxicity [2]. For this reason, the management of the MAs, and especially of Am, is of inordinate importance, if the potential long term risk of these elements is to be abated.

1
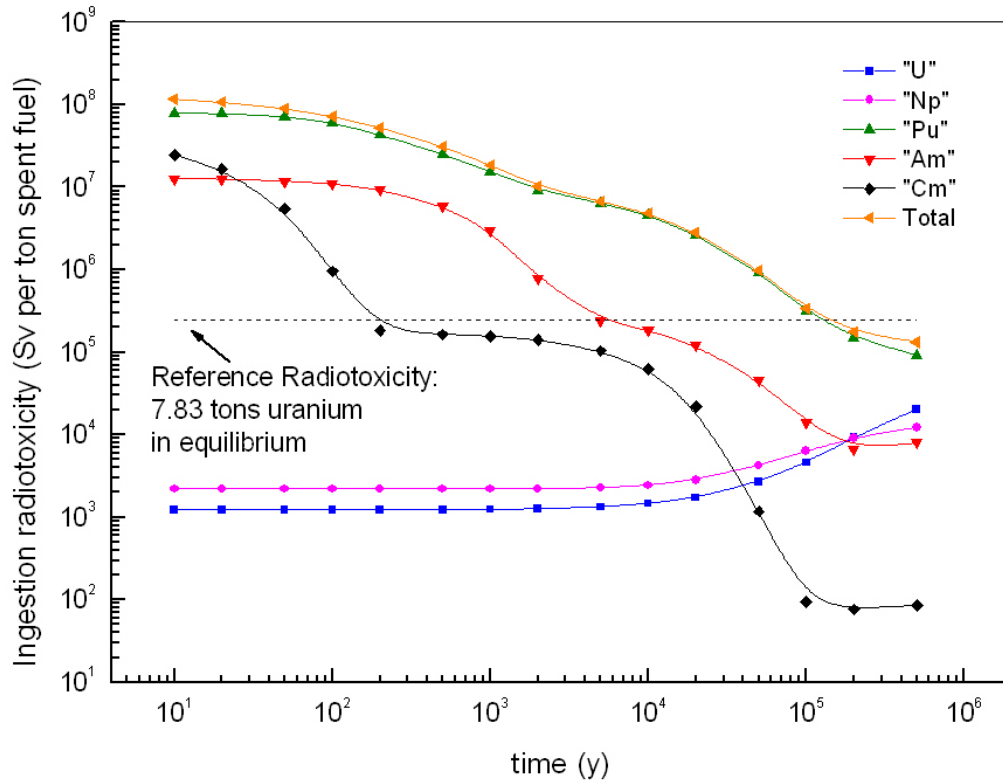
Figure 1.1: Time evolution of the radiotoxicity of the actinides in high-level wastes.

Currently, there are four strategies foreseen for the management of spent nuclear fuel:

I.   Deep geological disposal;

The first alternative consists in isolating the SNF within a stable geologic host rock formation such as salt rock, granite, or clay, etc. No release to the environment over long time frames must be ensured. Deep geological disposal has not been fully implemented in any country (although Finland and Sweden have identified sites and approved construction for such facilities).

II.   Storage and postponed decision;

The second option involves intermediate storage of the SNF and postponing a decision on the fate of the waste. This policy relies on nuclear technology progressing towards alternative options as proposed in the Generation IV initiative which not only tackles sustainability, but also the management of wastes by recycling and transmutation.

III.   Reprocessing;

In this strategy, the SNF is reprocessed to recover fissile materials (i.e. the U and Pu), which can be used to fuel current and future nuclear power plants. Reprocessing has its technical and political issues. A highly equipped and safe facility is required to ensure no releases to the environment. The processes can be complicated and expensive, and even though significant volume reductions, e.g. in the form of glass, can be achieved, additional intermediate level waste requires disposal too. Finally, all reprocessing plants are subjected to strict safeguards controls to ensure no potential misuse of the recovered materials, or even the facility itself.

The use of a fast neutron reactor can be a component a reprocessing programme. They can be designed to breed fuel as fast, or even faster, than they burn it. They can also be designed and configured to efficiently burn plutonium and other minor actinides.

IV.   Partitioning and transmutation (P&T)

The P&T strategy takes basic reprocessing one step further, in that it consists of the separation of the MAs from the spent fuel, as well as the U and Pu. These elements are then incorporated in a new matrix in order to transmute them in to short lived elements (i.e. fission products) through further irradiation in fast neutron reactors. According to the transmutation scenarios, the long term radiotoxicity of the SNF can be then reduced from 100,000 years down to 300 years. Even if the transmutation efficiency is inferior to 100%, a reduction to 1000 years is reasonable. The transmutation of MAs has a further benefit. Since the MAs contribute significantly to the heat load of spent fuel, their transmutation increases the effective capacity of a repository by at least a factor of 10, and the need for far fewer repositories.

P&T requires the incorporation of MAs, such as Am, in dedicated materials and needs an in depth study [3]. Concentrating on the homogeneous MA recycling in nuclear reactors, small amounts of MAs (up to 5%) are added to conventional (U,Pu) bearing oxide, metal, nitride or carbide fuels. Today, the most commonly used fuels are oxides. While their synthesis routes have been well established and optimized and their performance demonstrated, oxide fuels are not necessarily the most suitable fuels for fast reactor operation.

3

Indeed, the presence of two oxygen atoms per metal atom results in a softer neutron spectrum which, in combination with their poor thermal conductivity, is not necessarily optimal for fast reactor operation. Nitrides and carbides fuels are also potential candidates. They have a high actinide density, good thermal conductivity and high melting point, properties all of which leading to improved safety margins [6]. Table 1.1 summarises and compares some of the characteristics of various types of advanced nuclear fuels [6-9]. The higher metal density improves core characteristics, such as doubling time. At low linear power, both oxide and metallic fuels operate at about 80% of their melting point. In contrast, carbide and nitride fuels operate at about 40% of their melting point [7-9]. Thus, nitride and carbide fuels operating at higher power could improve the economics of the reactor operation. Despite their favourable margin to melt, neither carbide nor nitride have been developed on a large scale, mainly due to the difficulty in fabrication and less well studied and understood irradiation performance. An exception is the experience in India (Ganguly *et al* [10]) where carbide fuel was used for the operation of the test fast reactor at Kalpakkam.

Table 1.1: Intercomparison of some of the properties and experience of MOX, MC, MN and metallic fuels (M= U, Pu) [6-9].

	Selected fuel properties of uranium-plutonium mixed fuels			
	Metal	**Oxide**	**Nitride**	**Carbide**
Theoretical density (g.cm^{-3})	15.73	11.04	14.32	13.58
Metal density (g.cm^{-3})	14.10	9.80	13.50	12.96
Melting point (K)	1400	3023	3070	2750
Thermal conductivity, λ (W m^{-1} K^{-1})				
1000 K	25	2.6	15.8	18.8
2000 K		2.4	20.1	21.2
Breeding ratio	1.35-1.4	1.1-1.15	1.2-1.25	1.2-1.25
Swelling	High	High	Moderate	Moderate
Handling	Inert atmosphere	Inert atmosphere	Inert atmosphere	Inert atmosphere
Dissolution and reprocessing amenability	Pyro-processing demonstrated on pilot plant scale	Demonstrated on industrial scale for aqueous and pilot scale for pyroprocess	Dissolution easy but risk of C^{14} in reprocessing	Process not yet demonstrated on industrial scale
Fabrication/irradiation experience	Moderate	Large	Very little	Limited

Different techniques have been used for the synthesis of MC and MN (M= U, Pu) [9,10]. The methods of synthesis are similar because the MC and MN compounds both exhibit the "rock salt" structure. In contrast to oxides, several issues complicate their production:

➢ More processes steps are required as the carbide and nitride must be synthesised.

➢ The synthesis must be carried out inside leak tight glove boxes under inert gas because their oxidation susceptibility and pyrophoricity risk is high.

➢ Tight control of the carbon and nitride content is needed to prevent the formation of higher nitrides and carbides (e.g. MN_2, M_2N_3 and MC_2, M_2C_3).

➢ In the final product, light element (C, N, and O) impurities are higher compared to oxides.

The main methods to synthesise MC and MN are:

➢ Direct synthesis by arc-melting (for low quantities of fuels at laboratory scale).

➢ Direct nitration or carburisation of the metal, involving hydriding-dehydriding of bulk metal (to form fine metal powder) followed by carburization and nitridation with methane/propane or nitrogen for obtaining fine powders of MC and MN, respectively.

➢ Carbothermal reduction-powder metallurgy of metal oxide-carbon mixtures in vacuum/argon and flowing nitrogen for MC and MN, respectively.

The most studied route has been the carbothermal reduction of oxides as it is the most suited for large scale production. The homogenization of the precursor powders is achieved either by a "dry method", i.e. prolonged milling and blending of the oxide and carbon followed by carbothermal reduction, further communition, and compaction and sintering steps to obtain the final product. Alternatively a "wet chemical route", mainly known as the "sol-gel" process can be deployed to replace the powder metallurgy steps. In this route, microspheres (100-200 μm) of oxide plus carbon are prepared from the nitrate solution of uranium and plutonium by external or internal gelation processes. The Paul Scherrer Institut (PSI), in Switzerland, has been the pioneer for the synthesis of (U,Pu)C and (U,Pu)N microspheres by internal gelation [11].

5

The advantages of sol-gel solution processing (either internal or external) routes include:

➢ No dusts produced, thus reducing the radiotoxicity hazard and pyrophoricity risk.

➢ Automation and remote operation facilitated by free flowing spheres.

➢ Less fabrication steps required.

➢ Excellent nano-homogeneity of U and Pu, as the starting point was a nitrate solution of these two elements.

A full optimization of the synthesis parameters (C/U ratio, temperature and time for the carbothermal reduction) has never been established, and as one deals with solutions, this optimization is not at all trivial. High purity of the final compound is the target, and is determined to a large extent on the degree of homogeneity in the starting oxide-carbon mixture.

The difficulty in the synthesis of nitrides and carbides containing MAs is even greater and experimental data on such compounds are almost non-existent. In general, there is no industrial scale experience in the synthesis of high MAs bearing fuels (oxide, nitrides, carbides, non-metal) specifically designed for transmutation, and indeed only a handful of studies on the synthesis of MAs bearing the nitrides at laboratory scale, and none at all for the corresponding MAs bearing carbides.

The structure, the thermophysical properties and irradiation resistance are key components influencing the performance of fuels in nuclear reactors. Understanding the structure and the effect of the behaviour at high temperature is crucial to predict the safety margins for their behaviour in pile.

MN and MC compounds belong to the same family on the basis of their crystal structure (face centered cubic (fcc), NaCl) and they have similar physical and chemical properties. The mixed metal MN and MC of uranium and plutonium show complete solid solubility. Despite the significant studies on MN and MC fuels (M= U,Pu), it remains very

limited compared to oxides. Thus, some of the properties have been not well explained nor understood as a consequence of the highly dissipated data and poorly correlated data [12].

Regarding the fuel design and its safety during operation, experimental data on out-of-pile properties such a melting point, thermal conductivity, thermal expansion are essential. The variables that influence such properties of fuel are its composition, reaction temperature (T), density, microstructure and stoichiometry (O/M, C/M, and N/M) of fuels. These variables change also with irradiation. For this reason, their knowledge in pristine state and evolution during irradiation is essential for fuel design and safety analysis.

To evaluate the thermal performance of the fuel, their melting point and the thermal conductivity are needed. These properties play a crucial role in determining the power to melt of the fuel and are decisive in the selection of the operating linear heat rating of the fuel during irradiation. The melting point and thermal conductivity depend intrinsically on the fuel composition and stoichiometry, and can be modified when fission products are formed. They also change during irradiation, not just by the presence of fission products, but also by irradiation damage, and the formation of defects, porosity, fission-gas bubbles. Finally the evolution of chemical composition and the stoichiometry with irradiation also influence the safety of the fuel. These changes in the thermal conductivity affect the temperature profile across the fuel pellet radius, which directly influences important processes such as fission gas release, swelling, grain growth, which in turn may limit the linear power.

1.1.   *Motivation for the research conducted in this thesis*

Despite the Fukushima accident, nuclear energy remains an important component in the European energy mix and it also represents a significant contribution covering worldwide energy needs. As indicated above, improved strategies addressing issues concerning spent nuclear fuel (SNF) are needed and supplied by partitioning and transmutation, where MAs are recycled in nuclear reactors to decrease the long term radiotoxicity of the SNF. Research and development of fuels is essential for a better understanding of the phenomena occurring under irradiation, ultimately to prevent severe accidents.

Although, a considerable effort has been made to prepare and characterize actinide nitrides and carbides in the past, the issue of MAs incorporation in such fuels was poorly explored. Moreover, it is clear that much stronger attention must be paid to research associated with their operational safety.

The goal of this research was and is to make a significant contribution to the understanding of the basic properties of the nitrides and carbides by synthesising them, and by providing new structural and thermodynamic property data on these advanced fuels.

In this framework, a major goal of this thesis has been the synthesis of uranium nitrides and carbides, mixed U, Pu nitrides and carbides, and indeed MA bearing uranium nitrides and carbides at laboratory scale. An arc melting process was used to synthesize high purity $UC_{1\pm x}$, UC_2 and U_2C_3. In addition, UN, (U, Pu)N, (U, Pu)C, have been synthesized using an external gelation process coupled to carbothermal reduction steps and have been optimized for each material. Problems posed by MAs volatilisation during synthesis of nitrides and carbides are known and processes need to be modified to reach the final goal, namely the synthesis of (U,Pu,Am)N and (U,Pu,Am)C. This was achieved using a synthesis based on Am-infiltration of sol-gel produced porous beads [13,14]. Coupling external gelation, infiltration and carbothermal reduction methods, has several advantages, in particular the absence of dust during the preparation of Am fuels, has been achieved. This is an important safety criterion, as radiation dose to operators from dust deposits on the equipment in the glove boxes must be minimised.

The second objective of this work lay in the accurate characterization of the structural and thermophysical properties of these synthesised materials. Thus, the compounds were characterized using X-Ray Diffraction (XRD), X-Ray Absorption Spectroscopy (XAS), Nuclear Magnetic Resonance (NMR) and Raman spectroscopy to determine their short and long range crystallographic order. Ensuring the safety of the fuel during operation requires a precise knowledge of their behaviour at high temperature, and in particular the melting points of these materials were determined by specially adapted and calibrated laser melting measurements. Finally, the study of self-irradiation effects actinide materials provides information on their capability to withstand damage caused by the creation of the fission products or on alpha decay of specific nuclides. For the latter, the recoil atoms produce dense

9

collision cascades of typically 1500 displacements within a short range [15]. Hence, understanding the relation between damage, microstructure and physical properties is of fundamental importance for the fuel performance. The use of advanced techniques and spectroscopy methods providing structural data deepens the basic understanding of the radiation effects in condensed matter and will ultimately lead to the design of materials that are radiation resistant or tolerant. In this framework, the structural evolution of nitride and carbide fuels have been studied on materials stored under inert gas for 25 years.

1.2.   Manuscript layout

This manuscript is divided into eight chapters.

Chapter 2 presents the synthesis of UN by a combination of external gelation and carbothermal reduction methods. The synthesis parameters have been optimized so as to achieve the purest material possible. The local structure of this compound was fully characterized by coupling XRD, XAS and RAMAN measurements.

In Chapter 3, these above optimized synthesis parameters were applied for the preparation of (U, Pu)N and (U, Pu, Am)N. Further, the feasibility of the synthesis at the laboratory scale of Am bearing nitrides has been established. In addition, the structure of these materials has been investigated by XRD.

Chapter 4 describes the melting behaviour of UN and (U, Pu)N, which is an important limiting fuel property in view of reactor applications. Melting temperatures have been achieved using laser melting combined within a self-crucible approach. The incongruent melting of UN was demonstrated by additional post melting XRD. The effect of the Pu addition was also studied.

Chapter 5 deals with the self-irradiation effects that developed during storage in a (U, Pu)N fuel synthesized 25 years ago. Thus, the structural self-irradiation induced changes have been investigated by coupling XRD, XAS and Transmission Electron Microscopy (TEM).

In Chapter 6, the local structure in a series of $UC_{1\pm x}$ (x= 0 and 0.04) samples has been studied combining XRD, NMR and XAS methods. The structure of the $UC_{1\pm x}$ has been accurately assessed and the effect of the non-stoichiometry has been discussed.

Chapter 7 presents a structural study by arc-melting and by XRD, XAS and NMR of UC_2 and U_2C_3. The composition, the purity, the local environments of both U and C atoms as well as the bonds length with the coordination number have been determined.

The results generated here represent a substantial body of work and constitute an important contribution to the knowledge on the synthesis and the characterization of

11

plutonium and americium bearing uranium nitride and carbides fuels. Further, they complement the incomplete literature with detailed structural information on these key compounds

The thesis concludes with a chapter summarising the most important findings (Chapter 8).

1.3.   List of publications

Each chapter constitutes a paper submitted, accepted or already published in a peer reviewed scientific journal. The following list of publications has been arranged according to the submission date.

1. **U. Carvajal-Nuñez** et al., Structure of UC_2 and U_2C_3: XRD, ^{13}C NMR and EXAFS study, Journal of Alloys and Compounds, 589 (2014) 234-239. *Thesis, Chapter 7.*

2. **U. Carvajal-Nunez** et al., Chemical and structural characterization of uranium nitride produced by external gelation. Journal of Nuclear Materials, submitted, 2014. *Thesis, Chapter 2.*

3. **U. Carvajal-Nunez** et al., Melting Point Determination of Uranium Nitride and Uranium Plutonium Nitride: a Laser Heating Study , Journal of Nuclear Materials, in press, 2014. *Thesis, Chapter 4.*

4. **U. Carvajal-Nunez** et al., Preparation and Characterization of (U,Pu)N and (U,Pu,Am)N, Journal of Nuclear Materials, accepted, 2014. *Thesis, Chapter 3.*

5. **U. Carvajal-Nunez** et al., Characterization of self-damaged (U,Pu)N fuel used in the NIMPHE program, Journal of Nuclear Materials, 443 (2013) 491-496. *Thesis, Chapter 5.*

6. **U. Carvajal-Nunez** et al., Coupling EXAFS and ^{13}C NMR to study the effect of carbon content on the local structure of $UC_{1\pm x}$. Inorganic Chemistry, 2013, 52 (19), 11669–11676. *Thesis, Chapter 6.*

7. **U. Carvajal-Nunez** et al., Safety in the synthesis of nitride and carbide fuels. Transactions of the American Nuclear Society. American Nuclear Society-Annual Meeting 2012, Chicago, IL. *Thesis, Chapter 2.*

1.4.   References

[1]   G. Locatelli, M. Mancini, N. Todeschini, Energy Policy, Volume 39, Issue 12, December 2011, pp. 7762-7775.

[2]   D.G. Cacuci, Handbook of Nuclear Engineering. Vol. 5: Fuel Cycles, Decommissioning, Waste Disposal and Safeguards, Springer-Verlag GmbH, 2010.

[3]   R.E. Nightingale, Fast Reactor Nitrides Research, BNWL-842, 1968.

[4]   J.T. Dalton, Equilibria in the system uranium-plutonium-carbon in carbides in Nuclear Energy, L.E. Russell, eds. Proc. Of the Syposium, England, Harwell, Nov., 1963, vol.1, pp 77-94.

[5]   A.E. Ogard, W.C. Pritchard, R.M. Douglass, J.A. Leary, *J. Inorg. Nucl. Chem., 24 (1962) p. 29.*

[6]   A.E. Waltar, D.R. Todd, P.V. Tsvetkov, Fast Spectrum Reactors, Springer, 2011.

[7]   H. Matsui, M. Horiki, T. Kirihara, *J. Nucl. Sci. Technol.. 18 (1981) p. 922.*

[8]   O. Sisman, J.G. Morgan, Irradiation Behaviour of High-Temperature Fuel Materials, 1968.

[9]   F. Le Guyadec, C. Rado, S. Joffre, S. Coullomb, C. Chatillon, E. Blanquet, *J. Nucl. Mater., 393 (2009) p. 333.*

[10] C. Ganguly, P.V. Hegde, A. K. Sengupta, *J. Nucl. Mater., 178 (1991) pp.234–241.*

[11] British Nuclear Fuels Limited (BNFL), Advanced Reactors with Innovative Fuels: Second Workshop Proceedings, Chester, United Kingdom 22-24 October 2001; OECD Publishing, 2002.

[12] K. Richter, in: P. Vincenzini (Ed.), Direct Pressing: A New Method of Fabricating MX Fuels, High Tech Ceramics, Elsevier Science Publishers, Amsterdam, 1987, p. 2841.

[13] M. Vespa, M. Rini, J. Spino, T. Vitova, J. Somers, *J. Nucl. Mater., 421 (2012) p.80.*

[14] A. Fernandez. M. Walter, J. Somers, *internal report, unpublished results.*

[15] A.K. Sengupta, R. Agarwal, H.S. Kamath, in:, Rudy J.M. Konings (Ed.), Comprehensive Nuclear Materials, Elsevier, Oxford, 2012, pp. 55–86.

14

Chapter 2

Chemical and Structural Characterization of Uranium Nitride Produced by External Gelation

ABSTRACT

The determination of the properties of nuclear fuels is central to the Joint Research Centre – Institute for Transuranium Elements (JRC- ITU)´s programmes on the safety of nuclear fuels, and the data produced is used by numerous organisations in the assessment of the operational safety of these fuels. Much progress has been made for oxides, but less for alternative forms such as nitrides and carbides, which are more difficult to prepare in pure form for such property measurements. An improvement in the preparation of these fuels can be achieved by dust-free synthesis routes, especially important for minor actinide applications. Here we describe a sol-gel method using external gelation that avoids the generation of dust. Carbon is dispersed in the precursor oxide particles via a sol-gel external gelation step, which also assists material transport during the solid state reaction to generate the nitride from the oxide by carbothermal reduction. This process has been tested for the synthesis of uranium nitride, and UN with very low amounts of O and C impurities (< 0.07 and 0.2 wt% respectively) have been attained. The local structure of the as-synthesized UN was fully characterized coupling XRD, EXAFS and RAMAN measurements.

2.1.   Introduction

Uranium mononitride (UN) and uranium plutonium nitrides (U,Pu)N are promising candidate fuels for fast nuclear reactors. The properties which make this material so attractive for nuclear applications are among others their higher thermal conductivity compared to uranium dioxide (by approximately a factor of 7 [1]), a higher metal atom density (by 40%) and less moderation (a single counter ion to the metal). However, UN and (U,Pu)N also exhibits some disadvantages linked to its fabrication by carbothermal reduction method, such as its difficulty of achieving a pure compound [2,3], which in the end limits the reliability of all safety relevant property determinations. It is therefore necessary to develop synthesis methods capable of achieving high-purity nitrides reliably and repeatedly. This aspect is particularly important for JRC-ITU's programmes on safety of nuclear fuel, which centre on the determination of safety relevant parameters for their safety assessment. Without high quality samples this goal cannot be reached.

Among the techniques used to produce UN [1], carbothermal reduction has been often employed in the past [4,5,6]. This traditional route has been modified to incorporate direct pressing after carbothermal reduction [7]. The starting material for the carbothermal reduction can be prepared by a sol-gel route [7]. In India (BARC), in Switzerland (PSI), in Germany (JRC- ITU) and in Japan (JAEA) MN fuels have been successfully synthesized via such aqueous processing routes [1-8]. Some of the advantages of this sol-gel solution processing routes are:

➢ No production of dust, which reduces the radiotoxicity hazard and the pyrophoricity risk;

➢ Automation and remote operation facilitated by free flowing spheres;

➢ Limitation of the number of synthesis steps.

In this study, we followed a sol-gel route developed at JRC- ITU [7-9]; the major difference with the past synthesis methods is the use of the external gelation method to induce the precipitation. In contrast, to the internal gelation method [3], this process does not involve a combination of organic and aqueous phases, *i.e.* neither HMTA, UREA nor hot silicone oil

is needed. The liquid waste is decreased significantly. The viscosity of the broth solution containing the metal nitrate salts and carbon is increased through the addition of a polymer (polyvinylalcohol (PVA) or methocel).

In this context, the present study considers improved synthesis of UN by an external sol-gel dust-free route. Chemical analysis methods and Raman spectroscopy have been used to analyse the purity of the final product. Moreover Raman investigations on UN have not been reported in the open literature prior to the current work, at least to the authors´ knowledge. As no UN has been synthesized using this process, a structural characterization based on XRD and EXAFS has also been conducted. The ultimate goal of this work is not just the determination of the safety relevant thermophysical and thermochemical properties of UN and (U,Pu)N, but also (U,Pu,Am)N. The latter is far more challenging and necessitates improvements in the synthesis, to manage the additional radiation risk posed by americium.

2.2. Experimental

2.2.1. Sample preparation

UN was synthesised in the form of beads using an external sol-gel method, developed at JRC ITU [9]. Spherical particles (2-12 μm) of carbon black (99.95% of purity) were included directly in the sol-gel solution to increase its interaction with the oxide precursor and improve its reaction during the subsequent carbothermal reduction under N_2 (see reaction 1) and Ar/H_2 during the cooling to avoid the formation of higher nitrides.

$$UO_2 + 2C + 1/2N_2 \rightarrow UN + 2CO \quad (1)$$
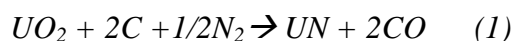
A large size of the particles (50-150 μm) was achieved. A high sol-gel spheres surface reduces their pyrophoricity and their ability to produce dust. Samples of the UO_2+C precursor beads, with a carbon-to-uranium ratio (C/U) of 2.8, were prepared. The inclusion of excess carbon with respect to stoichiometry required for the carbothermal reaction, C/U=2, was necessary to achieve a complete reaction. Essentially, higher carbon contents than stoichiometric provide the best means to remove the oxygen, which could be problematic if the carbon is not uniformly dispersed in the material. After the sol-gel step, calcination under

Ar/H_2 at 800°C during 4 hours was performed to remove the organics (methocel, triton and THFA) from the powder. The carbothermal reduction was conducted under N_2 at 1500°C during 8 hours with a further 2 hours under N_2/H_2 to remove excess carbon. The heating and cooling (the latter under Ar/H_2) rates were equal to 200°C/h. The progress of the reaction was monitored and recorded by the CO content in the exhaust gas in a device installed at the furnace.

2.2.2.   *Sample characterization*

The carbon, oxygen and nitrogen contents have been determined by direct combustion complemented by infrared absorption detection technique with an ELTRA CS-800 instrument. The relative uncertainties of the analyses are estimated to be 15, 25 and 3 wt% for the N, O and C contents, respectively.

X-Ray diffraction analysis was performed on a Bruker Bragg-Brentano D8 advanced diffractometer (Cu $K_{\alpha1}$ radiation) equipped with a Lynxeye linear position sensitive detector. The powder patterns were recorded at room temperature using a step size of 0.01973° with an exposure of 4 s across the angular range $10° \leq 2\theta \leq 120°$. Operating conditions were 40 kV and 40 mA. Lattice parameters were refined by the Le Bail method using the X'Pert HighScore Plus program.

Raman spectra were recorded using a Jobin – Yvon T64000 confocal spectrometer with notch filters and single grating (mono configuration). This system is equipped with a microscope for confocal micro-Raman measurements. Spectra were acquired with a Peltier cooled CCD matrix, with a resolution of ± 1 cm^{-1}. The 514 nm line of an Ar$^+$ laser were used as excitation sources, with a power on the sample surface of 6 mW to obtain the best signal to noise ratio. Spectra were recorded within 0° geometry (*i.e* on the reflected beam).

Scanning Electron Microscopy (SEM) was conducted on a Vega Tescan TS 5130-LSH. The operating conditions were 200 eV and 30 KeV. SEM images of complete beads were recorded using a magnification range of 3- 1000000. RAMAN spectra were measured on one of the beads identified in the SEM images.

X-ray absorption spectroscopy measurements were conducted at the dedicated actinide beamline ROBL at the European Synchrotron Radiation Facility (ESRF, France). The storage ring operating conditions were 6.0 GeV and 170–200 mA. A double crystal monochromator mounted with Si [111] crystals was used. Extended X-ray Absorption Fine Structure (EXAFS) spectra were collected at room temperature in transmission mode at the U L_{III} edge using UN powder mixed with BN and a Y foil was located between the second and the third ionization chamber for energy calibration of individual scans. The ATHENA software [10] was used for extracting EXAFS oscillations. Experimental EXAFS spectra were Fourier-transformed using a Hanning window in the *k* range [3.5-13.3] Å^{-1}. The ARTEMIS software [10] was used for the curve fitting in R for *R* values ranging from 1 to 6.2 Å. Both interatomic scattering path phases and amplitudes were calculated using the FEFF 8.40 [11] ab initio code. The FEFF calculations were based on spherical 7.5 Å clusters of atoms built using the NaCl *Fm-3m* structure. As previously described for UN [12], the more relevant multiple scattering paths have also been considered. The amplitude reduction factor was held constant at 0.90 [12] and the shift in threshold energy was varied as a global parameter in the fits.

2.3. Results and discussion

2.3.1. Sample purity

The results of the chemical analyses are summarized in Table 2.1. Due to the high uncertainty of the method, it is difficult to provide an absolute quantification of the exact stoichiometry of the nitride. Chemical analysis indicated that the uranium nitride contained oxygen (0.07 wt %) and carbon (0.2 wt%). These values are lower than those reported elsewhere (> 0.3 wt %) [5 -14].

Table 2.1: Chemical analysis of the UN sample (* Assuming that all C, O are in solid solution of the UX-type (X=C + O + N)).

.**UN**	Measured content (wt%)	Relative uncertainty (%)
N	6.5	15
O	0.0675	25
C	0.2	3
X/U *	0.997	12

Figure 2.1 presents the micro-Raman spectra recorded on 4 different spots of 4 μm^2 on a UN bead.
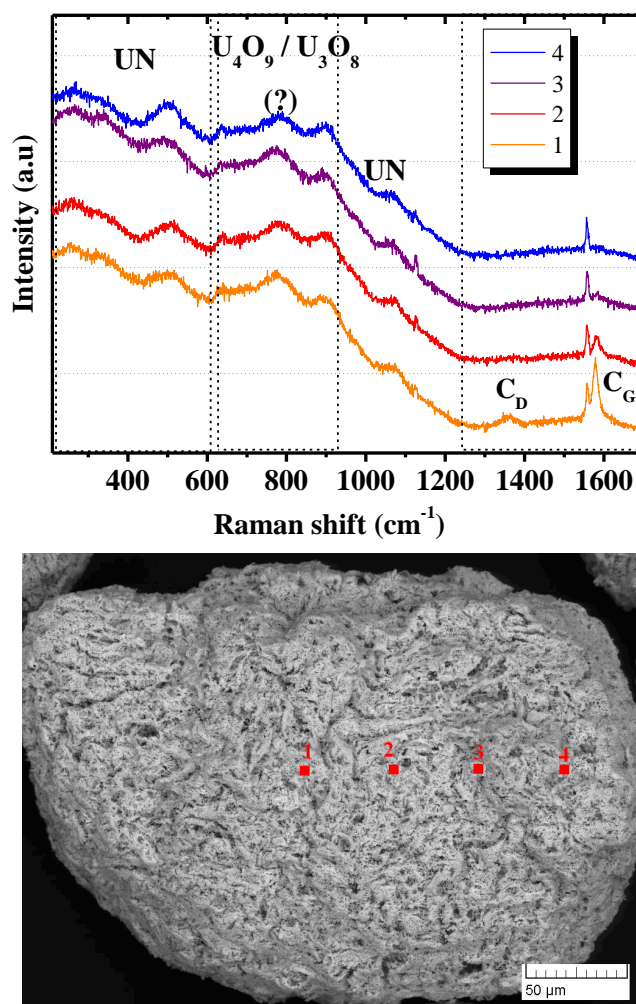
Figure 2.1: Raman spectra of the as-synthesized UN at 4 different spots (up). Secondary electron image of UN sample (* 1, 2, 3 and 4 correspond to the positions of the RAMAN spectra) (down).

One can note that the C content is not homogeneously distributed in the bead. Three different spectral regions were identified i.e at 200-600 cm^{-1}, 600-900 cm^{-1} and 1350-1600 cm^{-1}. Raman spectroscopy is very sensitive to ppm levels of carbon present in a sample [15]. Using the Raman spectra of Zr-N-O as reference, the main UN peaks are expected in the region between 200 and 600 cm^{-1} [16], and as shown in Figure 2.1, the spectrum of UN is dominated by two peaks at 237 and 510 cm^{-1}. It has been reported that the peak in the range

of 150–260 cm^{-1} and the peak at about 500 cm^{-1} are due to the disorder- induced single acoustic phonons and the disorder-induced scattering from optic phonons in fcc mononitrides, respectively [16]. By analogy with ZrN, these peaks can be attributed to U-N acoustic and U-N optical phonons observed at 150-260 cm^{-1} and 450-550 cm^{-1}, respectively [16]. A weak shoulder around 1030 cm^{-1} can be tentatively attributed to an overtone of the longitudinal optical mode (LO) observed around 510 cm^{-1}.

In contrast, the carbon G peak is easily visible at 1583 cm^{-1} in spectra recorded on the bead, together with the disordered graphite D-mode at 1360 cm^{-1} [17]. A sharp Raman mode is always visible at 1550 cm^{-1}, the typical frequency of adsorbed O_2 molecules [18-19]. The presence of molecules O_2 could seem unlikely given the highly reactive nature of UN. In contrast, this feature could either correspond to an amorphous carbon (with sp^3 bond), carbon diamond or amorphous carbonitride [20].

The presence of oxygen impurities can also explain the formation of irregular U_4O_9 and U_3O_8 thin layers on the sample surface, to which we assign the modes visible in the 600-900 cm^{-1} range [21]. The obvious observation that such Raman modes are broad and weak would be compatible with the fact that the corresponding oxide layers should be extremely thin (a few nanometres).

2.4.   Structure

Figure 2.2 shows the XRD pattern of the as-synthesized UN sample. All the diffraction peaks of the samples match the cubic UN phase (*Fm-3m* (225)). In addition, the diffraction peaks are very sharp which implies high crystallinity of the material.
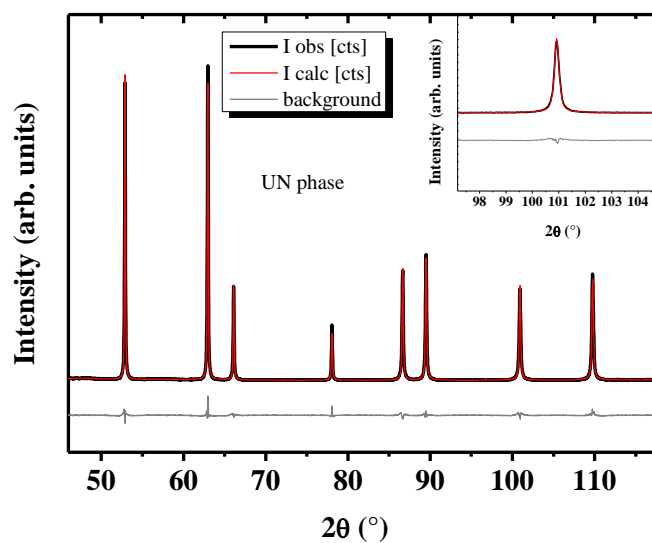
Figure 2.2: XRD of the as-synthesized UN.

The refined lattice parameter was 4.8950(2) Å, which is slightly higher than the value reported in the literature (4.8902(3) Å) [14]. This increase could be due to the presence of carbon in the lattice [22]. Indeed, while insensitive to small oxygen impurities [23], the UN lattice parameter is sensitive to carbon impurities [22], which can even lead to the formation of a U(C,N) solid solution [24].

EXAFS measurements have been performed to probe the local environment of the U atoms.

Figure 2.3 shows the corresponding k^3-weighted and the Fourier Transform EXAFS spectra.
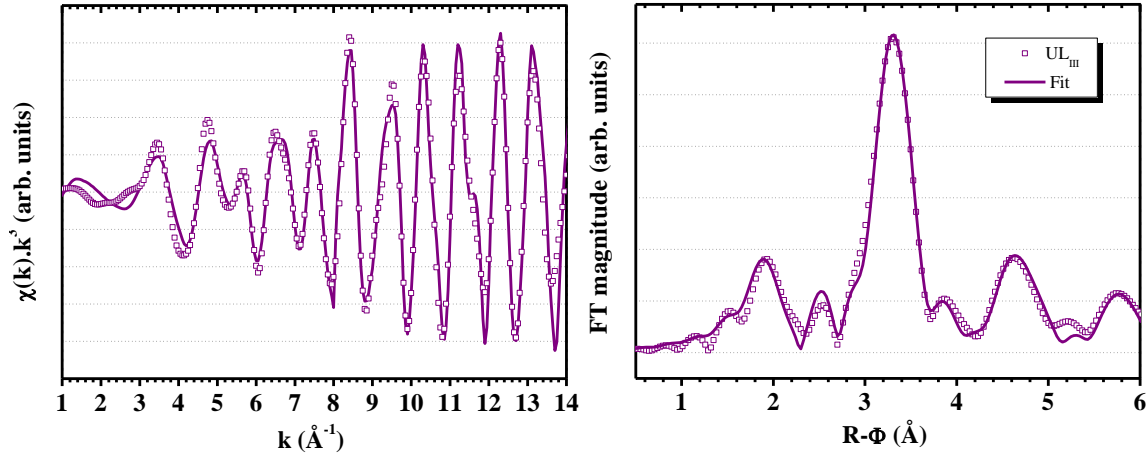
Figure 2.3: k^3 weighted EXAFS spectra and Fourier transform of the as-synthesized UN.

No additional N bonds with U were needed to reproduce the experimental data. A good agreement between the experimental and fitted data is observed, confirming the validity of the used structural model. The structural parameters are presented in Table 2.2.

Table 2.2: Crystallographical parameters derived from the fitting of k^3-weighed U L_{III} EXAFS analysis (*: data calculated from the XRD lattice parameter).

Edge	Shell	R (Å)	N	σ^2 (Å^2)	R_{XRD} (Å)
U L_{III}	N_1	2.447(5)	5.7 (5)	0.007 (1)	2.451 *
k range : 3.5 - 13.3	U_1	3.461 (5)	11.8 (5)	0.004 (1)	3.464 *
R-range : 1.35 - 6.2	U_2	4.92(1)	8.1 (5)	0.006 (1)	4.922 (1)
	U_3	6.01(2)	24	0.008 (1)	6.07 (1)

EXAFS analyses indicate that the environment around the main atom is formed by nitrogen at 2.447(5) Å and uranium atoms at 3.461(5), 4.92(1) and 6.01(2) Å, respectively. These interatomic distances are consistent with those derived from the XRD lattice parameter for the UN structure (see Table 2.2). The highly-structured environment of the material can be deduced from the ability to distinguish three cation shells. The results obtained for the U-N and U-U bonds are in a good agreement with the only other EXAFS study made on UN [12].

The Debye-Waller factor values are very low for a room temperature measurement embellishing the evidence of the high degree of order in the structure.

2.5.   Conclusion

We optimised an external gelation process obtaining large UN particles of approximately 20-150 μm in diameter, which resulted in the production of a very limited amount of dust during the fuel synthesis. This reduction of the dust free decreases the radiotoxicity, increasing the safety of such fuels. The chemical characterisation of the UN beads produced revealed a particularly low level of oxygen impurities (600ppm), enabling future safety related property determination, as the ultimate goal of this work. A unique Raman analysis was performed on UN for the first time, revealing the presence of Raman active modes similar to other mono-nitrides. Local micro-Raman analysis also showed the irregular presence of carbon and oxygen impurities on sample surface. XRD and EXAFS analyses revealed the presence of a single highly ordered (*Fm-3m)* phase.

2.6.   References

[1]   T. Inoue, M. Sakata, H. Miyashiro, N. Yoshiki, T. Matsumura, A. Sasahara, *J. Nucl. Sci. Technol.; 93:2 (1991)*.

[2]   P.E. Evans, T.J. Davies, *J. Nucl. Mater., 10 (1963) p.43*.

[3]   G. Ledergerber, Z. Kopajtic, F. Ingold, R.W. Stratton, in:, H. Matzke, G. Schumacher (Eds.), Nuclear Materials for Fission Reactors, Elsevier, Oxford, 1992, pp. 28–35.

[4]   Y. Arai, S. Fukushima, K. Shiozawa, M. Handa, J. Nucl. Mater., 168 (1989) p.280.

[5]   K. Minato, M. Akabori, M. Takano, Y. Arai, K. Nakajima, A. Itoh, T. Ogawa, *J. Nucl. Mater., 320 (2003) pp. 18*.

[6]   T. Ogawa, Y. Shirasu, K. Minato, H. Serizawa, *J. Nucl. Mater., 247 (1997) p.151*.

[7]   A. Fernandez, J. McGinley, J. Somers, M. Walter, *J. Nucl. Mater., 392 (2009) p.33*.

[8]   C. Ganguly, P.V. Hegde, *J Sol-Gel Sci Technol 9 (1997) 285*.

[9]   A.Fernandez, M.Walter, J.Somers, *(n.d.)*.

[10] B. Ravel, M. Newville, *J. Synch. Rad. 12 (2005) p.537*.

[11] J.J. Rehr, J.J. Kas, M.P. Prange, A.P. Sorini, Y. Takimoto, F. Vila, *Comptes Rendus Physique 10 (2009) p.548*.

[12] F. Poineau, C.B. Yeamans, G.W.C. Silva, G.S. Cerefice, A.P. Sattelberger, K.R. Czerwinski, *J. Radioanal.and Nucl. Chem. 292 (2011) p.989*.

[13] V.V. Akhachinskii, S.N. Bashlykov, *Atomic Energy 27 (1969) p.1317*.

[14] E.H.P. Cordfunke, *J. Nucl. Mater*., 56 (1975*) p. 319*.

[15] T. Jawhari, A. Roid, J. Casado, *Carbon 33 (1995) p.1561*.

[16] C. Moura, P. Carvalho, F. Vaz, L. Cunha, E. Alves, *Thin Solid Films 515 (2006) p. 1132*.

[17] S. Reich, C. Thomsen, *Phil. Trans. R. Soc. Lond. A 362 (2004) p. 2271*.

[18] J.E. Cahill, G.E. Leroi, *J. Chem. Phys. 51 (1969) p. 97*.

[19] H.G.M. Edwards, D.A. Long, K. B. Najm, M. Thomsen, *J. Raman Spectros. 10 (1981) p. 60*.

[20] A.C. Ferrari, J. Robertson, *Phil. Trans. R. Soc. Lond. A 362 (2004) p. 2477*.

[21] D. Manara, B. Renker, *J. Nucl. Mater., 321 (2003) p.233*.

[22] P.E. Potter, *J. Nucl. Mater.,* 42 (1972*) p. 1*.

[23] T. Muromura, *J. Nucl. Sci. Technol., 19 (1982) pp.638-645*.

[24] M. Katsura, T. Sano, *J. Nucl. Sci. and Technol. 3 (1966) p. 194.*

[25] T. Inoue, M. Sakata, H. Miyashiro, N. Yoshiki, T. Matsumura, A. Sasahara, *J. Nucl. Sci. Technol.; 93:2 (1991).*

[26] S.Voit, Advanced Fuel Cycle Initiative (AFC) 1G Test in the Advanced Test Reactor (ATR), Private Comunication, *(n.d).*

[27] M. Takano, A. Itoh, M. Akabori, T. Ogawa, S. Kikkawa, H. Okamoto, Synthesis of Americium Mononitride by Carbothermic Reduction Method, in Proc. Global'99: Nuclear Technology – Bridging the Millennia (Jackson Hole, Wyoming, Aug. 29-Sept. 3, p. 1999).

[28] T. Ohmichi, K. Shiozawa, Y. Arai, Roles and Direction of Material Science in Nuclear Technology, in Proc. of the Fourth International Symposium on Advanced Nuclear Energy Research (Ibaraki, Japan, 1992, p. 167).

[29] Petricek,V., Dusek,M. & Palatinus,L, (2006) JANA 2006.

[30] Y. Suzuki, Y. Arai, T. Iwai, T. Ohmichi, *J. Nucl. Sci. and Technol., 28 (1991) p.689.*

[31] M. Kato, K. Konashi, *J. Nucl. Mater., 385 (2009) p.117.*

Chapter 3

Preparation and Characterization of (U,Pu)N and (U,Pu,Am)N

ABSTRACT

Mixed uranium-plutonium nitrides are promising fuels for fast reactors. In comparison with the mixed uranium-plutonium oxides, mixed nitride fuel (U,Pu)N has the advantages of applicability to PUREX method in the reprocessing stage, compatibility with different cladding material and chemical stability against oxidation.

Americium recycling for transmutation, however, has been tested mainly for the oxides in fast neutron reactor applications. To determine safety relevant properties such as vapour pressure, thermal conductivity, etc., it is essential to have high quality and well characterized reference samples. The incorporation of minor actinides in fuels, and especially of Am, is a problematic issue in term of safety, as these elements are highly radiotoxic, which requires higher safety considerations, minimising operator exposure to radiation. Thus, decreasing the generation of dust in the synthesis steps, radiation dose is reduced. To reach these goals, improvements in the synthesis route must be achieved. This letter reports the synthesis of (U,Pu)N and (U,Pu,Am)N with 25% of Pu and 9% of Am from the (U,Pu)O$_2$ precursor. The synthesis route relies on an adaptation of the carbothermal reduction method, using a sol gel approach to prepare the precursor oxide particles, containing carbon in the feed solution (C/M=2.8, M=U,Pu), via a sol gel step, thus ensuring a dust free product. The americium was

infiltrated into these oxide beads, prior to the carbothermal reduction step. The products synthesized have been also characterised by X-ray diffraction.

3.1.   Introduction

The transmutation of Minor Actinides (MA) is one of the potential options to reduce the radiotoxic inventory of spent nuclear fuel [1]. Among the various possibilities, mixed uranium-plutonium nitrides are considered to be a suitable matrix to host MA, and ultimately as a transmutation fuel in a homogeneous reactor minor actinide recycling route. Several attempts have been made to synthesize MA bearing nitrides by carbothermal reduction of the oxide [2-13].

The incorporation of MA in fuels, is problematic in terms of safety, as these elements are highly radiotoxic, specially of Am, which is responsible of the major radiotoxicity amongst the MA. Therefore, dedicated facilities with remote manipulators and glove boxes are mandatory for handling Am and Pu. In addition, several studies [8,13] have shown that the volatilisation of Am can occur during the synthesis process, which is a non-acceptable feature.

The Joint Research Centre-Institute for Transuranium Elements (JRC-ITU)'s programmes on nuclear fuel safety (Safety of Advanced Nuclear Fuels, SANF among others) focuses on the determination of safety relevant properties for the safety assessment of nuclear fuels in operation in nuclear reactors. This goal can only be achieved, however, by the synthesis of high quality and high purity reference samples. Concerning minor actinides this brings an extra challenge as the As Low As Reasonable (ALARA) principle applies, and operator dose must be minimised.

This particular study concentrates on the improvement of the traditional synthesis of both (U,Pu)N and (U,Pu,Am)N. Thus, we have pursued the traditional route of carbothermal reduction of the oxide and modified it. The starting material for the carbothermal reduction has been prepared by a combination of sol-gel and infiltration methods, whereby the carbon necessary for the carbothermal reduction is directly incorporated in the fuel during the sol gel step. In comparison to the traditional synthesis methods such as power metallurgy, these improvements present several advantages in particular the absence of dust during the

preparation of Am fuels; this is an important safety criterion. Dust control is an important part of reducing exposure to radiation. In the process, the gel contains the liquid and the solid phase. After, the drying the liquid is removed yielding the porous beads.

3.2. Experimental

The synthesis of nitrides requires utmost attention and provision of highly chemically inert atmospheres in the glove boxes, since these materials may be pyrophoric and are highly reactive with oxygen. In addition, the presence of Am, being highly radiotoxic, necessitates the use of glove box standards with operation by remote manipulators [14].

The nitrides were synthesized by coupling external gelation sol-gel and infiltration methods (for (U,Pu,Am)N only) and carbothermal reduction steps. Figure 3.1 describes the complete synthesis process of (U,Pu)N and (U,Pu,Am)N with 25% of Pu and 9% of Am. The carbon needed for the carbothermal reduction is already incorporated in the sol-gel step. The feed solution consists of a solution of Pu and U nitrate. Organics, such as methocel, tetrahydrofurfuryl alcohol (THFA) and triton are added to increase the viscosity and decrease the surface tension. This broth is dropped into an ammonia bath where ammonia diffuses into the droplet causing precipitation. A similar method was employed in the past to synthesize (U,Pu,Am)N with 20% of Pu and 2% of Am [2]. The JRC-ITU uses an inverted cup rotating at high speed to produce the droplets. Due to the configuration of this device, the resulting particle size is in the 20-150 µm size range. Thus, the sol-gel route provides an intimate mixing of the solid solution $(U,Pu)O_2$ with C.
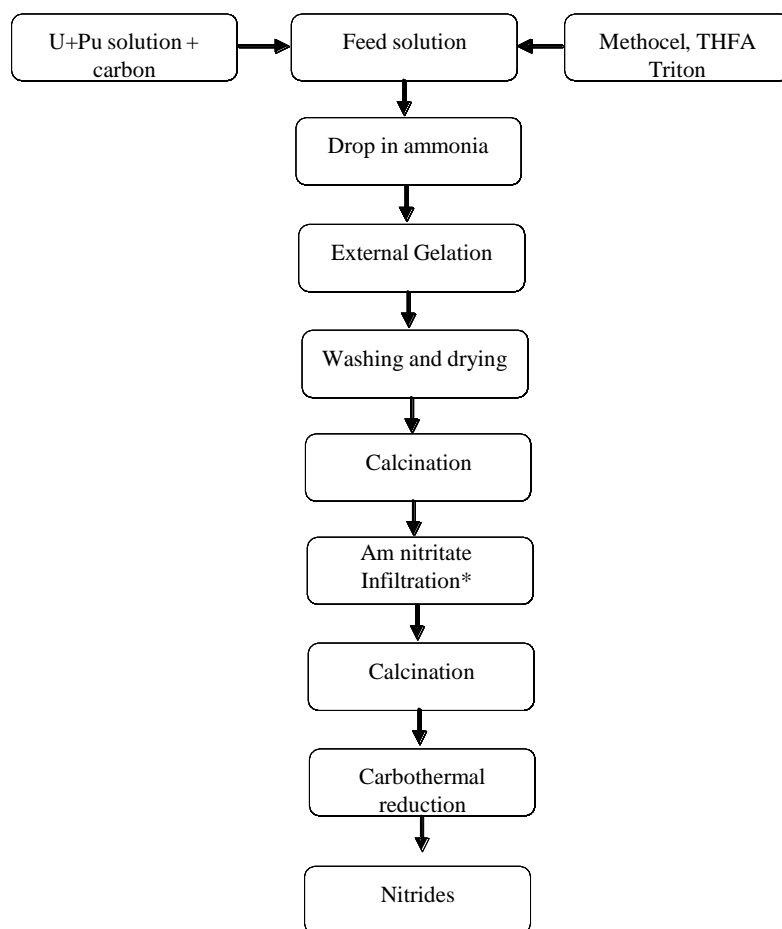
Figure 3.1: Synthesis process of (U,Pu)N and (U,Pu,Am)N. (* The infiltration step is only for (U,Pu,Am)N)

It is important, to maintain a high degree of dispersion of the carbon powder, which can be assisted by the addition of dispersion agents, such as triton. Lower processing temperatures during the carbothermal reduction step should be possible, as the mixed U-Pu oxide, even as micron sized beads, is formed from nano crystal grains, likely deposited directly on the carbon grains.

For both (U,Pu)N and (U,Pu,Am)N, the carbothermal reduction was performed on the calcined beads, following optimisation of the conditions that have been established for this type of compounds [15] i.e. at 1500°C during 10h under N_2. Two hours before cooling down, N_2/H_2 was introduced to remove the excess of carbon since the carbon had been added in

excess in the feed solution (C/M=2.8) to ensure complete carbothermal reduction. Cooling under Ar/H_2 avoided the formation of higher nitrides.

XRD analyses were performed using a Bragg-Brentano Bruker D8 Advance diffractometer (Cu $K_{\alpha 1}$ radiation) equipped with a Lynxeye linear position sensitive detector. The powder patterns were recorded by step scanning using a step size of 0.01973° with an exposure of 4s per step across the angular range $10° \leq 2\theta \leq 120°$. Lattice parameters were obtained by the Le Bail method using the Jana program [16].

3.3. Results and discussion

3.3.1. (U,Pu)N

The XRD pattern of the $U_{0.75}Pu_{0.25}N$ sample is presented in Figure 3.2. Two phases were observed. The $(U_{0.75}Pu_{0.25})N$ rocksalt-type phase is present in a concentration of *ca* 96 % and exhibits a lattice parameter of 4.893 (2) Å, which is in a good agreement with the value reported in the literature by Benedict *et al.* [17] (4.891 (2) Å for $U_{0.80}Pu_{0.20}N$). Considering the lattice parameters of UN (4.890 Å) and PuN (4.905 Å) [3], the measured value in this study is in good agreement with that derived from the Vegard law (4.892 Å). An additional impurity fluorite (*Fm-3m*) phase was found with a content of about 4 % with a lattice parameter of 5.470 (2) Å. As UO_2, PuO_2 and AmO_2 exhibit the fluorite structure (*Fm-3m*), one can conclude that this minor phase corresponds to an $MO_{2\pm x}$ species. Knowing that the primary beads are $(U,Pu)O_2$ and considering the variation of the Vegard law of the MOX lattice parameter with O/M [18], the measured lattice parameter suggests that this phase corresponds to $U_{0.75}Pu_{0.25}O_{1.95}$, where plutonium is partially reduced to the oxidation state III due to the reductive conditions used in the latter stages of the nitride synthesis.
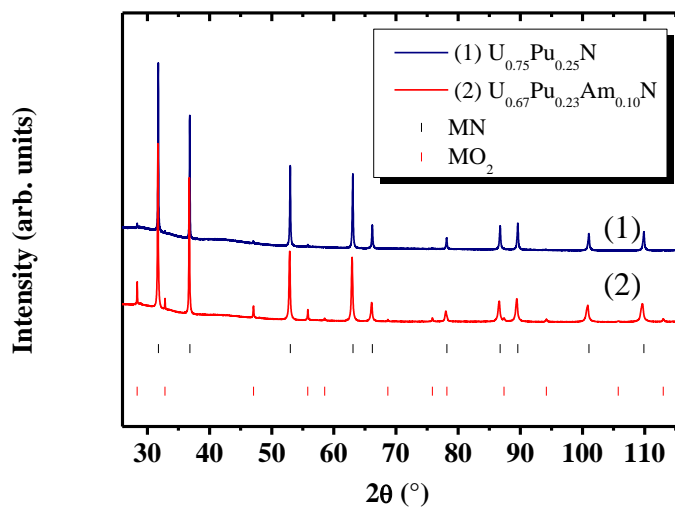
Figure 3.2: XRD patterns of (U,Pu)N and (U,Pu,Am)N.

3.3.2.   (U,Pu,Am)N

According to calorimetry and alpha spectroscopy methods, the Am content was 9.1(3) % before the carbothermal reduction (CTR). After the synthesis of the nitride, an Am content of 9.7(5) % was determined. Considering the uncertainty of the measurements, no sublimation of Am was detected during the CTR step. One can conclude that the final stoichiometry is $U_{0.67}Pu_{0.23}Am_{0.10}N$ and goes beyond an earlier study at JRC-ITU which succeeded in synthesizing a similar sample with 2% Am [2]. The slight increase in Am content in the sample can be reconciled with losses of residues from the sol gel or more likely by the reaction of excess carbon with N_2/H_2 in the final stages of CTR, and Ar/H_2 during the cool down period.

The XRD pattern of (U,Pu,Am)N is presented in Figure 3.2 and, as for (U,Pu)N, two phases are observed. The main phase, corresponding to about 91 % of the final product, is attributed to a (U,Pu,Am)N rocksalt type structure with a lattice parameter of 4.902 (1) Å. Considering a linear combination between the three pure compounds lattice parameters with 67% of UN, 23% of PuN and 10% of AmN whose lattice parameter is 4.991 Å [3], one can estimate a lattice parameter of 4.902 Å, which is in exceptional agreement with the measured

value of 4.902 (1) Å for this $U_{0.67}Pu_{0.23}Am_{0.10}N$. The secondary phase, present up to *ca* 9%, crystallized in the fluorite type structure (*Fm-3m*) and has a lattice parameter of 5.468 (2) Å. By analogy with the above (U,Pu)N, one can assume that this is an oxide $MO_{2\pm x}$ phase and most likely corresponds to $U_{0.67}Pu_{0.23}Am_{0.10}O_{2\pm x}$ as the metal content should remain identical. The O/M stoichiometry cannot be estimated in this case due to the considerable lack of data in the U–Pu–Am–O system. One can assume that the O/M <2.00. This impurity oxide reflects the very reactive nature of the nitride, an incomplete carbothermal reduction or a combination of both.

3.4.   Conclusion

The JRC-ITU has successfully synthesised (U,Pu,Am)N. Although further improvements remain to be made, these results demonstrate the promise of this route for the safe synthesis of this potential transmutation fuel. Thus, the path is opened to reach the ultimate goal of this work, namely high quality property measurements to enable a full and accurate safety assessment of these materials as fuels in reactors.

3.5.   References

[1]   T. Inoue, M. Sakata, H. Miyashiro, N. Yoshiki, T. Matsumura, A. Sasahara, *J. Nucl. Sci. Technol.; 93:2 (1991).*

[2]   A.Fernandez, M.Walter, J.Somers, *(n.d.).*

[3]   K. Minato, M. Akabori, M. Takano, Y. Arai, K. Nakajima, A. Itoh, T. Ogawa, *J. Nucl. Mater., 320 (2003) pp. 18.*

[4]   M.Takano, A. Itoh, M. Akabori, K. Minato, M. Numata, Study on the stability of AmN and (Am,Zr)N in Proc. Global'03 (New Orleans, U.S.A, Nov. 16-20 pp. 2285-2291).

[5]   Y. Arai, K. Nakajima, *J. Nucl. Mater., 281 (2000) pp. 244-247.*

[6]   K. Nakajima, Y. Arai, Y. Suzuki, *J. Nucl. Mater., 247 (1997) pp. 33-36.*

[7]   T. Muromura, *J. Nucl. Sci. Technol., 19 (1982) pp.638-645.*

[8]   M. Takano, A. Itoh, M. Akabori, T. Ogawa, S. Kikkawa, H. Okamoto, Synthesis of Americium Mononitride by Carbothermic Reduction Method, in Proc. Global'99: Nuclear Technology – Bridging the Millennia (Jackson Hole, Wyoming, Aug. 29-Sept. 3, p. 1999).

[9]   Y. Suzuki, Y. Arai, Y. Okamoto, T. Ohmichi, *J. Nucl. Sci. Technol., 31 (1994) pp.677-680.*

[10]   T. Ogawa, T. Ohmichi, A. Maeda, Y. Arai, Y. Suzuki, *J. Alloys Comp., 224 (1995) pp. 55-59.*

[11]   Y. Okamoto, A. Maeda, Y. Suzuki, *J. Nucl. Mater., 206 (1993) p. 94.*

[12]   M.Takano, A.Itoh, M. Akabori, T. Ogawa, M. Numata, H. Okamoto, *J. Nucl. Mater., 294 (2001) pp. 24-27.*

[13]   S.Voit, Advanced Fuel Cycle Initiative (AFC) 1G Test in the Advanced Test Reactor (ATR), Private Comunication, *(n.d).*

[14]   T. Ohmichi, K. Shiozawa, Y. Arai, Roles and Direction of Material Science in Nuclear Technology, in Proc. of the Fourth International Symposium on Advanced Nuclear Energy Research (Ibaraki, Japan, 1992, p. 167).

[15]   U. Carvajal-Nunez, D. Prieur, D. Manara, E. Lopez Honorato, A. Scheinost, J. Somers, *J. Nucl. Mater.,submitted, 2013.*

[16]   V. Petricek, M. Dusek & L. Palatinus, (2006), JANA 2006.

[17]   U. Benedict, K. Richter, *J. Nucl. Mater., 55 (1975) pp. 352-354.*

35

[18]   M. Kato, K. Konashi, *J. Nucl. Mater. 385 (2009) pp. 117-121.*

Chapter 4

Melting Point Determination of Uranium Nitride and Uranium Plutonium Nitride:

a Laser Heating Study

ABSTRACT

Understanding of the behaviour of nuclear material in extreme conditions is essential for the analyses of the operation limits of nuclear fuels, and prediction of possible nuclear reaction accidents. In this context, the high temperature behaviour of uranium nitride and mixed uranium-plutonium nitrides has been studied in the present work by laser heating under controlled atmosphere coupled with fast multi-wavelength pyrometry. Such an approach has allowed performing a thermal arrest analysis and establishing the solid-liquid phase boundaries in the investigated compositions, whereby non-congruent vaporisation was avoided by setting a suitable nitrogen overpressure. In addition, the normal spectral emissivities of the current samples were determined by radiance spectroscopy. Besides revealing a slightly more metallic optical behaviour in plutonium-containing compositions, this latter characterisation led to the determination of the real melting / solidification temperatures of the investigated nitrides. It is confirmed that UN melts congruently at (3120 ± 30) K in a nitrogen pressure of 0.25 MPa (2.5 bar). The melting / solidification temperatures decrease in plutonium containing samples, reaching (3045 ± 25) K for x(PuN)=0.2, a composition of interest for potential applications of this material as a nuclear fuel. Besides

their fundamental importance, the current results are useful for a deeper understanding of the nitride fuel behaviour under accidental conditions, whereby uncontrolled thermal excursions might occur in the nuclear reactor core.

4.1. Introduction

Uranium nitride (UN) and mixed uranium-plutonium nitride (U,Pu)N exhibit a number of favourable nuclear fuel properties when compared to conventional oxide fuels, including high fissile atom density and high thermal conductivity [1,2]. A complete knowledge of the high temperature behavior of these materials is therefore fundamental for the fuel design and safety, as it defines the performance limits of a fuel element itself [3]. Whilst problems and proposed solutions concerning the nitride synthesis are addressed in another publication [4], the current paper deals with the measurements of solid/liquid equilibria in uranium nitride and one mixed uranium - plutonium mononitride. In the present research, the melting behaviour of sol-gel synthesized nitrides has been investigated by a recently developed quasi-containerless fast laser heating technique, coupled with multi-wavelength spectro-pyrometry for the measurement of temperature. The phase diagram of the U-N binary system has been widely studied [5–8] at temperatures well below melting, and has notably been reported in the compilation works of Okamoto [9] and of Uno *et al.* [10]. Uranium mononitride (UN), dinitride (UN_2) and sesquinitride (U_2N_3) are the stable compounds observed in this material system. UN and UN_2 are envisaged in the NaCl type face-centered and cubic CaF_2-type face-centered cubic respectively with (*Fm-3m*) space group both, while U_2N_3 crystallizes in a body centered cubic structure at low temperature (α- U_2N_3) and in a hexagonal structure at higher temperature (β-U_2N_3) [11,12] envisaged in the (*Ia-3)* space group. The high-temperature properties and the phase stability of the U-N system have been summarized by Hayes *et al.* [13] and more recently by Chevalier *et al.* [14]. The congruent melting point of UN has been published as 3123±30 K [15,16] for a nitrogen pressure superior or equal to 2.5 atm. Other values (2923±100 K [17] and 2753±50 K [14]) have been reported in the literature, but are considered to be too low and unreliable [14]. The present temperature determination by a pyrometric method requires knowing some UN optical properties such as the reflectivity, the

transmissivity and, especially, the emissivity. In this field, the only direct reflectivity measurements (at room temperature) were reported by Arakawa *et al.* [18].

Uranium-plutonium mixed nitrides (U,Pu)N crystallize in the same NaCl-type structure, as UN and PuN [10]. Although UN and PuN form a continuous solid solution, a large deviation from Vegard´s law was observed, suggesting the non-ideality of the solution [19]. Two different melting temperatures for the composition $U_{0.8}Pu_{0.2}N$, 2633 and 3053 ± 20 K, have been proposed by Huebotter [20] and Nightingale *et al.* [21], respectively. No data about the optical properties of these mixed nitrides are available in the literature.

Considering the high volatility of these nitrides at high temperature [22,23] and their strong tendency to react with an even low amount of oxygen [24], only very few data have been published on their high temperature behaviour. These were obtained by heating, in dedicated furnaces, nitride samples under a nitrogen overpressure, mostly at the price of costly and cumbersome experimental facilities. Technical difficulties were even increased in the investigation of radioactive samples, for which the experimental setup had to be mounted in suitable shielded cells or glove boxes.

In this context, the current investigation aims at providing more and extra data on the high temperature behaviour of UN and (U,Pu)N by using a modern heating approach based on remote laser irradiation. It is possible, with this technique, to perform a thermal analysis up to very high temperature (well beyond melting) on a sample mounted in a radiation-shielded autoclave under controlled atmosphere. In the present setup, neither the heating agent (the laser) nor the measuring devices (the pyrometers) are in contact with the pressurised and radioactive environment, which makes the entire experimental procedure much easier and more flexible compared with more traditional ones. As a result, a consistently larger number of experimental data have been collected, allowing for a sounder statistical analysis. Furthermore, some novel data about the spectral emissivities of the investigated compounds have been measured thanks to the employment of pyrometers operating at different wavelengths in the visible and near-infrared domains. After laser melting, the samples were finally characterized by X-Ray Diffraction (XRD) and by Scanning Electron Microscopy (SEM).

4.2.   Experimental section

4.2.1.   UN and (U,Pu)N samples

The nitride samples were prepared by carbothermal reduction under N_2 of carbonous oxides beads produced by coupling external sol-gel and carbothermal reduction methods. This process, fully described by Carvajal *et al.* [4], has also been employed to ensure the synthesis of (Zr,U)N [25].

According to the X-Ray Diffraction (XRD) collected with a Bruker Bragg-Brentano D8 advanced diffractometer (Cu $K_{\alpha 1}$ radiation), rocksalt-type solid solutions *(Fm-3m)* have been produced for both UN and (U,Pu)N samples.

4.2.2.   Laser melting

4.2.2.1.   <u>Laser heating pulses</u>

UN and (U, Pu)N samples were mounted in a controlled-atmosphere autoclave closed by a gas - proof quartz window 10 mm thick. Physical contact to their mount was limited by using three radially arranged graphite screws to hold them in place. In some case, zirconium oxide based ceramic glue produced by Advanced Materials Inc. ® was used to fix the sample. Independently, only a small portion of the sample surface was irradiated by a heating laser beam, so that the hot material was only in contact with cooler parts of the same composition. This self-containing (or quasi-containerless) character of the current measurements greatly reduced or completely ruled out problems such as uncontrolled interaction between the sample and its containment, typically encountered in nitrides at high temperatures.

These specimens were studied at very high temperature by laser heating combined with fast pyrometry (Figure 4.1), as described by Manara *et al.* [26].
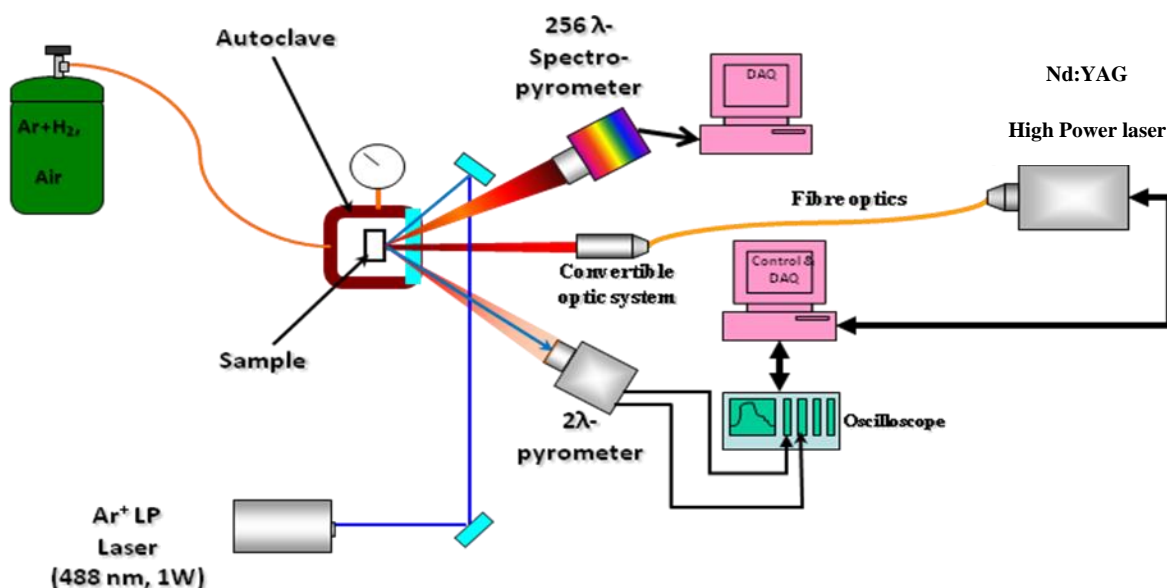
Figure 4.1: Experimental Setup of the laser heating combined with fast pyrometer.

The heating agent was a Nd:YAG 4.5 kW cw laser radiating at 1064.5 nm, programmable with a complex power / time profile, allowing thermal cycles of variable duration. The laser beam, conveyed by fiber optics, impinged on the sample surface on an approximately circular area of 3 mm in diameter, heating it beyond melting for variable time durations (from a few tens of ms to a few hundreds ms). The invariance of the recorded phase transition temperatures with the dwelling time in the liquid state could thus be checked, to study the possible occurrence of phenomena out of the thermodynamic equilibrium (such as segregation or non-congruent vaporisation). The high power laser pulse was then switched off and the sample let cool naturally. Cycles of three successive melting pulses were performed in each experiment. During the intervals between pulses (lasting several seconds), the sample temperature has decreased to an intermediate level, close to the pyrometer's detection limit (approximately 1400 K). Avoiding full cooling to room temperature between the melting pulses ensured a better mechanical stability of the sample throughout repeated shots, which lead to an improved result reproducibility. Finite element simulations of the heating cycles (Böhler *et al.* [27]), supported by micro-imaging of the quenched samples, ensured that at the beginning of the cooling process homogeneous temperature was produced in the laser

irradiated area for a depth of a few tens μm. Thermal analysis was then performed on the cooling stage of the cycle.

4.2.2.2. *Temperature measurements*

The sample temperature was measured on a spot of 0.5 mm in diameter at the centre of the laser-heated area by means of a pyrometer equipped with a fast logarithmic amplifier (adjusting the time of about 10 μs to 1% of log output) and operating at 655 nm [26]. It was calibrated against a standard tungsten-ribbon lamp in the range of 1800 to 2500 K, ensuring traceability to the International Temperature Scale of 1990 [28]. Beyond this temperature, the validity of the calibration, as well as the quality of the optical windows and the alignment, were tested by measuring in-situ the melting radiance temperatures of molybdenum and tungsten (2530 K and 3207 K, respectively, at 653 nm (Bedford *et al.* [29]).

A further spectro-pyrometer, based on a linear array of 256 Si photodiodes, was used to record the sample thermal radiance in the range of 488 to 1011 nm. This instrument allows a more complete spectral analysis, whereby its main disadvantage is in the poorer time resolution (one spectrum per millisecond at best) [26]. Due to low signal-to-noise ratio, only the range of 550 to 920 nm was useful for the current measurements. The photodiode at 649 nm was calibrated up to 2500 K using the tungsten-ribbon lamp and this calibration was transferred to a tubular-cavity variable-temperature graphite blackbody-furnace up to 3500 K. The remaining photodiodes were then calibrated with this blackbody, allowing a conversion of output signal to spectral radiance over the entire useful wavelength range. The measured radiance spectra recorded in the vicinity of the melting / solidification points were fitted by least-squares regression to Planck's distribution law for blackbody radiance, modified by a wavelength- and temperature-dependent function assumed to represent the normal spectral emissivity (NSE or ε_λ). Although such an approach is known to be affected by low numerical accuracy [30], compared to other techniques, it can be considered as acceptable for materials, like the current uranium and plutonium nitrides, which are known to display a regular emissivity behaviour (continuous and monotonous trend as a function of λ). The normal spectral emissivity is a parameter relating the thermal radiance emitted by a real surface at a given temperature T with the thermal radiance emitted by an ideal blackbody at the same

temperature. Since only such an ideal blackbody follows Planck's radiation law, the following identities hold for a real surface:

$$L_\lambda = \varepsilon_\lambda \cdot L_{\lambda bb} = \frac{1}{\lambda^5} \cdot \frac{\varepsilon_\lambda}{e^{\frac{c_2}{\lambda T}} - 1} = \frac{1}{\lambda^5} \cdot \frac{1}{e^{\frac{c_2}{\lambda T_\lambda}} - 1} \qquad (1)$$

Where *bb* stand for "blackbody", L_λ is the radiance power intensity per unit solid angle, unit volume and unit wavelength, $c_{1L} = 2 \cdot h \cdot c_0^2$ is the first radiation constant, taken here as unity, and $c_2 = h \cdot c_0 \cdot k_B$ is the second radiation constant (14,388 K·µm). c_0 is the speed of light in vacuum, h Planck's constant, and k_B Boltzmann's constant. Equation (1) defines also the radiance temperature T_λ, which is the temperature directly measured on a real surface by a pyrometer operating at the wavelength, λ. In the hypothesis that $\exp\left(\frac{c_2}{\lambda \cdot T}\right) \gg 1$ (acceptable for T·λ<3100 K·µm), the relation between T and T_λ can easily be derived from equation (1):

$$\frac{1}{T} = \frac{1}{T_\lambda} + \frac{\lambda}{c_2} \cdot \ln \varepsilon_\lambda \quad (2)$$

The normal spectral emissivity values measured with the current approach have been compared with the only ones available in literature, the room temperature reflectivity (ρ_λ) data reported by Arakawa *et al.* [18], with the help of the following identity:

$$\varepsilon_\lambda = 1 - \rho_\lambda \qquad (3)$$

Equation (3) is valid for any opaque material under the hypotheses of Kirchhoff's law [31], always met in the current experimental conditions. The current NSE values were then used to transform radiance into real temperature through Equation (2) in pyrometer-recorded thermograms.

4.2.2.3.   The reflected light signal method

In addition to locating the characteristic freezing arrest upon cooling, an additional method was applied in some cases to facilitate the observation of the melting / freezing

transition onset. This so called "Reflected Light Signal (RLS)"-method relies on recording the intensity of a lower-power (750 mW) Ar^+ probe-laser which is reflected off the sample surface (Manara *et al.* [26]). A characteristic noise-like structure appeared in the RLS upon melting, due to vibrations of the sample's liquid surface (which disappeared again upon solidification), permits the detection of the variations in the reflectivity of the samples surface, which may indicates phase transitions.

4.2.3. Post-melting sample characterisation

Scanning Electron Microscopy (SEM) and X-ray diffraction (XRD) were used to characterize the nitride samples after the laser heating / melting / freezing cycles. SEM was conducted on a Vega Tescan®, Model TS 5130- LSH. The operating conditions were 200 eV and 30 keV. For the samples containing plutonium, images were recorded on a Philips® XL40 operated at 20 kV. Cross-sections through melted surfaces were prepared for microstructural analysis and imaged unetched. SEM images of complete beads were recorded using a magnification range of 3- 1.000,000 and a resolution of 1 nm. XRD was performed using a Bruker® D8 Advance diffractometer (Cu-K_{a1} radiation) with a 2θ range of 10°-120° using 0.009° steps with 2 s of count time per step at operating conditions of 40 kV- 40 mA. The XRD instrument was equipped with a Lynxeye® 3 linear position sensitive detector.

4.3. Results and discussion

4.3.1. Laser melting

4.3.1.1. <u>Uranium nitride</u>

A UN sample was heated under an over-pressure of 0.25 MPa of 99.999 % pure nitrogen. The sample stability towards fast vaporisation could in fact not be ensured for N_2 partial pressures lower than 0.2 MPa at the melting point, in agreement with previous observations [6,15,16]. One of the thermograms recorded during the laser heating / cooling cycles on uranium mononitride is reported in Figure 4.2a.
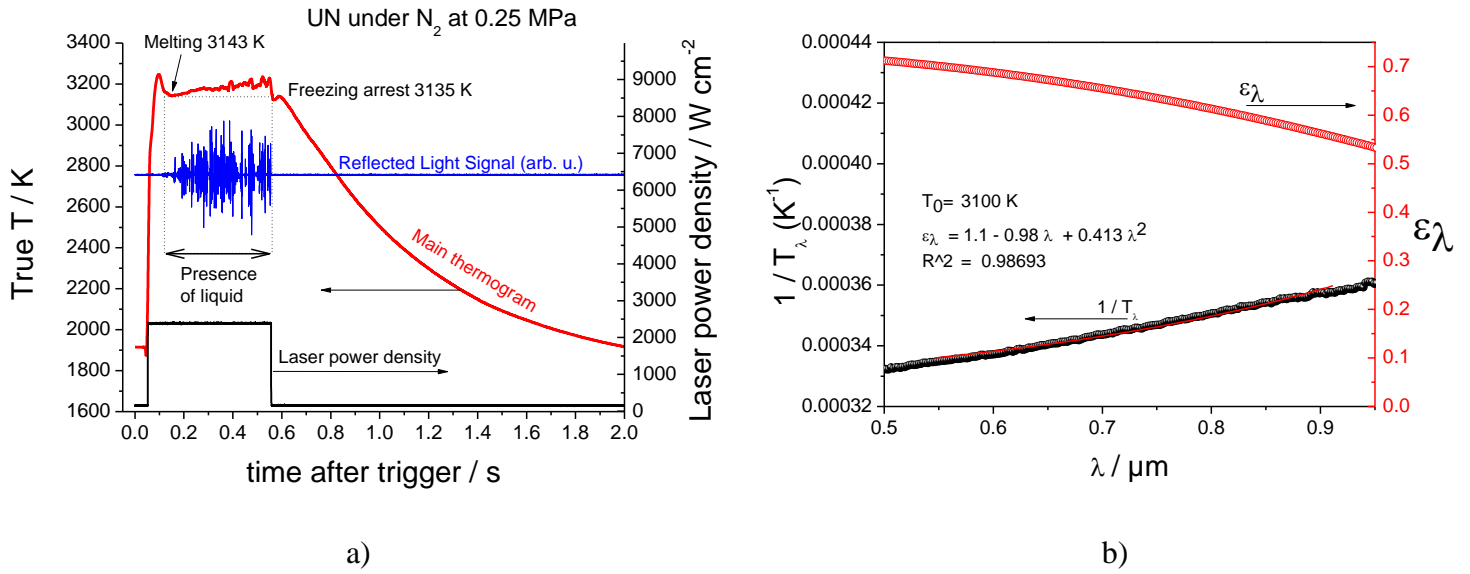
Figure 4.2ab: UN laser heating thermogram and emissivity analysis.

The melting point is clearly visible on the heating flank of the radiance temperature T_λ *vs.* time curve, highlighted by a change of its slope and an apparent temperature peak. No obvious thermal arrest is observable at this stage, as expected, due to the high-power localised heating and the fact that thermodynamic equilibrium is not guaranteed at this stage on the measurement spot [26,32]. The apparent temperature peak and thermogram slope change is justified by an abrupt change in the thermophysical properties (thermal conductivity, density, NSE) of the material upon the formation of liquid.

A very clear thermal arrest can be observed in the cooling stage of the experiment, after the end of the heating laser pulse. At this point, the sample is let cool naturally, and upon solidification the melting enthalpy released leads to a clear plateau at a radiance temperature slightly below 3000 K. Throughout the experiment, the presence of a liquid phase on the sample surface is confirmed by the clear vibrations in the reflected light signal (RLS), ascribable to capillar forces in the fluid (surface tension). The slight undercooling affecting this plateau is a well known feature typical of fast freezing, ascribed to the solidification kinetics by a nucleation and growth process. In the current experiments, it is due to the time needed for the forming solid to reach the free sample surface, where the temperature is actually measured by the pyrometers. Taking into account such a mechanism, the maximum

45

recoalescence point should be taken as the real freezing radiance temperature. This last can be converted into real temperature through Equation (2), once ε_λ is determined. This is done with the help of the current multi-wavelength spectro-pyrometer. The procedure is shown in 4.2b. The current experimental values of the inverse radiance temperature at the freezing plateau are plotted *vs.* wavelength (limited to the investigated spectral window) as in Equation (2). The resulting curve is fitted with a non-linear function of the type of Equation (2), where ε_λ is dependent on λ. Such dependence is taken, as a starting approximation, from a polynomial fit of Arakawa's data [18]. The best fit of the current data yields the following values for real temperature and NSE:

$$T_{M(UN)} = 3110 \text{ K} \pm 35 \text{ K}$$

$$\varepsilon_\lambda = 1.1 - 0.98{\cdot}\lambda + 0.413 \cdot\lambda^2$$

In Figure 4.2b, the values obtained in the present analysis for ε_λ of freezing UN is then compared with those calculated from Arakawa's data points though Equation (3). The fair agreement between the two sets of points confirms the numerical stability of the adopted procedure and the negligible dependence of ε_λ on temperature (Arakawa data were in fact measured at room temperature).

It is also worthwhile to remark that this emissivity analysis ensures that the observed melting and freezing material is actually UN. In fact, because its melting point is very close to the one of uranium dioxide (3130 K $\pm$ 20 K) [33, 34, 35] and because of the possible presence of oxygen impurities, one could be led to doubt that UO_2 might have formed on the surface, and been heated through the solid/liquid transition instead of UN. However, the normal spectral emissivity of uranium dioxide is well established and displays a constant value of approximately 0.83, independent of the wavelength (greybody behaviour) [36]. Instead, the current NSE values and trend are clearly those of uranium nitride, in agreement also with the measurements of Arakawa *et al.* [18].

The same kind of measurement has been successfully repeated three times on the same UN sample. The resulting melting / freezing temperature is 3120 $\pm$ 20 K. The fact that such temperature stays reproducible over successive shots suggests that segregation and non-

congruent vaporisation phenomena, if present, have no visible effect on the measured solid/liquid equilibrium temperature.

4.3.1.2. *Uranium- plutonium nitride*

An experimental procedure identical to that explained for UN was applied to $U_{0.8}Pu_{0.2}N$ samples. Typical resulting radiance temperature *vs*. time and ε_λ *vs*. wavelength curves is reported in Figure 4.3 and, with more details, in Figure 4.4a and b.
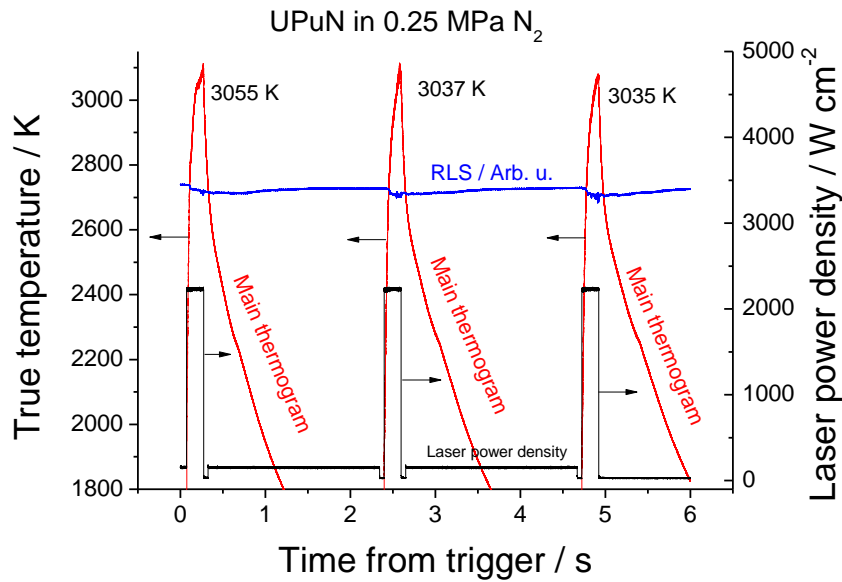
Figure 4.3: Example of a full heating / cooling cycle performed by laser irradiation on a nitride sample. The presence of a liquid layer on the sample surface is revealed by the onset of vibrations in the Reflected Light Signal (RLS). Solidification points correspond to thermal arrests on the temperature vs. time curve (thermogram).

47

a)   b)
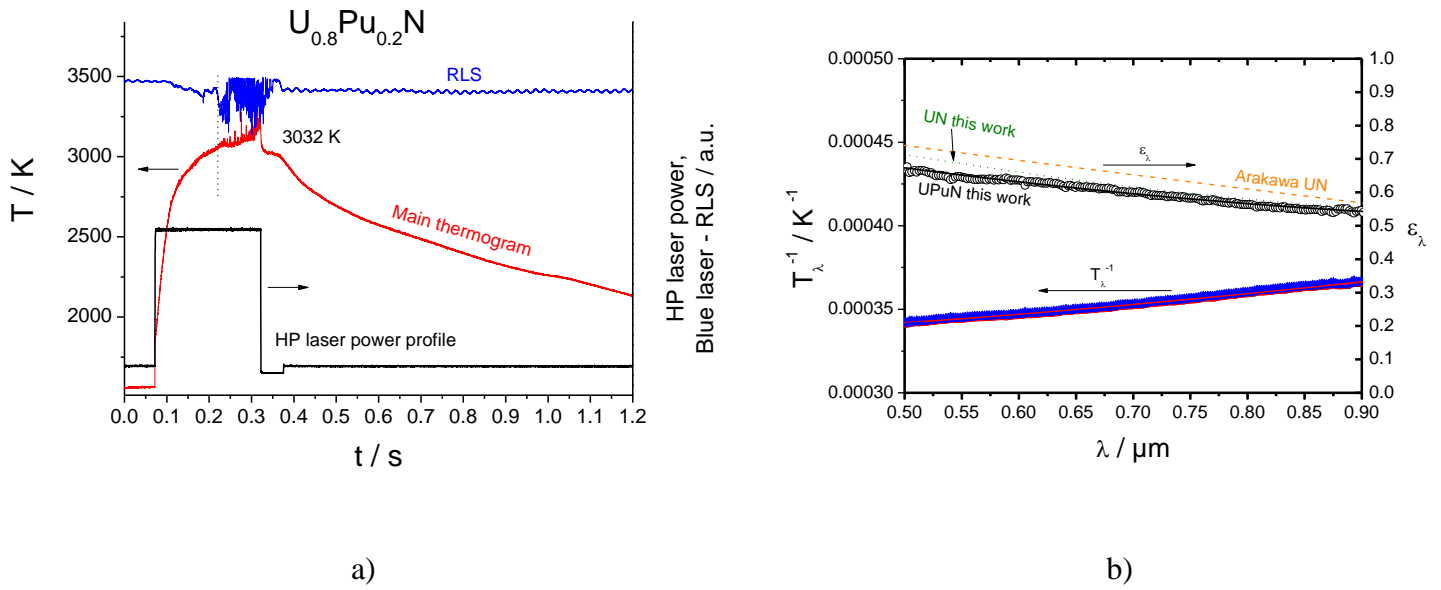
Figure 4.4ab: $U_{0.80}Pu_{0.20}N$ laser heating thermogram and emissivity analysis.

Nine successful laser shots were performed on each of the two pellets. The sample melting point was overcome in fifteen of these shots, with a satisfactory reproducibility of the resulting solidification temperature:

$$T_{M((UPu)N)} = 3045 \text{ K} \pm 25 \text{ K}$$

The rather disturbed shape of the thermogram shows that vaporisation must occur at the highest temperatures. This phenomenon has certainly a limited impact on the recorded solidification points, which are well reproducible over successive shots. However, it might result in segregation effects on the sample surface, not necessarily visible in the melting/freezing recorded temperatures.

Figure 4.4b reports the NSE analysis performed on one (U,Pu)N sample. The resulting NSE *vs* λ trend is very similar to the one obtained in this work and measured by Arakawa [18] for UN (both curves are displayed in the same graph for comparison). The best fit of experimental data was obtained with the following equation:

$$\varepsilon_\lambda = 0.976 - 0.761 \cdot \lambda + 0.310 \cdot \lambda^2$$

The current NSE measured on mixed uranium-plutonium nitride is slightly lower than the NSE of UN. Although the difference is still within the experimental uncertainty, this observation might indicate that the addition of plutonium to the (U,Pu)N solid solution lead to a slightly more reflective material, with more metallic electro-optical properties.

4.3.2.   Error analysis

The dispersion of the present experimental melting / freezing points is combined, using the law of independent error expansion with the systematic uncertainties typical of the employed technique [26]. Global values for 2-σ uncertainty bands are thus obtained, as reported above for the melting / freezing points of UN and (U,Pu)N.

The error on the NSE coefficients is more difficult to estimate because of the more complex numerical procedure needed for their optimisation. The relative uncertainty on the NSE value at 655 µm, most important for the conversion of the current radiance temperature into real temperature through Equation (2), can be taken as $\pm$ 5 % of the absolute ε_λ value. The corresponding effect on the real melting/freezing points has been taken into account in the reported temperature uncertainties.

4.3.3.   Post sample characterization

4.3.3.1.   Uranium Nitride

Due to the difficulty to separate the molten from the unmolten part, the XRD pattern was collected on a piece of sample including mostly molten and refrozen material, but also macroscopic traces of unmolten parts. Figure 4.5 shows the XRD patterns of the UN sample before and after melting.

49
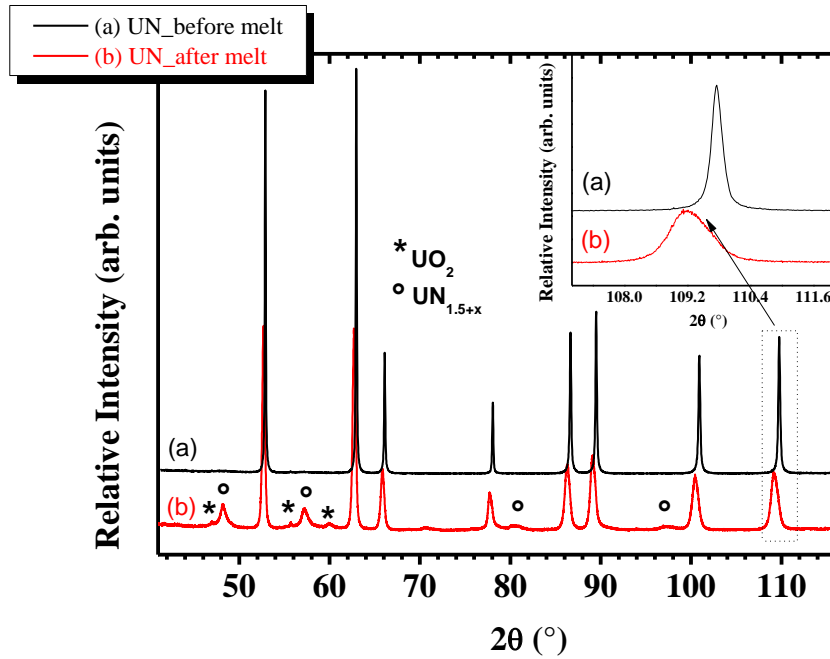
Figure 4.5: XRD patterns of UN before and after laser melting.

One can clearly observe that both samples have the same crystal structure, i.e. NaCl fluorite type face centred cubic. The lattice parameter of the UN after laser melting is equal to 4.908(2) Å, which is higher than the original value of 4.895 (1) Å before laser melting [4]. Considering the lattice parameter values reported in the literature for $UN_{0.8}$, $UN_{1.04}$ and $UN_{1.10}$ [37], no clear variation can be established upon deviation of the N/U ratio from the exact unity. For that reason, it is difficult to determine if the formed UN phase is UN_{1-x} or UN_{1+x}. Note though this uncertainty in the composition is largely negligible in terms of observable effects on the melting temperature. Furthermore, to discard the possibility of the effect of the impurities, chemical analyses have found that the present UN sample contains low O (0.0675 wt%) and C (0.2 wt%) contents as impurities [4].

The presence of two additional minor phases is suggested by additional diffraction XRD peaks. One of these minor phases corresponds to a fluorite UO_{2+x} phase with a lattice parameter of 5.472 (2) Å. The other minor phase can be indexed as a UN_{2-x} or a U_2N_{3+x} phase, with either a lattice parameter of 5.33(2) Å or 10.66(2) Å. The lattice parameter of $UN_{1.5 \leq x < 2}$

can vary over a fairly wide range. For precisely stoichiometric $UN_{1.5}$, a value of 10.678(5) Å was found, 10.580(5) Å for $UN_{1.75}$ up to the values for UN_2 [38].

Although supplementary XRD peaks of superstructure should be visible in the case of U_2N_3 phase, these structural features are not observed. However, the presence of U_2N_3 can not be discarded in reason of the quality of the XRD pattern and the low cristallinity level of the phase. One can only conclude that, in these conditions, the cooling of UN leads to the formation of a non-stoichiometric UN, a UO_{2+x} and a $UN_{1.5+x}$ phase.

These observations suggest that UN cannot be considered to melt congruently under the current experimental conditions. Since only one thermal arrest is clearly visible in the reported thermograms (see Figure 4.4a), the solidus and liquidus points most likely exist for this composition, however very close to each other in temperature.

The solidification and cooling paths can then be rather complex, and lead to the formation of UN_{2-x} or U_2N_{3+x} and non-stoichiometric uranium mono-nitride of uncertain composition in the vicinity of stoichiometric UN. It is also possible, that some UN_{2-x} or U_2N_{3+x} are formed because of the nitrogen overpressure under which the laser heating cycles were performed. A full comprehension of these phase transformations upon cooling would imply a detailed description of the U-N binary phase diagram in a compositional range. Indeed, only very recently [38] it has been investigated at temperatures well below melting, and never at higher temperatures.

The presence of uranium dioxide traces can be explained by the high-temperature prompt reaction of the nitride with oxygen traces still present in the autoclave. As reported above however, no effect of such impurities on the melting behaviour of the current UN samples could be detected with the present experimental approach. This is consistent with the measured emissivity which is obviously the one of UN, with no signs of UC or UO_2.

Figure 4.6 shows the SEM image of the UN pellet after melting. The laser-irradiated zone, heated over the melting point is clearly visible in the middle of the sample. Three different zones are clearly observed: zone 1 which represents the molten zone, zone 2 which is a partially melted zone, and zone 3 which is a heat-affected portion.
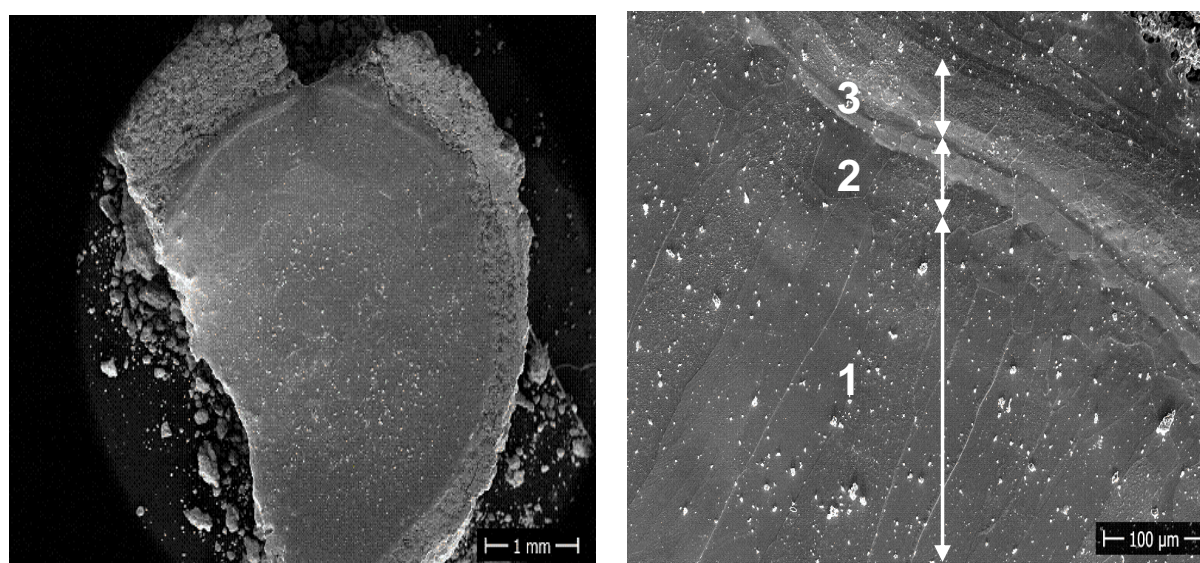
Figure 4.6: SEM–Secondary electron image of a UN sample after three laser heating cycles. Left: whole pellet. Right: magnification of the pellet,s surface. The zone 1, represents the molten zone, zone 2 is a partially melted zone, and zone 3 is a heat-affected portion

4.3.3.2. *Uranium-plutonium-nitride.*

Figure 4.7 shows the XRD patterns of $U_{0.80}Pu_{0.20}N$ sample before and after laser melting. In both cases, a NaCl fluorite type face centred cubic, as for UN, is observed.
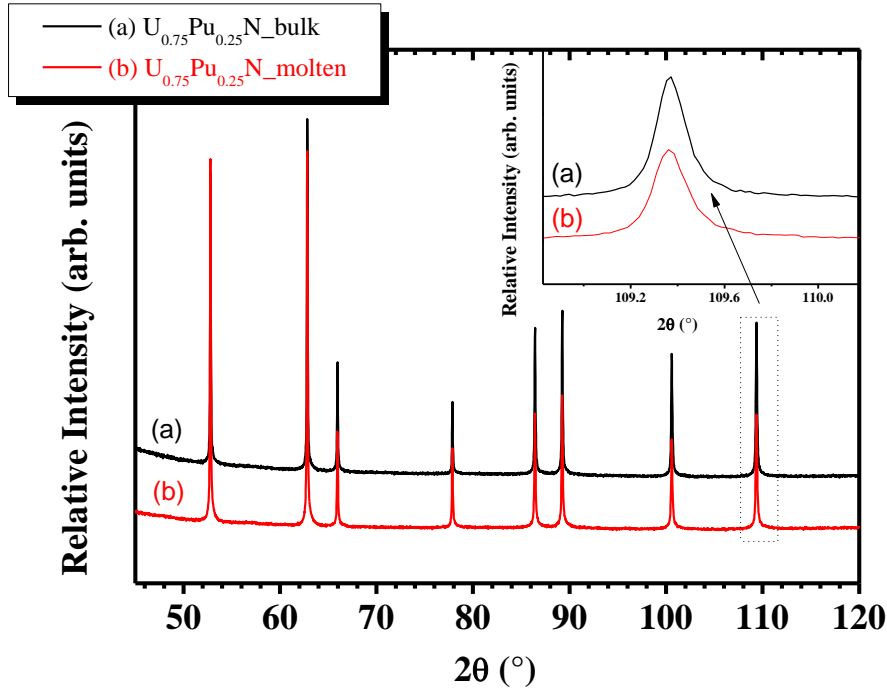
Figure 4.7: XRD patterns of $U_{0.80}$ $Pu_{0.20}N$ before and after laser melting.

The inset shows a magnification at high diffraction angles. The lattice parameter obtained for both the molten and unmolten material was 4.893(2) Å, in agreement with the value reported in the literature for the $U_{0.80}Pu_{0.20}N$ stoichiometry [39]. This means that, the mixed uranium-plutonium nitride studied in the present work melts congruently, at least within the uncertainty limits of the current XRD analysis. Although the current measurements would be consistent with a $U_{0.80}Pu_{0.20}N$ or in the vicinity of this composition, further experiments would be needed in order to confirm this point. In fact, the solidus and liquidus lines might be too close to each other to be clearly distinguished with the current experimental approach, a situation already reported for the $UC - UC_2$ system [40].

Compared with the results reported for pure UN, the present results suggest that the addition of plutonium to the fcc mono-nitride phase decreases its melting point. In contrast, the absence of secondary phases, it seems to stabilise the fcc NaCl – like solid solution at high temperature when the Pu is present in the structure. This information is of interest for a description of the ternary U-Pu-N phase diagram at high temperature. The morphology of molten and non molten parts was investigated by SEM (see Figure 4.8). The samples were

generally broken after the laser heating cycles. For that reason, the SEM does not allow to differentiate the laser-irradiated zones.
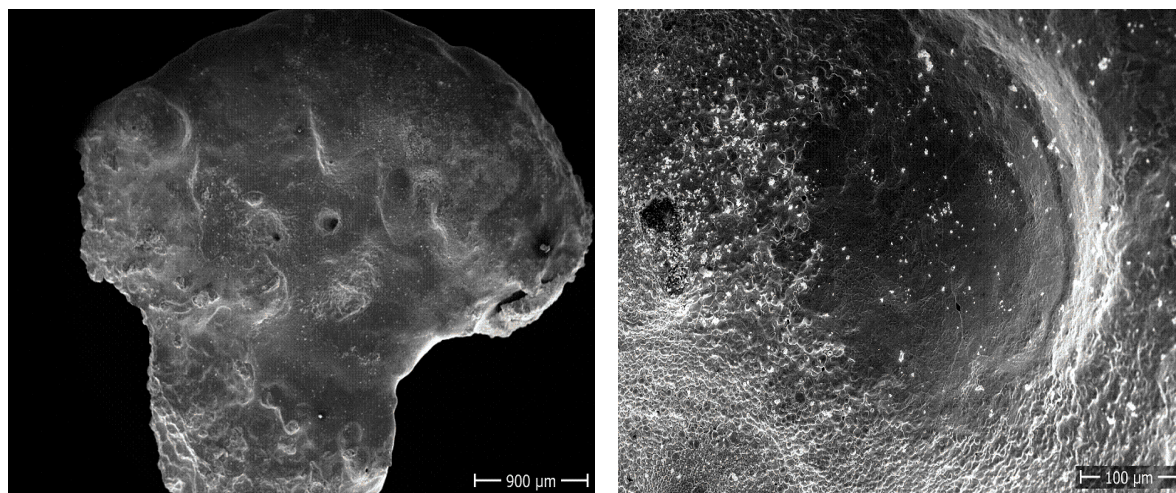
Figure 4.8: SEM–Secondary electron image of a $U_{0.80}$ $Pu_{0.20}$N sample after three laser heating cycles. The sample broke after the laser heating cycles (left). Magnification of the sample (right).

4.4.   Conclusions

The melting / freezing temperatures of both UN and mixed (U,Pu)N have been studied for the first time by fast laser heating and multi-wavelength pyrometry. The transition temperatures obtained by the current technique are in agreement with those previously proposed on the basis of more traditional measurements. According to the present study, the following temperatures recommended for the melting point of UN and $U_{0.80}Pu_{0.20}N$ are (3120 $\pm$ 30) and (3045 $\pm$ 25) K respectively. Pre- and post-melting XRD analysis performed on the laser irradiated samples shows that new phases are present in the UN samples after fast cooling from the liquid state. This suggests that UN might not melt congruently under the current experimental conditions, and that the binary U-N phase diagram might be rather complex for U/N$\leq$1 at high temperature. In contrast, no phase changes were detected instead between fresh and laser melted $U_{0.8}Pu_{0.2}N$, suggesting that this composition melts congruently under the current experimental conditions, or at least that its liquidus and solidus points must be too close to each other to be distinguished with the current technique. In any case, the addition of plutonium nitride to uranium nitride seems to stabilise the Na-Cl-like solid

solution at high temperature. The current results encourage further research on the melting and high-temperature behaviour of these and other refractory nitrides.

4.5.   References

[1]   P.E. Evans; T. J. Davies, *J. Nuc. Mater., 10 (1963) pp. 43–55.*

[2]   M. Streit; F. Ingold, *J. Eur. Ceram. Soc., 25 (2005) pp.2687–2692.*

[3]   D. R.Olander; Demonstration, U. S. E. R. and D. A. D. of R. D. and Fundamental aspects of nuclear reactor fuel elements: prepared for the Division of Reactor Development and Demonstration, Energy Research and Development Administration; Technical Information Center, Office of Public Affairs, Energy Research and Development Administration, 1976.

[4]   U. Carvajal-Nunez, D. Prieur, E. Lopez Honorato, A. Schenoist, J. Somers, *J. Nucl. Mater.,submitted, 2013.*

[5]   C. L. Hoenig, C. L. *J. Am. Ceram. Soc., 54 (1971) pp. 391–398.*

[6]   R. Benz, M. G. Bowman, *J. Am. Chem. Soc., 88 (1966) pp. 264–268.*

[7]   P.E. Lapat and R.B. Holden, in J.T. Waber, P. Chiotti and W.N. Miner (eds.), Compounds in Nuclear Reactor Technology, Edwards Bros., Ann Arbor, MI, 1964, p. 225.

[8]   F. Müller and H. Rages, Thermodynamics of Nuclear Materials, IAEA, Vienna, 1968, p. 257.

[9]   Okamoto, H. JPE 1997, 18, 107.

[10] M. Uno, T. Nishi, M. Takano, M. In Comprehensive Nuclear Materials; Rudy J.M. Konings, Ed.; Elsevier: Oxford, 2012; pp. 61–85.

[11] R. E. Rundle, N. C. Baenziger, A. S. Wilson, R. A. McDonald, *J. Am. Chem. Soc. 70 (1948) pp. 99–105.*

[12] F. Poineau, C. B. Yeamans, G. W. C. Silva, G. S. Cerefice, A. P. Sattelberger, K. R. Czerwinski, *J. Radioanal. Nucl. Chem., 292 (2011) pp. 989–994.*

[13] S. L. Hayes, J. K. Thomas, K. L. Peddicord, *J. Nucl. Mater., 171 (1990) pp. 300–318.*

[14] P.-Y. Chevalier, E. Fischer; B.Cheynet, *J. Nucl. Mater., 280 (*2000) pp. 136–150.

[15] W. M. Olson, R. N. R. Mulford, *J. Phys. Chem., 68 (1964) pp. 1048–1051.*

[16] J. Bugl, A.A. Bauer, *J. Am. Ceram. Soc., 47 (1964) pp. 425–429.*

[17] P. Chiotti, *J. Am. Ceram. Soc., 35(*1952) pp. 123–130.

[18] E.Arakawa, M. W. Williams, *J. Nucl. Mater.,* 41 (1971) pp. 91–95.

[19] K. Minato, M. Akabori, M. Takano, Y. Arai, K. Nakajima, A. Itoh, T. Ogawa, *J. Nucl. Mater., 320 (2003) pp. 18-24.*

[20] P.E. Huebotter, Comparison of (U,Pu)C and (U,Pu)N as fast reactor fuel.; ANL-Memo; 1973.

[21] R.E. Nightingale, Fast reactor nitrides research., BNWL-842, 1968; pp. 6.1–6.3.

[22] W.M. Pardue, F.A. Rough, R.A. Smith, *J.* Nucl. Met., Met. Soc. AIME, 13: (1968) pp. 369-811.

[23] C. A. Alexander, J. S. Ogden, W. M. Pardue, *J. Nucl. Mater., 31 (1969) pp. 13–24.*

[24] H. Wiame, M.-A. Centeno, S. Picard, P. Bastians, P. Grange, *J. Eur. Ceram. Soc., 18 (1998) pp. 1293–1299.*

[25] M.Walter, J.Somers, A.Fernández-Carretero, J. Rothe*, J. Nucl. Mater., 373 (2008) pp. 90–93.*

[26] D. Manara; M. Sheindlin, W. Heinz, C. Ronchi, *Rev. Sci. Instrum., 79 (2008) pp. 113901–7.*

[27] R. Böhler, M. J. Welland, F. D. Bruycker, K. Boboridis, A. Janssen, R. Eloirdi, R. J. M. Konings, D. Manara, *J. Appl. Phys. 11 (2012).*

[28] H. Preston-Thomas, *Metrologia, 27 (1990) pp. 3–10.*

[29] R E Bedford, G Bonnier, H Maas, F Pavese, *Metrologia 33 (1996) pp. 133–154.*

[30] L. Fiessler, M. Groll, G. Neuer, *J. Sol. Energy Eng., 59(1992) pp. 14–20.*

[31] H. O. McMahon, *J. Opt. Soc. Am., 40 (1950) pp. 376–378.*

[32] M. J. Welland, W. T. Thompson, B. J. Lewis, D. Manara, *J. Nucl. Mater., 385 (2009) pp. 358–363.*

[33] H. Hausner, *J. Nucl. Mater., 15 (1965) pp. 179–183.*

[34] J. K. Fink, T. Sofu, H. Ley, *Inter. J. Therm., 20 (1999) pp. 279–287.*

[35] J. K. Fink, *J. Nucl. Mater., 279 (2000) pp. 1–18.*

[36] Bober, M. Eur Thermophys Prop Conf, 7th; Antwerpen, Belgium; 30 June – 4 July (1980) pp. 297-306.

[37] F. A. Shunk, M. Hansen, K.; Anderko, Constitution of binary alloys; McGraw-Hill, 1969.

[38] G. W. C. Silva, C. B. Yeamans, G. S.Cerefice, K. R. Czerwinski, A. P. Sattelberger, , *J. Chem. Mater. 20 (2008) pp. 3076–3084.*

[39] Y.Suzuki, Y.Arai, T.Iwai, T.Ohmichi, *J. Nucl. Sci. Technol., 28 (1991) pp. 689–691.*

[40] C. A. Utton, F. De Bruycker, K. Boboridis, R. Jardin, H. Noel, C. Guéneau, D. Manara, *J. Nucl. Mater., 385 (2009) pp. 443–448.*

Chapter 5

Characterization of Self-damaged (U,Pu)N Fuel Used in the NIMPHE Program

ABSTRACT

During in-pile, irradiation-induced damage occurs in nuclear fuel and results in a deterioration of its properties, which can affect the margin to melt of the fuel. Damage also occurs in fresh fuel through the self-irradiation process, and thus provides a convenient means to investigate changes in the material. A uranium-plutonium mixed nitride fuel made over 25 years ago, and stored in the ITU archives has been retrieved. Coupling EXAFS and TEM has shown that this material was still well-crystallized. However, an increase of 0.3 % of the lattice parameter was found. As shown by the EXAFS, the U-N and Pu-N as well as the metal - metal distances are similarly affected. However, no significant modification of both anion and cation sublattice was found. Although no defect clustering was found by EXAFS, the presence of nanometric helium bubbles was demonstrated by TEM as well as nanometric disordered domains.

5.1. Introduction

More than four decades ago, nitride fuels were identified as potential candidates for Sodium Fast Reactors (SFR) on the basis of their attractive properties, including a high thermal conductivity, a high heavy metal density and a high melting temperature [1,2]. In comparison with oxide cores, these properties should lead to a significant improvement of

both core safety and performance. Several irradiation programs [3,4] were conducted to study the in-pile behavior of these materials. Among others, the NIMPHE (NItrure Mixte dans Phénix à joint HElium) irradiation experiment in the Phénix reactor was performed jointly by CEA (Commissariat à l´Energie Atomique et aux Energies Alternatives) and JRC-ITU (Joint Research Centre-Institute for Transuranium Element) to compare the influence of different syntheses routes on the fuel performance. Thus, the preparation of mixed uranium-plutonium nitrides by the direct pressing method was realized at the JRC - ITU in 1987 with the collaboration of the CEA. While some of the pins were irradiated in the Phénix reactor and submitted to post-irradiation examinations, other samples were stored in the ITU archives. In these $U_{0.78}Pu_{0.22}N$ fuels, one can expect some changes of the fuel properties during the 25 years of storing time. Indeed, the aging process of Pu mainly leads to the following dominant reactions [5]:

$$^{238}Pu \rightarrow {}^{234}U + {}^4He \text{ (86 years)}$$

$$^{241}Pu \rightarrow {}^{241}Am + \beta \text{ (14 years)} \rightarrow {}^{237}Np + {}^4He \text{ (432 years)}$$
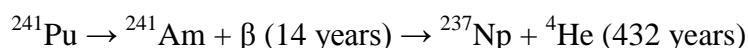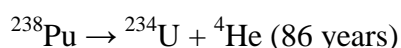
The combined α activities of ^{238}Pu, and ^{241}Am are associated to the formation of ~ 2500 Frenkel pairs per cascade induced mainly by the recoil nucleus (~ 85 keV), leading ultimately to the self-irradiation of the material as well as to the formation of helium. This mechanism can lead to well-known phenomena at the structural scale such as amorphization [6], allotropic transitions [7], lattice parameter expansion [8,9], defect formation [10,11] and pellet swelling at the macroscopic scale [12,13], leading ultimately to a change of the fuel thermophysical properties[14]. In this work, these potential changes, induced by the self-irradiation, have been studied using X-ray Absorption Spectroscopy (XAS) and Transmission Electron Microscopy (TEM).

5.2. Experimental

5.2.1. Material synthesis

One of the objectives of the NIMPHE irradiation experiment was to compare the influence of three different synthesis routes based on CTR (conventional carbothermal

reduction and direct pressing of pellets and granules) on the irradiation performance of nitride fuels. In the current work, the retrieved sample was synthesized by the direct pressing route, which is a method, developed at JRC-ITU, of cold-compacting based on the carbothermal reduction but without comminution [4,15]. In the framework of the NIMPHE program, the material synthesis was achieved in 1987. The $U_{0.78}Pu_{0.22}N$ archive-pellets were stored in a sealed pin under He in the ITU archives.

In 2012, after 25 years of storage, the pin was transferred in a glove box to retrieve the nitride pellets. Considering the isotopic composition given in Table 5.1 and a storage time of 25 years, the α cumulative dose is equal to $\sim 4.5 \times 10^{18}$ $\alpha.g^{-1}$.

Table 5.1: Isotopic composition of the as-synthesized and damaged NIMPHE fuel (*: measured by chemical methods).

	Composition (%) 1987 *
Pu/(U+Pu+Am)	20.8
^{238}Pu	0.16
^{239}Pu	74.64
^{240}Pu	21.86
^{241}Pu	2.63
^{242}Pu	0.71
Am/Pu	0.37
^{241}Am	100

The total dpa value as damage indicator resulting from the alpha-decays has been calculated using the SRIM code [16]. An average energy of 85 keV and of 5.5 MeV has been used for the recoil nucleus and the alpha-particle respectively. The displacement energy computed was 25 eV for both U/Pu and N atoms. The results using these parameters were ~ 1200 displacements per alpha-decay resulting in a total value of damage of 1.2 dpa. The damaged sample was then characterized using XRD, XAS, SEM and TEM.

5.2.2.   *Material characterization*

5.2.2.1.   <u>XRD</u>

XRD analyses were carried at room temperature using a Bragg-Brentano Bruker D8 Advance diffractometer (Cu $K_{\alpha 1}$ radiation) equipped with a Lynxeye linear position sensitive detector. The powder patterns were recorded by step scanning using a step size of 0.01973° with an exposure of 4s across the angular range $10° \leq 2\theta \leq 120°$. The operating conditions were 40 kV to 40 mA. Lattice parameters were refined by the Le Bail method using the X'Pert HighScore Plus program.

5.2.2.2.   <u>XAS</u>

XAS data acquisition was performed on the damaged $U_{0.78}Pu_{0.22}N$ powder mixed with BN, the latter being essentially transparent to X-rays. XAS measurements were conducted at the ROBL beamline dedicated to actinide elements at the European Synchrotron Radiation Facility (ESRF, France). The storage ring operating conditions were 6.0 GeV and 170–200 mA. A double crystal monochromator mounted with Si (1 1 1) crystal was used. XAS spectra were collected at room temperature in transmission mode at the U L_{III} and in fluorescence mode at the Pu L_{II} and Pu L_{III} edges. A 13-element Ge solid-state detector using a XIA (X-ray Instrumentation Associates) digital amplifier was used to acquire the fluorescence signal. Y, Zr and Mo foils were located between the second and the third ionization chamber for energy calibration of individual scans. Before averaging scans, each spectrum was aligned using the X-ray Absorption Near Edge Structure (XANES) spectra of the metallic foil. E_0 were taken as the first inflection point using the zero the first zero-crossing value of these second derivate. The position of the white line maximum was selected with the first zero-crossing of the first derivative.

The ATHENA software [17] was used to extract Extended X-ray Absorption Fine Structure (EXAFS) oscillations. Experimental EXAFS spectra were Fourier-transformed using a Hanning window. The ARTEMIS software [17] was used for the curve fitting in k^3 for R values ranging from 1.2 to 6.2 Å. Both interatomic scattering path phases and amplitudes

were calculated using the FEFF 8.40 [18] ab initio code. The FEFF calculations were based on spherical 7.5 Å clusters of atoms built using the NaCl *Fm-3m* structure. From the backscattering atoms in the unit cell, only the single scattering paths of the first N atom (N_1) and of the first three Me (U or Pu) atoms (Me_1, Me_2 and Me_3) have been included in the fits. As previously described for UN[19] and (U,Zr)N[20], the more relevant multiple scattering paths have also been considered. The amplitude reduction factor was held constant at 0.90 [19] and the shift in threshold energy was varied as a global parameter in the fits.

5.2.2.3.   *SEM*

Secondary electron (SE) and backscattered electron (BSE) images of the damaged $U_{0.78}Pu_{0.22}N$ sample were acquired using a Philips XL40 scanning electron microscope installed in a glove box [21].

5.2.2.4.   *TEM*

For TEM analysis small fragments of the sample were crushed in analytical grade ethanol with an agate pestle and mortar. A drop of the suspension was pipetted onto a carbon coated copper grid (400 mesh).

Transmission electron microscopy (TEM) investigations were conducted with a special modified FEI Tecnai G^2 F20 XT for the analyses of radioactive materials [21], operated at 200 kV and equipped with a Gatan GIF Tridiem energy filter. Electron energy-loss spectra (EELS) were acquired in scanning transmission electron microscopy (STEM) mode with irradiation times of between 5 and 20 s. The energy dispersion was 0.2 eV/channel and the convergence and collection angle were 20 and 14 mrad, respectively.

5.3.   Results and discussion

5.3.1.   XANES

The U L_3 and Pu L_3 edges XANES spectra of the damaged $U_{0.78}Pu_{0.22}N$ NIMPHE fuel are presented in the Figure 5.1.
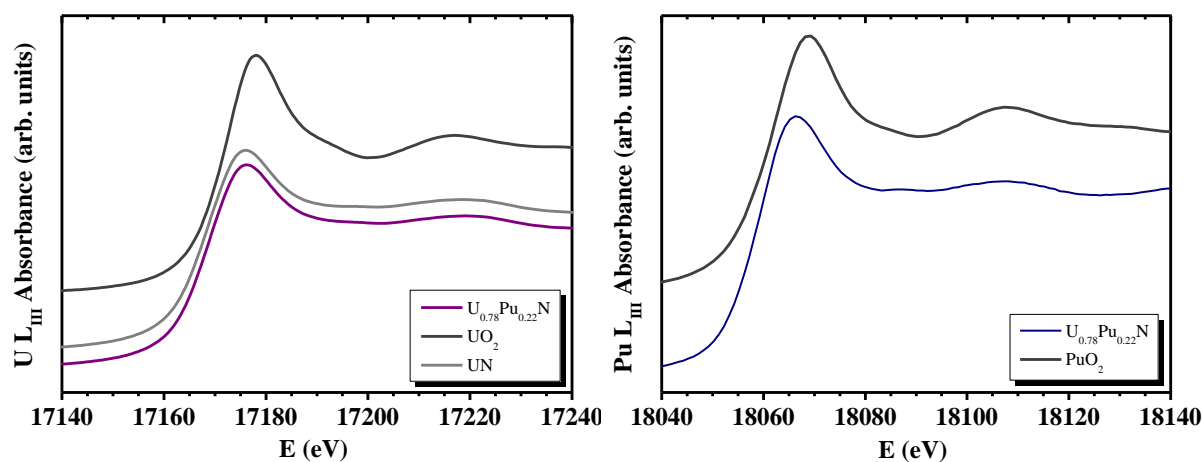
Figure 5.1: XANES spectra of damaged $U_{0.78}Pu_{0.22}N$ NIMPHE fuel at U L_{III} and Pu L_{III} edges (The XANES spectra of UN, UO_2 and PuO_2 are presented as reference materials).

The corresponding energy positions of inflection point and white line are provided in the Table 5.2.

Table 5.2: Energies of the inflection point (IP) and white line (WP) positions of the $U_{0.78}Pu_{0.22}N$ NIMPHE fuel XANES spectra.

	U L_3 edge		Pu L_3 edge	
	IP (eV)	WL (eV)	IP (eV)	WL (eV)
$U_{0.80}Pu_{0.20}N$ damaged	17165.2	17172.1	18059.0	18065.3
UN	17164.8	17172.0	-	-
UO_2	17169.0	17174.0	-	-
PuO_2	-	-	18062.1	18068.8

At the U L_3 edge, one can observed that the shape and the energy position of the damaged $U_{0.78}Pu_{0.22}N$ XANES spectrum are similar to the UN reference materials. Thus the

oxidation state of U in mixed (U,Pu)N is the same as in pure UN. Note that the U valence is not influenced by the presence of Pu, as would have been expected. Comparing with the UO_2 XANES spectra, one can observe a shift of 3.2 eV. At the Pu L_3 edge, a shift of ~ 3 eV toward the lower energies was observed between the XANES spectrum of $U_{0.78}Pu_{0.22}N$ and PuO_2. As a similar shift was reported for PuN and PuO_2 [22], it can be supposed that Pu exhibit the same valence in PuN and (U,Pu)N materials.

5.3.2.   Effect of the self-irradiation

5.3.2.1.   Macroscopical properties

As soon as the sealed pin was open in the inerted glove box, the pellets were submitted to a visual inspection and neither crack nor strain was observed. The geometrical characteristics of the as-synthesized and damaged pellets are presented in Table 5.3.

Table 5.3: Pellet characteristic of the as-synthesized and damaged $U_{0.78}Pu_{0.22}N$ NIMPHE fuel (n.d.: no data; *: data retrieved in the fabrication report).

	Mass (g)	Diameter (mm)	Density (%TD)
As-synthesized *	n.d.	7.163 (7)	81.75 (2.25)
Damaged	3.883 (1)	7.17 (5)	82.4 (5)

Considering the measurement uncertainty, no significant variation of the pellet dimensions (diameter or height) was found, despite an α cumulative dose of ~ 4.5×10^{18} α.g^{-1}. One notes that diameter variation of ~1% has been reported on $U_{0.90}Am_{0.10}O_{2-x}$ pellet for significantly lower doses (~ 3.10^{17} α.g^{-1}) [13,23].

However, some self-irradiation effects could be found by comparing the SEM observations of the as-synthesized and the damaged $U_{0.78}Pu_{0.22}N$ NIMPHE fuel, presented in Figure 5.2 and Figure 5.3, respectively.
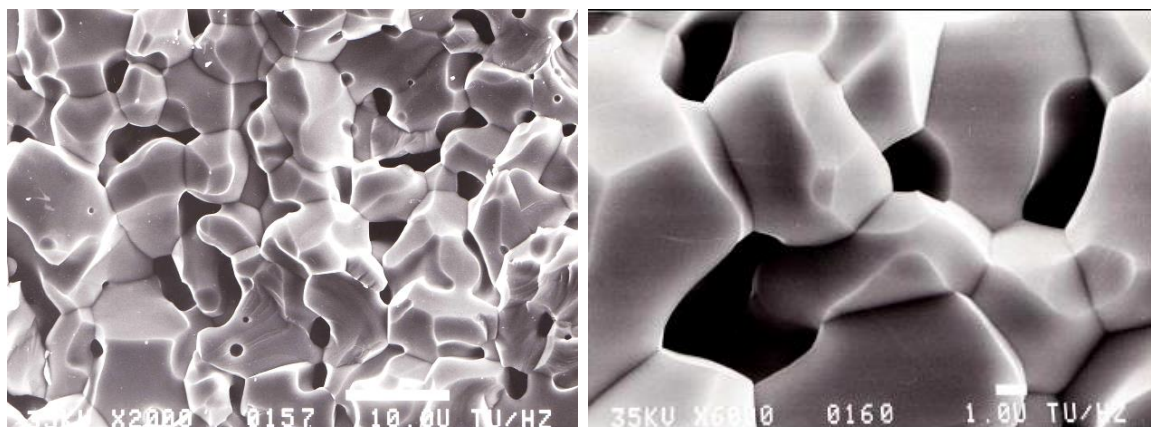
Figure 5.2: SEM observations at 2000x (left) and at 6000x (right) magnification of the as-synthesized $U_{0.78}Pu_{0.22}N$ NIMPHE fuel (data retrieved in the fabrication report).
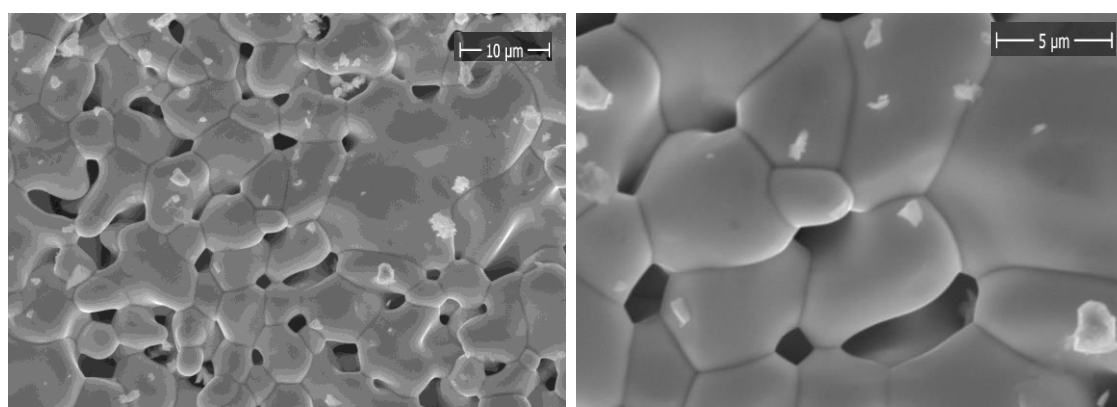
Figure 5.3: SEM observations at 2000x (left) and at 5000x (right) magnification of the damaged $U_{0.78}Pu_{0.22}N$ NIMPHE fuel.

The as-synthesized material exhibits angular-shaped grains while the grains of the damaged compound exhibit a more rounded-shaped grain structure. No significant variation of the grain size was found, indicating that no division into subgrains occurs with self-irradiation. The effect on the grain size of the experimental preparation could be excluded as the samples were neither crushed nor ground before the SEM measurements.

5.3.2.2.   *Microstructure*

From the data retrieved in the fabrication report, the as-synthesized $U_{0.78}Pu_{0.22}N$ material exhibited a rocksalt type (*Fm-3m*) solid solution with a lattice parameter equal to 4.893 (1) Å. According to the XRD pattern presented in the Figure 5.4, a single peak derived from one rocksalt type phase has also been observed for the damaged $U_{0.78}Pu_{0.22}N$ compound.
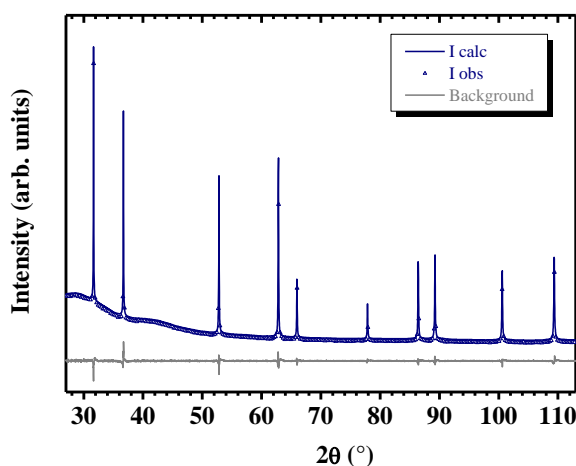
Figure 5.4: XRD pattern of the damaged $U_{0.78}Pu_{0.22}N$ NIMPHE fuel.

As a solid solution was maintained after 25 years of storage, one can conclude that the self-irradiation has not resulted in neither allotropic transition nor phase transformation, contrary to that already been reported in other systems [7]. The lattice parameter of the damaged $U_{0.78}Pu_{0.22}N$ sample is equal to 4.9086 (1) Å. Comparison with the value derived for the as-synthesized compound yields a lattice parameter increase of 0.32(5) %. Okamoto et al. [24] have reported a value of 0.254% for PuN after 800 days of self-irradiation. Studies on the effects of the self-irradiation in fluorite oxides suggest that this value of 0.3 % could correspond to a saturation value for the lattice parameter [8,25,26]. The slight expansion of the lattice parameter can be understood from self-irradiation ballistic effects and associated elastic collisions which result in atomic displacements and defect formations [10,27]. To complete the XRD analyses, EXAFS measurements have been performed on the damaged materials to probe the local environment of U and Pu cations.

In accordance with the XRD results and as described in the experimental section, both U L_{III} and Pu L_{II} EXAFS spectra were fitted considering a NaCl type structure (*Fm-3m*). The experimental and fitted EXAFS spectra are presented in the Figure 5.5.
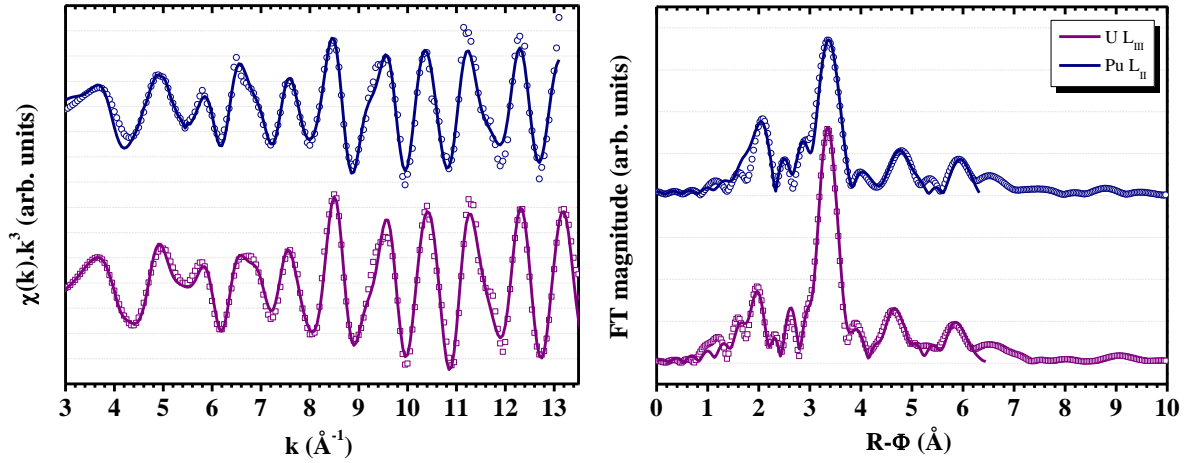
Figure 5.5: U L_{III} and Pu L_{II} k^3-weighed EXAFS spectra of damaged $U_{0.78}Pu_{0.22}N$ NIMPHE fuel.

A good agreement between the experimental and fitted data is observed, confirming the validity of the structural model used for the analysis. No additional Me-N or Me-Me distances were needed to reproduce the experimental data, confirming the complete local integration of Pu in the rocksalt structure. Considering the experimental uncertainty, this shows that the anion and cation atoms are still located on the atomic positions of the NaCl structure type, i.e. no atoms ejected in interstitial positions through the energy of the self-irradiation process could be detected. The crystallographical parameters derived from the EXAFS fitting are provided in the Table 5.4.

Table 5.4: Crystallographical parameters derived from the fitting of k^3-weighed U L_{III} and Pu L_{II} EXAFS analysis (Me: U or Pu cations).

Edge	Shell	R (Å)	N	σ^2 (Å^2)
U L_{III}	N_1	2.440 (5)	5.5 (5)	0.007 (1)
k range : 3.0 – 13.9 Å^{-1}	Me_1	3.475 (5)	11.8 (5)	0.004 (1)
R-factor : 1.4	Me_2	4.90 (1)	8.1 (5)	0.006 (1)
	Me_3	6.02 (2)	24	0.008 (1)
Pu L_{II}	N_1	2.471 (5)	5.9 (5)	0.008 (1)
k range : 3.0 - 12.8 Å^{-1}	Me_1	3.472 (5)	11.9 (5)	0.005 (1)
R-factor : 2.1	Me_2	4.93 (1)	8.0 (5)	0.006 (1)
	Me_3	6.03 (3)	24	0.009 (1)

The EXAFS data analysis provides element-specific Me - N bond lengths. Indeed, the first U - N_1 interatomic distance is equal to 2.440 (5) Å while the Pu – N_1 is about 0.03 Å higher. Besides, the U – N_1 distance is consistent with previous EXAFS measurement on UN [19]. This bimodal distribution in the cation sublattice was expected, as different U-N_1 and Zr-N_1 bond lengths have been reported for analogous (U,Zr)N compounds [20]. One should note that equal U-O_1 and Pu-O_1 interatomic distances have been observed in only $U_{0.50}Pu_{0.50}O_2$. Indeed, a multimodal distribution, explained by the presence of cuboctahedral oxygen defects, was reported for mixed oxides with lower content of Am (> 30%) [28]. This difference of distribution in mixed uranium-plutonium oxides and nitrides can be understood from the difference of structures, namely fluorite-type and rocksalt-type. Thus, different coordination and free sites in the lattice, accommodate the doping cations differently. Those slight discrepancies are only observed in the closest environment, i.e. the first metal-anion distances.

Contrary to the first Me-N_1 shell, one can notice in the Me-Me shell that the U or Pu bond lengths with the first, second and third Me neighbors are very close (~ 3.47, ~ 4.93 and ~ 6.03 Å). This suggests the presence of a homogeneous solid solution without any cluster formation, since both Me_2 and Me_3 atoms are located in the neighbouring unit cells. As shown in Table 5.5, these interatomic distances are consistent with those derived from the XRD lattice parameter.

Table 5.5: Interatomic distances of the as-synthesized and damaged $U_{0.78}Pu_{0.22}N$ NIMPHE fuel (*: data calculated from the XRD lattice parameter, **: data calculated by weighing the $U - Me$ and $Pu - Me$ distances).

	As-synthesized	Damaged	
	R_{XRD} (Å)	R_{XRD} (Å)	R_{EXAFS} (Å)
Me - N_1	2.45 *	2.45 *	2.446 (5) **
Me - Me_1	3.46 *	3.47 *	3.474 (5) **
Me - Me_2	4.893 (1)	4.9086 (1)	4.91 (1)

Comparing with the values calculated by XRD for the as-synthesized material, one can detect a small increase of the Me-Me_1 and Me-Me_2 interatomic distances beyond the experimental uncertainty. Besides this is in agreement with the XRD results which showed an increase of 0.3 % of the lattice parameter. Note that an increase of the first Me-N distance can not be observed considering the experimental error.

Although the ease of the formation of vacancies in the N sublattice has been found before [29], the coordination numbers are close to the theoretical value of the perfect NaCl type structure, indicating that no vacancies were formed in the cation sublattice. Although some precautions must be taken considering the uncertainty, the present EXAFS analysis does not seem to show the presence of vacancy clusters. The formation of such defects has already been encountered with self-irradiation [30]. The Debye-Waller factors are comparable with those derived for the as-synthesized UN material [19]. Indeed, the derived values are relatively low indicating that the structure is relatively ordered.

TEM measurements were performed on the $U_{0.78}Pu_{0.22}N$ sample. Figure 5.6 shows a TEM bright field image displaying the presence of some defect clusters (black dots) but no additional extended defects (dislocations).
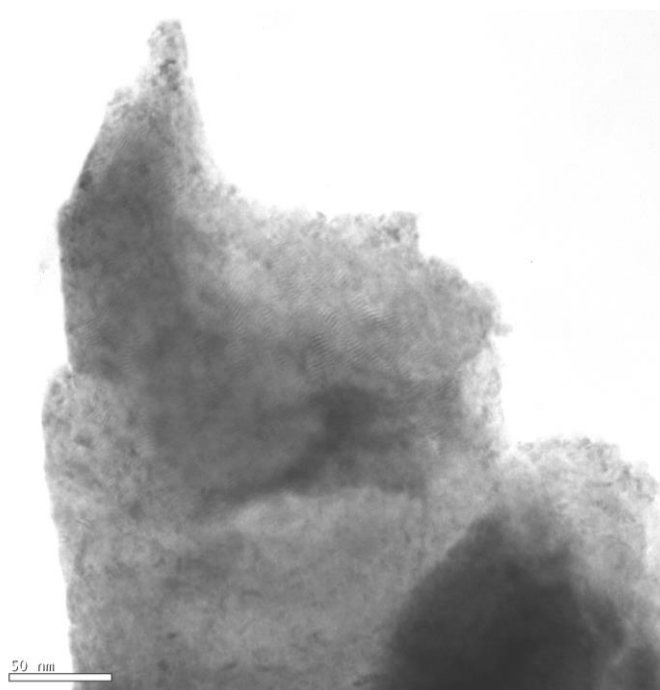
Figure 5.6: TEM bright field image showing the presence of some defect clusters (black dots) but no further extended defects (dislocations). Some oxidation occurred as seen by the presence of a wavy structure on some areas.

Some superficial oxidation (identified by EELS) occurred most probably during TEM sample preparation seen by the presence of a wavy structure on some areas In Figure 5.7, the high resolution TEM bright field image shows the presence of very few defects.
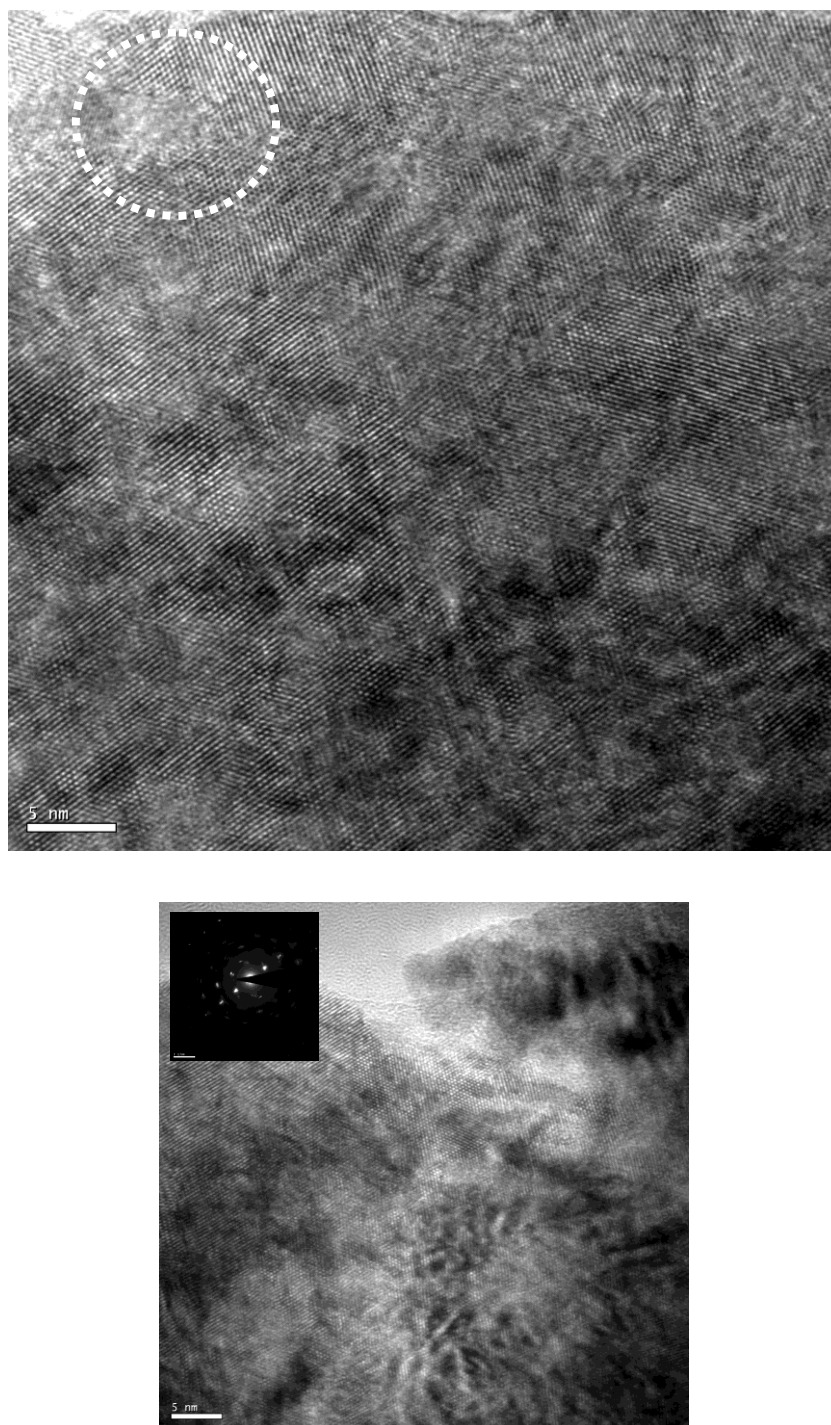
Figure 5.7: High resolution Transmission Electron Microscopy bright field image showing the presence of very few defects (up). The dotted circled area is, however, more de-organized as shown also by the corresponding FFT compared to the one of the global area (bottom).

The dotted circled area is, however, more de-organized as shown also by the corresponding Fast Fourier Transform (FFT) (see inset Figure 5.7 (bottom) on the top) compared to the one of the global area. Such areas were found scarcely in the investigated areas. In addition to the lack of damage, precipated nanometer sized helium bubbles were found in the TEM bright field image (underfocused) in Figure 5.8.
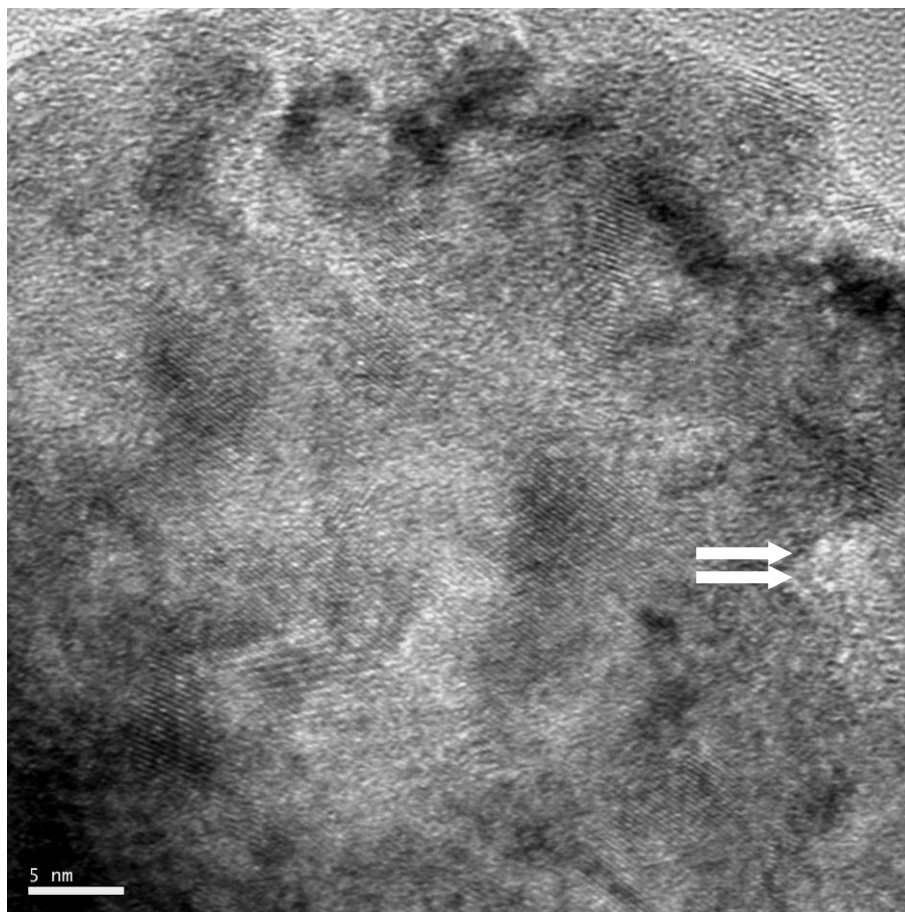
Figure 5.8: TEM bright field image (underfocused) showing the presence of helium bubbles with nanometric sizes (white arrow).

The overall observation is that little damage is observed for an alpha-dose having produced ~ 1.2 dpa. Similar studies have been performed on U/Pu oxides with comparable damage rates [31]. The formation of dislocation loops has been observed as a consequence of the alpha-damage for doses ranging between 0.01 and 4 dpa. Also helium bubbles have been observed in these mix-oxides for similar alpha-doses. The nitride sample shows even a better

resistance to damage build-up or a better recombination of defects. This result is in very good agreement with both XRD and EXAFS measurements.

Despite the intrinsic differences, comparing the present experimental data with those on conventional uranium-plutonium mixed oxide would have been of great interest, but no strictly comparable study on $(U,Pu)O_2$ materials exist. Based on several studies, the fluorite [32–34] and the rocksalt [35] structures have proven exceptional stability to irradiation and that similar stability behavior toward fission products was found [36]. The present work shows that the rocksalt structure accommodates perfectly the presence of various cations with different ionic radii, as it has already been extensively observed in the fluorite structure [28,37–39].

5.4.   Conclusion

In the framework of the NIMPHE program, $U_{0.78}Pu_{0.22}N$ pellets were fabricated by the direct pressing method in 1987. These materials were retrieved from the ITU archive after 25 years.

Coupled XRD and EXAFS measurements have shown that the self-irradiation leads to a slight increase of the interatomic distances and ultimately to an expansion of 0.3 % of the lattice parameter. From the TEM analyses it could be shown that the nitride material exhibits a good radiation tolerance. Few extended defects were observed but the formation of nanometric He bubbles was observed as it is the case for equivalent self-damaged oxides.

5.5.   References

[1]   Kolokol, A. S.; Shimkevich, A. L. In *International Conference on Nuclear Engineering, Proceedings, ICONE*; 2008; Vol. 1, pp. 759–763.

[2]   Meyer, M. K.; Fielding, R.; Gan, J. *Journal of Nuclear Materials* 2007, *371*, 281–287.

[3]   Delage, F.; Carmack, J.; Lee, C. B.; Mizuno, T.; Pelletier, M.; Somers, J. *Journal of Nuclear Materials*.

[4]   Fernandez, A.; McGinley, J.; Somers, J.; Walter, M. *Journal of Nuclear Materials* 2009, *392*, 133–138.

[5]   Thiebaut, C.; Baclet, N.; Ravat, B.; Giraud, P.; Julia, P. *Journal of Nuclear Materials* 2007, *361*, 184–191.

[6]   Walter, M.; Somers, J.; Fernandez, A.; Haas, D.; Dardenne, K.; Denecke, M. A. *Journal of Nuclear Materials* 2007, *362*, 343–349.

[7]   Martin, P. M.; Belin, R. C.; Valenza, P. J.; Scheinost, A. C. *Journal of Nuclear Materials* 2009, *385*, 126–130.

[8]   Hurtgen, C.; Fuger, *J. Inorg. Nucl. Chem. Letters* 1977, *13*, 179–188.

[9]   Jankowiak, A.; Maillard, C.; Donnet, L. *Journal of Nuclear Materials* 2009, *393*, 87–91.

[10] Ewing, R. C.; Weber, W. J.; Clinard, F. W. *Progress in Nuclear Energy* 1995, *29*, 63–127.

[11] Wiss, T. In *Comprehensive Nuclear Materials*; Rudy J.M. Konings, Ed.; Elsevier: Oxford, 2012; pp. 465–480.

[12] Deschanels, X.; Picot, V.; Glorieux, B.; Jorion, F.; Peuget, S.; Roudil, D.; Jégou, C.; Broudic, V.; Cachia, J. N.; Advocat, T.; Den Auwer, C.; Fillet, C.; Coutures, J. P.; Hennig, C.; Scheinost, A. *Journal of Nuclear Materials* 2006, *352*, 233–240.

[13] Prieur, D.; Jankowiak, A.; Roudil, D.; Dubois, S.; Leorier, C.; Herlet, N.; Dehaudt, P.; Laval, J.-P.; Blanchart, P. *Journal of Nuclear Materials* 2011, *411*, 15–19.

[14] Staicu, D.; Wiss, T.; Rondinella, V. V.; Hiernaut, J. P.; Konings, R. J. M.; Ronchi, C. *Journal of Nuclear Materials* 2010, *397*, 8–18.

[15] Richter, K.; Gueugnon, J.; Kramer, G.; Sari, C.; Werner, P. *Nucl. Technol.; (United States)* 1985, *70:3*.

[16] Ziegler, J. F.; Ziegler, M. D.; Biersack, J. P. *Nuclear Instruments and Methods in Physics Research Section B: Beam Interactions with Materials and Atoms* 2010, *268*, 1818–1823.

[17] Ravel, B.; Newville, M. *Journal of Synchrotron radiation* 2005, *12*, 537–541.

[18] Rehr, J. J.; Kas, J. J.; Prange, M. P.; Sorini, A. P.; Takimoto, Y.; Vila, F. *Comptes Rendus Physique* 2009, *10*, 548–559.

[19] Poineau, F.; Yeamans, C. B.; Silva, G. W. C.; Cerefice, G. S.; Sattelberger, A. P.; Czerwinski, K. R. *Journal of Radioanalytical and Nuclear Chemistry* 2011, *292*, 989–994.

[20] Walter, M.; Somers, J.; Fernández-Carretero, A.; Rothe, J. *Journal of Nuclear Materials* 2008, *373*, 90–93.

[21] Wiss, T.; Thiele, H.; Janssen, A.; Papaioannou, D.; Rondinella, V. V.; Konings, R. J. M. *JOM* 2012, *64*, 1390–1395.

[22] Conradson, S. D.; Abney, K. D.; Begg, B. D.; Brady, E. D.; Clark, D. L.; Den Auwer, C.; Ding, M.; Dorhout, P. K.; Espinosa-Faller, F. J.; Gordon, P. L.; Haire, R. G.; Hess, N. J.; Hess, R. F.; Keogh, D. W.; Lander, G. H.; Lupinetti, A. J.; Morales, L. A.; Neu, M. P.; Palmer, P. D.; Paviet-Hartmann, P.; Reilly, S. D.; Runde, W. H.; Tait, C. D.; Veirs, D. K.; Wastin, F. *Inorganic Chemistry* 2004, *43*, 116–131.

[23] Prieur, D.; Jankowiak, A.; Leorier, C.; Herlet, N.; Donnet, L.; Dehaudt, P.; Lechelle, J.; Laval, J.-P.; Blanchart, P. *Ad. in Sc. and Tech.* 2010, *73*, 104–108.

[24] Okamoto, Y.; Maeda, A.; Suzuki, Y. *Journal of Nuclear Materials* 1993, *206*, 94–96.

[25] Prieur, D.; Jankowiak, A.; Leorier, C.; Herlet, N.; Donnet, L.; Dehaudt, P.; Maillard, C.; Laval, J.-P.; Blanchart, P. *Powder Technology* 2011, *208*, 553–557.

[26] Takano, M.; Akabori, M.; Arai, Y. *Journal of Nuclear Materials* 2011, *In Press, Corrected Proof.*

[27] Lang, M.; Zhang, F.; Zhang, J.; Wang, J.; Lian, J.; Weber, W. J.; Schuster, B.; Trautmann, C.; Neumann, R.; Ewing, R. C. *Nuclear Instruments and Methods in Physics Research Section B: Beam Interactions with Materials and Atoms* 2010, *268*, 2951–2959.

[28] Martin, P.; Grandjean, S.; Valot, C.; Carlot, G.; Ripert, M.; Blanc, P.; Hennig, C. *Journal of Alloys and Compounds* 2007, *444-445*, 410–414.

[29] Jhi, S.-H.; Louie, S. G.; Cohen, M. L.; Ihm, J. *Phys. Rev. Lett.* 2001, *86*, 3348–3351.

[30] Ackland, G. *Science* 2010, *327*, 1587–1588.

[31] Jonnet, J.; Van Uffelen, P.; Wiss, T.; Staicu, D.; Rémy, B.; Rest, J. *Nuclear Instruments and Methods in Physics Research B* 2008, *266*, 3008–3012.

[32] Garrido, F.; Vincent, L.; Nowicki, L.; Sattonnay, G.; Thomé, L. *Nuclear Instruments and Methods in Physics Research Section B: Beam Interactions with Materials and Atoms* 2008, *266*, 2842–2847.

[33] Thomé, L.; Moll, S.; Debelle, A.; Garrido, F.; Sattonnay, G.; Jagielski, J. *Advances in Materials Science and Engineering* 2012, *2012*.

[34] Matzke, H.; Lucuta, P. G.; Wiss, T. *Nuclear Instruments and Methods in Physics Research Section B: Beam Interactions with Materials and Atoms* 2000, *166–167*, 920–926.

[35] Beauvy, M.; Dalmasso, C.; Iacconi, P. *Nuclear Instruments and Methods in Physics Research Section B: Beam Interactions with Materials and Atoms* 2006, *250*, 137–141.

[36] Bévillon, É.; Ducher, R.; Barrachin, M.; Dubourg, R. *Journal of Nuclear Materials* 2012, *426*, 189–197.

[37] Carvajal-Nunez, U.; Prieur, D.; Vitova, T.; Somers, J. *Inorg. Chem.* 2012, *51*, 11762–11768.

[38] Prieur, D.; Martin, P.; Lebreton, F.; Delahaye, T.; Banerjee, D.; Scheinost, A. C.; Jankowiak, A. *Journal of Nuclear Materials* 2013, *434*, 7.

[39]   Hubert, S.; Purans, J.; Heisbourg, G.; Moisy, P.; Dacheux, N. Inorg. Chem. 2006, 37, 3887–3894.

Chapter 6

Coupling XRD, EXAFS and ^{13}C NMR to Study the Effect of the Carbon Stoichiometry on the Local Structure of UC$_{1±x}$

ABSTRACT

A series of uranium carbide samples, prepared by arc melting with a C/U ratio ranging from 0.96 to 1.04, has been studied by X-Ray Diffraction (XRD), ^{13}C Nuclear Magnetic Resonance (NMR) and by Extended X-ray Absorption Fine Structure (EXAFS). XRD determines phase uniqueness and the increase of the lattice parameter versus the carbon content. In contrast, ^{13}C NMR detects the different carbon environments in the lattice and in this study, clearly identifies the presence of discrete peaks for carbon in the octahedral lattice site in UC and an additional peak associated with excess carbon in hyperstoichiometric samples. Two peaks associated with different levels of carbon deficiency are detected for all hypostoichiometric compositions. More than one carbon environment is always detected by ^{13}C NMR. This exemplifies the difficulty in obtaining a perfect stoichiometric uranium monocarbide UC$_{1.00}$. The ^{13}C MAS spectra of uranium carbides exhibit the effects due to carbon content on both the broadening of the peaks and on the Knight shift. An abrupt spectral change occurs between hypo- and hyperstoichiometric samples. The results obtained by EXAFS highlight subtle differences between the different stoichiometries and in the

hyperstoichiometric samples EXAFS results are consistent with the excess carbon atoms being in the tetrahedral interstitial position.

6.1.   Introduction

A full understanding of nuclear fuels is essential to predict their safe behaviour in nuclear power plants. Both characterization and modelling play an important role in this field and thanks to the progress in analytical methods the long-term goal comes closer. Uranium carbides have been widely investigated as advanced nuclear fuels [1] since they present several safety-related advantages compared to oxides fuels [2]. Among others, these materials exhibit a higher thermal conductivity [3], a higher metal loading and lower moderation during irradiation [4]. A higher safety margin is achieved by their operation at about 40% of their melting temperature, in contrast to 80% for oxide fuels [5,6,7]. Despite these advantages, the use of uranium carbides has been limited due to the difficulties associated with their synthesis [1]. Indeed, the preparation of pure uranium monocarbide, $UC_{1.00}$, is problematic due to its narrow composition limits [8], and the samples are generally classified in two subgroups, i.e. hypo- or hyperstoichiometric carbides samples. Also, due to the carbon loss during the heat treatment, the composition of the sample can vary from one preparation batch to the next, depending on the treatment time and on the temperature [9]. Since these carbides are readily oxidised in the presence of humidity, precautions must be taken during their preparation and storage to prevent their degradation [10,11]. Uranium carbides are commonly prepared by either arc-melting [12] or carbothermic reduction methods [13,14,15]. While arc-melting leads to more homogeneous samples with less oxygen and impurities, the carbothermic reduction is more suitable for large scale synthesis [16]. Hypo- and hyperstoichiometric uranium carbides compounds, noted hereafter as $UC_{1\pm x}$, crystallize with uranium in the face centred cubic positions [8]. Two structural types could be envisaged depending on the location of the carbon atoms in the interstices of this structure. These are the NaCl *(Fm-3m)* or ZnS *(F-43m)* type, where the carbon atoms are located in octahedral or in the tetrahedral sites, respectively [17]. Rundle *et al* [18] have reported that carbon atoms in the cubic structure are located in octahedral interstices. This was confirmed by a recent EXAFS study [19] on UC that showed that the ZnS structural model was not consistent with the EXAFS data. In the case of hypostoichiometric carbides, UC_{1-x}, there are vacancies on the octahedral sites of the

carbon sub-lattice. Structural defects [20], like vacancies or interstitial atoms [21], affect the material properties of fresh samples and during irradiation in reactors, with potential impact on fuel performance and eventually on the safety of the reactor operation. For instance, vacancies lead notably to distortion of the lattice structure and macroscopic swelling [22], eventually altering material properties such as strength and ductility.

In this study, we report the effect of the carbon content on the ordering of the structure at the atomic scale in uranium carbides UC$_{1\pm x}$ (0.96 ≤ "1±x" ≤ 1.04). As uranium monocarbide melts incongruently, the samples obtained by arc melting are quenched, and are not usually annealed. This quenched state induces some disorder in the lattice, and so far, no studies on uranium carbides have reported distributions of vacancies or carbon in the lattice of UC$_{1\pm x}$. Thus, it is essential to evaluate the local environment of the atoms by combining three structural characterization techniques, namely X-Ray Diffraction (XRD), Nuclear Magnetic Resonance (NMR) and X-ray Absorption Spectroscopy (XAS). The new NMR spectrometer at JRC-ITU permits, for the first time, the rapid spinning of the uranium carbide samples and thus high resolution ^{13}C magic angle spinning (MAS) spectra. These results are compared to those obtained by EXAFS to provide a detailed atomistic view of the uranium carbide structures.

6.2.   Experimental section

6.2.1.   Sample preparation and chemical analysis

The uranium carbide samples were prepared by arc melting of the constituent elements, uranium metal and graphite, under a high purity argon atmosphere (6N), on a water-cooled copper hearth. Metallic zirconium in the chamber acts as a getter for oxygen. The UC$_{1\pm x}$ ingots were melted and turned several times to achieve homogenous samples. The weight losses of the initial charges were below 0.5 wt%. The samples were stored under high vacuum to prevent their oxidation [23,24]. An additional heat treatment was carried out on the UC$_{0.96}$ sample at 1450°C for 10 hours under high vacuum (10^{-5} mbar) followed by a cooling rate of 20°C/h.

Chemical analyses of carbon, oxygen and nitrogen contents have been determined by direct combustion using the infrared absorption detection technique with an ELTRA CS-800 instrument.

6.3. X-Ray diffraction

The XRD analysis was performed on a Bruker Bragg-Brentano D8 advanced diffractometer (Cu K$_{\alpha 1}$ radiation) equipped with a Lynxeye linear position sensitive detector. The powder patterns were recorded at room temperature using a step size of 0.01973° with an exposure of 4 s across the angular range $10° \leq 2\theta \leq 120°$. Operating conditions were 40 kV and 40 mA. Lattice parameters were refined by the Le Bail method using the X'Pert HighScore Plus program.

6.4. Nuclear Magnetic Resonance

Uranium carbide ingots were crushed to a fine powder and loaded into 1.3 mm zirconia rotors under helium (6N) in a glove box. The particle size was sufficiently small not to affect the radiofrequency response of the sample due to skin-depth effects. The ^{13}C NMR spectra, with ^{13}C in natural abundance (1.1%), were recorded on a Bruker Advance 400 spectrometer operating at 9.4 T (Larmor frequency of ^{13}C 100 MHz). This apparatus has been adapted for the study of highly radioactive material using commercial NMR probes and rotors [25]. An evacuation tube at the top of the magnet bore, is connected via a HEPA filter to the laboratory ventilation system in order to eliminate the dispersion of radioactive particles in the event of rotor crash. Despite the potential for eddy current effects during spinning of the semi-metallic uranium carbides, ^{13}C MAS NMR spectra could be acquired at spinning rates of 55 kHz. Rotor-synchronised Hahn echoes were used to acquire the spectra. The pulse durations were 2.5 μs ($\pi/2$) and 5 μs (π), respectively, with an echo delay of 18.2 μs (1 rotor period). Fully relaxed spectra could be acquired with a relaxation delay of 150 ms due to the paramagnetic relaxation mechanism provided by the conduction electrons [26]. All spectra were calibrated relative to tetramethylsylane (0 ppm) by using adamantane as a secondary reference, with ^{13}CH and ^{13}CH$_2$ peaks at 29.45 ppm and 38.48 ppm [27], respectively. Due to

safety restrictions on running the MAS NMR system unattended overnight, the number of transients was limited to 51,200 for each spectrum. All the spectra were analysed and fitted using the dmfit software [28].

6.5.　　Extended X-Ray Absorption Fine Structure

The uranium carbides ingots were crushed and milled in an agate mortar under high-purity helium atmosphere (6N) to obtain a small particle size. 5 mg of powdered samples were mixed with 55 mg of boron nitride, as it is transparent to high energy X-rays, and then pressed to obtain pellets of about 5 mm diameter and 1 mm thickness. Each sample was fixed in a plastic holder, then sealed with Kapton® tape in a double bag under argon atmosphere (6N) and stored in a glass bottle also under argon atmosphere (6N) up to the measurements made at the ANKA synchrotron site. The samples were observed by optical microscopy and X-Ray radiography to characterize the homogeneity of the mixture and the absence of cracks. Further they were prepared a short time before the experiment to minimize the risk of oxidation.

X-ray Absorption Spectroscopy (XAS) data were collected at the INE-Beamline at the Angströmquelle Karlsruhe (ANKA) [29]. A Ge(422) double crystal monochromator coupled with a collimating and focusing Rh-coated mirrors was used. XAS spectra were collected in both transmission and fluorescence modes at the U L$_{III}$ (17166 eV) edge. Before averaging scans, each spectrum was aligned using the Y reference foil located between the second and the third ionization chamber. The ATHENA software [30] was used to extract EXAFS oscillations. Experimental EXAFS spectra were Fourier-transformed using a Hanning window over the k-range 2.8 – 12.5 Å^{-1}. The ARTEMIS software [30] was used for the curve fitting in k^{3} space. Both interatomic scattering path phases and amplitudes were calculated using the *ab initio* code FEFF8.20 [31]. Data fitting was performed in k^{3} space for R values ranging from 1.4 to 6.3 Å. The S_0^2 value was set at 0.90 and the shift in threshold energy was varied as a global parameter.

6.6.   Results and discussion

6.6.1.   Structure of UC$_{1\pm x}$ materials

6.6.1.1.   *Chemical Analysis: C, O and N contents*

The chemical analyses made to determine carbon, oxygen and nitrogen contents are summarized in Table 6.1. The uncertainty of the analyses is estimated at 3 wt%, corresponding to an uncertainty in the stoichiometry of uranium carbides of about ± 0.03. Due to this high uncertainty of the chemical analyses relative to the small changes in carbon composition in the samples, it is difficult to give an absolute quantification of the C/U by this method. As expected with arc melting, as a synthesis method, the oxygen content present in the samples is low and is significantly better than can be achieved using the carbothermal reduction method.

Table 6.1: Chemical analysis of the UC$_{1\pm x}$

	UC$_{0.96}$	UC$_{1.00}$	UC$_{1.04}$
Theoretical C content (wt.%)	4.62	4.80	4.99
Measured C content (wt.%)	4.60 (14)	5.00 (15)	4.90 (15)
C/U ratio	0.96 (3)	1.04 (3)	1.02 (3)
O (ppm)	142 (30)	94 (19)	119 (24)
N (ppm)	< 2	< 2	< 2

6.6.1.2.   *XRD*

The XRD patterns of UC$_{1\pm x}$ ("1±x"= 0.96, 1.00, 1.04) samples are displayed in Figure 6.1.
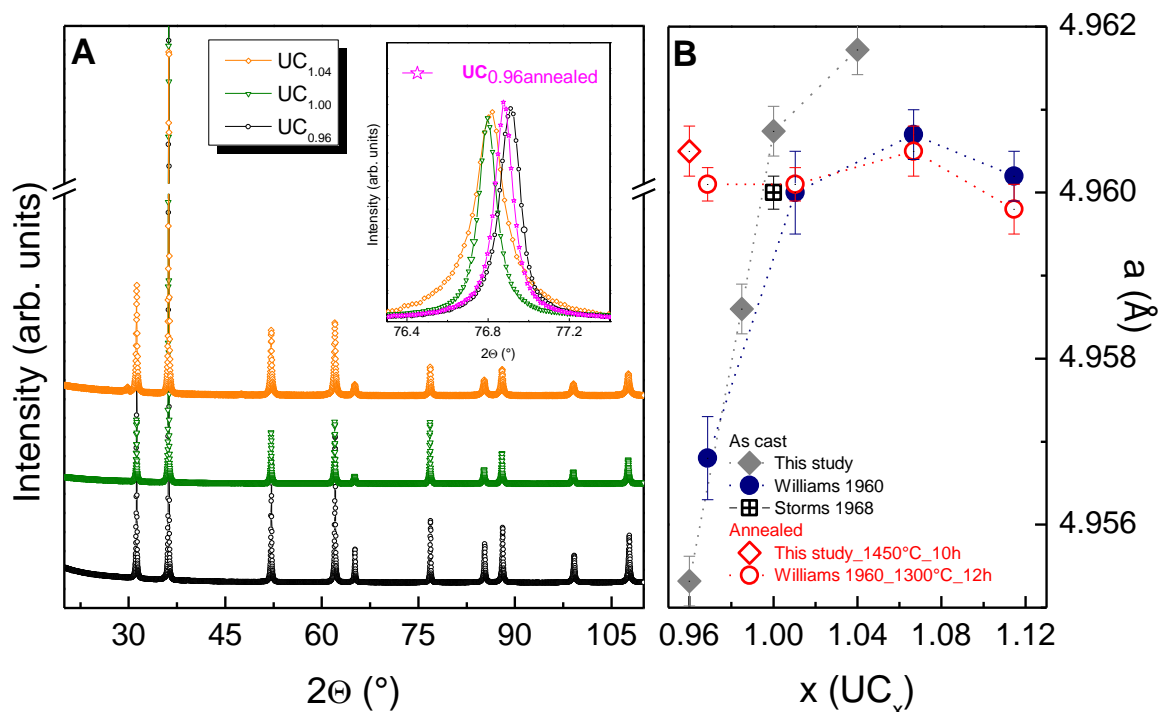
Figure 6.1: A – XRD patterns of the $UC_{1\pm x}$ samples. The inset compares the (400) peak of $UC_{1\pm x}$ as cast samples with a $UC_{0.96}$ annealed sample. B - Lattice parameter (Å) evolution as a function of the C/U ratio [33, 34].

Two structural models can be suggested for the carbon position, NaCl *(Fm-3m)* or ZnS *(F-43m)* types, in which the carbon atoms occupy the octahedral or the tetrahedral sites, respectively. Due to the low scattering factor of the carbon relative to the uranium atoms, and to the small range of C/U composition, Rietveld analysis using X-ray diffraction patterns is not capable of defining the atomic positions of the carbon and its composition in the uranium carbides. Neutron diffraction could be more relevant for this purpose. In this study, XRD defines the quality of the samples in terms of impurities and the crystallinity. Thus all the samples displayed the fcc structure expected for uranium monocarbide and are highly crystalline as shown by the narrow diffraction peaks. Due to the high quality of the measurement, a small peak around $2\theta = 35.6°$ has been detected in the $UC_{0.96}$ sample, which coincides with the highest intensity peak expected for free uranium metal with its orthorhombic structure. Actually, according to the U–C phase diagram [32], U and UC coexist in the hypostoichiometric domain.

The lattice parameters of UC$_{1\pm x}$ samples versus the C/U ratio are plotted in Figure 6.1 and compared with previous values [21,33,34]. In agreement with the literature data, two evolutions of the lattice parameter with the C/U ratio are observed: for C/U < 1.0, there is a linear increase with increasing C/U ratio, and for C/U ≥ 1.0 the lattice parameter remains more constant. The inset in Figure 6.1 shows this evolution in terms of a single diffraction peak. Considering the low amount of oxygen assessed with the chemical analyses, the evolution of the lattice parameter cannot be attributed to the presence of oxygen impurity in these samples. In contrast, an increase of the oxygen content in U carbides leads to a decrease of the lattice parameter [35]. Even if oxygen is very difficult to detect by XRD, the fact that neither broad peaks nor a UO$_2$ phase are observed and the fact that the lattice parameter increases with carbon content, suggests that the oxidation is very limited, in agreement with chemical analyses. To support this statement, XRD measurements were also performed on the samples used for EXAFS experiments after two months storage and no variation of the lattice parameter was detected, confirming the absence of sample oxidation.

6.6.1.3. *NMR*

The specially adapted NMR spectrometer available at the JRC-ITU allows unique, high spinning speed spectra of radioactive samples to be obtained. As the UC$_{1\pm x}$ are semi-metals, large NMR resonance shifts (Knight shifts) are expected due to the collective hyperfine shifts of unpaired electrons near the Fermi surface of these materials [36]. In Figure 6.2, the static and the spinning Hahn echo spectra of the UC$_{1.00}$ sample are compared; the values obtained by fitting the spectra are reported in Table 6.2.
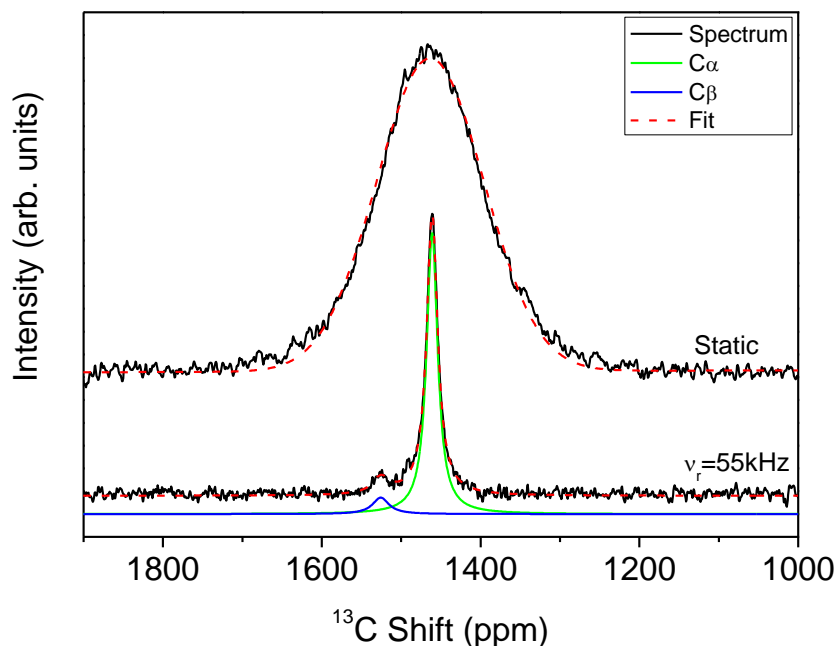
Figure 6.2: Top - ^{13}C static Hahn-echo NMR spectrum of UC$_{1.00}$. Bottom - MAS Hahn-echo NMR spectrum and its corresponding fit (B$_0$ = 9.4 T, ν_r = 55 kHz).

Table 6.2: ^{13}C shift and Full Width at Half Maximum (FWHM) of the UC$_{1\pm x}$ samples.

Compounds	Shift (ppm)		FWHM (ppm) Spinning		FWHM (Hz) Static	
	^{13}C$_\alpha$	^{13}C$_\beta$	^{13}C$_\alpha$	^{13}C$_\beta$	^{13}C$_\alpha$	^{13}C$_\beta$
UC$_{1.04}$	1463	1525	23.1 (2)	35.6 (2)	153.1 (4)	
UC$_{1.00}$	1461	1526	16.7 (2)	25.2 (2)	159.1 (4)	
UC$_{0.96}$	1448	1483	28.5 (4)	108.9 (2)	147.7 (6)	335.7 (2)
UC$_{0.96\ \text{Annealed}}$	^{13}C	1468	25.5 (3)		150.8 (7)	
UC$_{0.985}$	1458	1486	25.5 (3)	101.2 (2)	135.4 (4)	292.5 (1)

First, the ^{13}C static spectrum is characterized by a broad Gaussian with a maximum at 1463 ppm and a full width at half maximum (FWHM) of 16 kHz (159 ppm). The absence of an anisotropic static line shape is consistent with the cubic symmetry around the ^{13}C nucleus. The line-width is, thus, attributed to a range of shifts due to the paramagnetic susceptibility of the UC$_{1.00}$ particles and a distribution of local fields arising from the distribution of particle shapes in the powder. Spinning the sample at very high speed (ω_r=55kHz) results in a sharpening of the peak to give a high-resolution spectrum. This highly resolved spectrum is

composed of one symmetric, purely Lorentzian peak with a chemical shift of 1461 ppm, similar to that observed in the ^{13}C static spectrum, but with a FWHM almost 10 times narrower than the static. This is consistent with the octahedral local environment. A second small purely Lorentzian peak at 1526 ppm is also visible with 4 % of the total signal intensity. Although in a first instance, only one carbon environment is expected in UC$_{1.00}$, the ^{13}C MAS spectrum detects the presence of this second carbon environment, albeit in a very small quantity relative to the main peak. In the recent EXAFS study by Vigier *et al.* [19] on a UC$_{1.00}$ sample whose preparation and lattice parameter are similar the UC$_{1.00}$ sample in this study, the authors propose the presence of one type of carbon in the sample. In NMR a chemically different, second carbon environment can be detected, even in low concentration. Indeed, only the achievement of a perfect crystal with a precise and exact stoichiometry of UC$_{1.00}$ can lead to one single carbon environment. This would be quite an achievement and is challenging due to the difficulty of controlling the final composition of the uranium carbide samples by arc melting. Certainly, weight loss during this preparation can be limited but never avoided completely. The presence of a second carbon environment in hyperstoichiometric UC$_{1\pm x}$ could be expected, and is now detected in the ^{13}C MAS spectrum. Thus, we argue that the main and purely Lorentzian peak observed in the ^{13}C spectrum can be attributed to carbons localized on the octahedral sites of the NaCl structure. The second and smaller Lorentzian peak is due to the presence of excess carbon present in the lattice. The Lorentzian nature of this peak suggests that it represents carbon in a well-defined 'defect environment'. This could be either as C-C dumbbells or as C in the other tetrahedral interstitial positions in the NaCl structure. Previous density functional calculations [20,37] suggest that the first assumption, carbon in the form of a dumbbell, is preferred due to its lower energy of formation. These calculations indicate that the energy of formation of C$_2$ dumbbells having the <111> or <110> orientations is about 2.18 and 2.16 eV respectively, while the formation energy of carbon in interstitial position, is equal to 2.52 eV [37]. The presence of a second peak with 4% intensity suggests that the true composition of the UC$_{1.00}$ is in fact UC$_{1.02}$. This is because the introduction of a C-C dumbbell at the site of a C atom affects two carbon atoms, the original plus the excess carbon. So UC$_{1.02}$ would have 4% of C in these sites.

In Figure 6.3, the ^{13}C MAS spectra of UC$_{0.96,}$ UC$_{0.985}$ and UC$_{1.04}$ are presented and compared with the UC$_{1.00}$ spectrum.
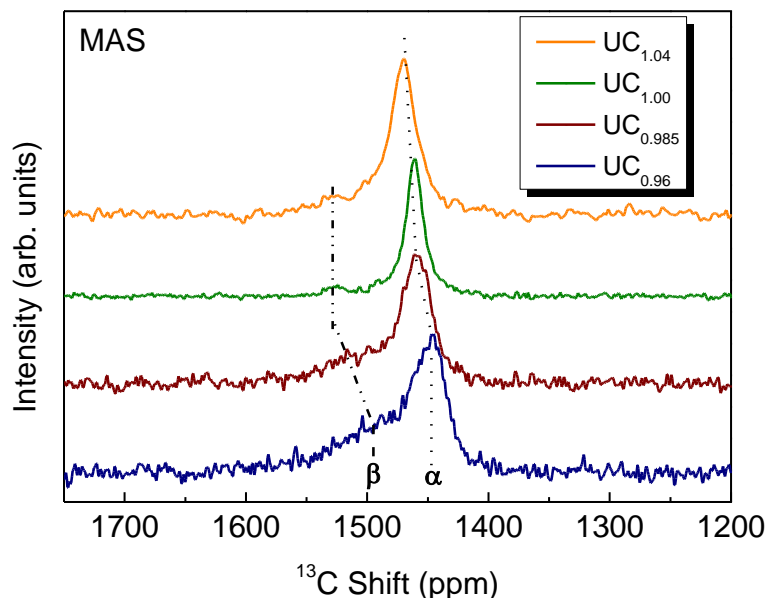
Figure 6.3: ^{13}C Hahn-echo MAS NMR spectra of UC$_{1.04}$, UC$_{1.00}$, UC$_{0.985}$ and UC$_{0.96}$ (B$_0$ = 9.4 T, ν_r = 55 kHz).

For all samples two peaks are observed, the main, and sharper, one will be designated as the α peak, whilst the smaller and broader peak is reported as here as the β peak. Two effects can be observed and are defined by the substitution of excess carbon in the lattice in hyperstoichiometric samples and the absence of carbon from sites in hypostoichiometric UC$_{1\pm x}$. In the former, UC$_{1.00}$ and UC$_{1.04}$ samples exhibit an additional narrow peak at 1527 ppm indicating the presence of a well-defined C defect site. In UC$_{1.04}$ there is also a small amount of additional intensity between these two resonances. In UC$_{0.985}$ and UC$_{0.96}$ broad additional peaks are observed at higher frequency in addition to peaks that are close to the peak for octahedral carbon in the UC lattice. One interpretation of the hypostoichiometric spectra would be that some UC, closer to perfect stoichiometry, is responsible for the sharper peak close to the UC$_{1.00}$ main peak (peak α) and that it is co-existing with more disordered material that produces the broader peaks to higher frequency (peak β). There appears to be a correlation between the increasing paramagnetic shift and peak broadening of the ^{13}C NMR line and the decreasing C content of the UC$_{1-x}$. The origin of this shift would require a detailed electronic structure calculation. However, since the magnitude of the shift is of the

89

order of a hundred ppm for a very small change in C content it is likely to be a Knight shift effect due a change in the density of states at the Fermi level rather than a 'chemical shift' effect. The width of the line is indicative of a range of these isotropic Knight shifts. It is clear that the MAS NMR can narrow a susceptibility-broadened line and the origin of the broadening here is the distribution of local environments. The corresponding static spectrum of UC$_{1\pm x}$ samples, not reported here, as all are characterised by a broad Gaussian peak and the extracted shifts are in a good agreement with the previous ^{13}C static spectrum results, reported by Lewis *et al.* [38], on a sample with a C/U ratio of 1.03.

The resonance shifts and the FWHM of the *α* and *β* MAS NMR peaks versus the composition of the uranium carbide samples are shown graphically in Figure 6.4.
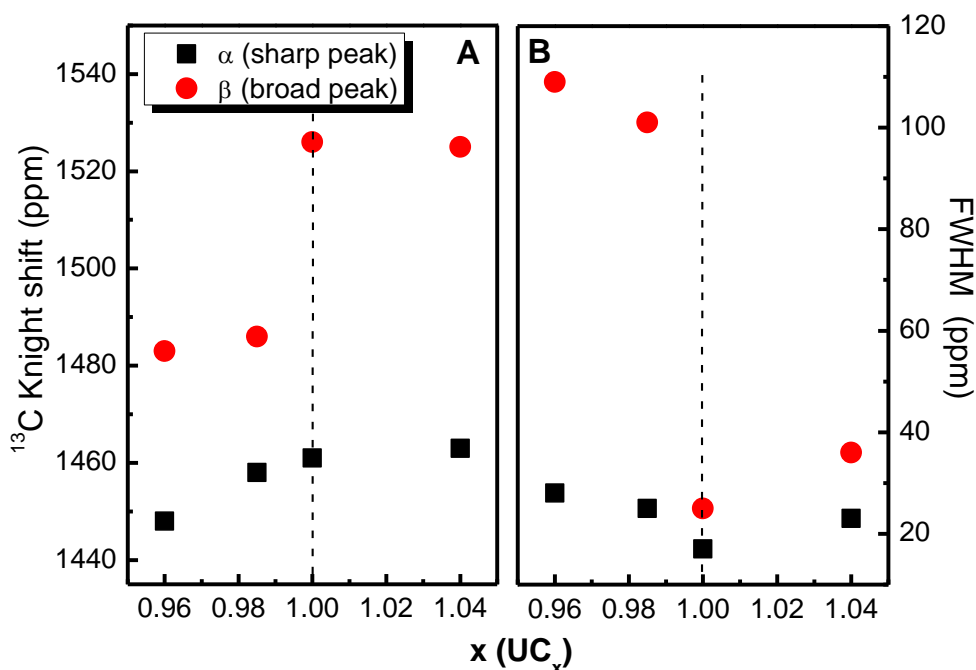
Figure 6.4: A - Evolution of the ^{13}C NMR shift as a function of the C/U ratio. B - Evolution of the FWHM as a function of the C/U ration. The dotted line at C/U = 1.00 indicates the transition from high to low FWHM value corresponding to a transition to more ordered sample.

The trend of shifts to higher frequencies for lower C contents are present for both peaks, but are more emphasized for the *β* peak. One can assume that the broad *β* peaks, in hypostoichiometric samples can be attributed to carbon atoms, which are surrounded by

vacancies in the next carbon shell [39]. Carbon-13 NMR is thus a potentially powerful probe of the change in carbon local environments in the transition from hypo- to hyperstoichiometric uranium carbides.

6.6.1.4.   *EXAFS*

According to the above NMR results, two C environments are systematically observed for each $UC_{1\pm x}$ material. In the case of $UC_{0.96}$ and $UC_{0.98}$, the presence of vacancies might explain this. Regarding the $UC_{1.00}$ and $UC_{1.04}$, one can assume that there is an excess of carbon atoms located either in interstitial or in dumbbell position. Therefore to investigate further these materials, the local structure around U atoms was investigated by EXAFS, in addition to the C environment, as studied by NMR.

The Figures 6.5 and 6.6 present the U L_{III} experimental k^3-weighted EXAFS spectra and the corresponding Fourier transforms (FTs) of $UC_{0.96}$, $UC_{1.00}$ and $UC_{1.04}$ materials.
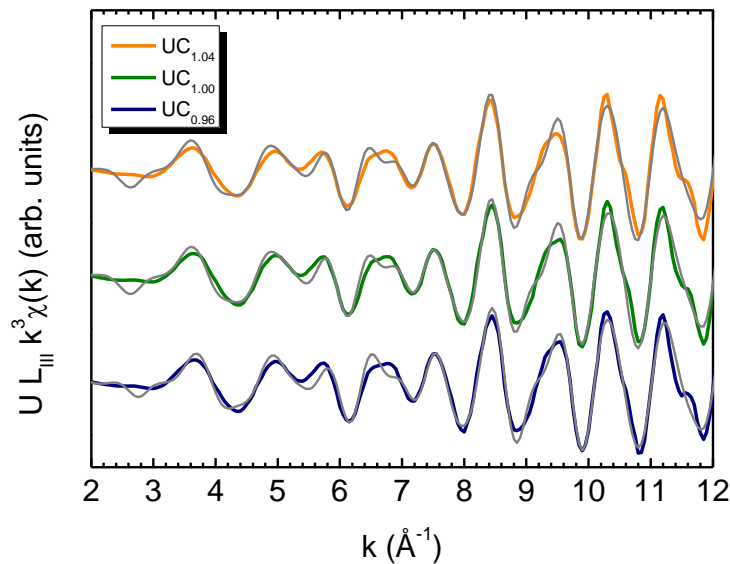
Figure 6.5: Experimental and fitted $k^3 \chi(k)$ EXAFS spectra at the UL_{III} edge (the grey lines represent the fit).

(a)

(b)

(c)
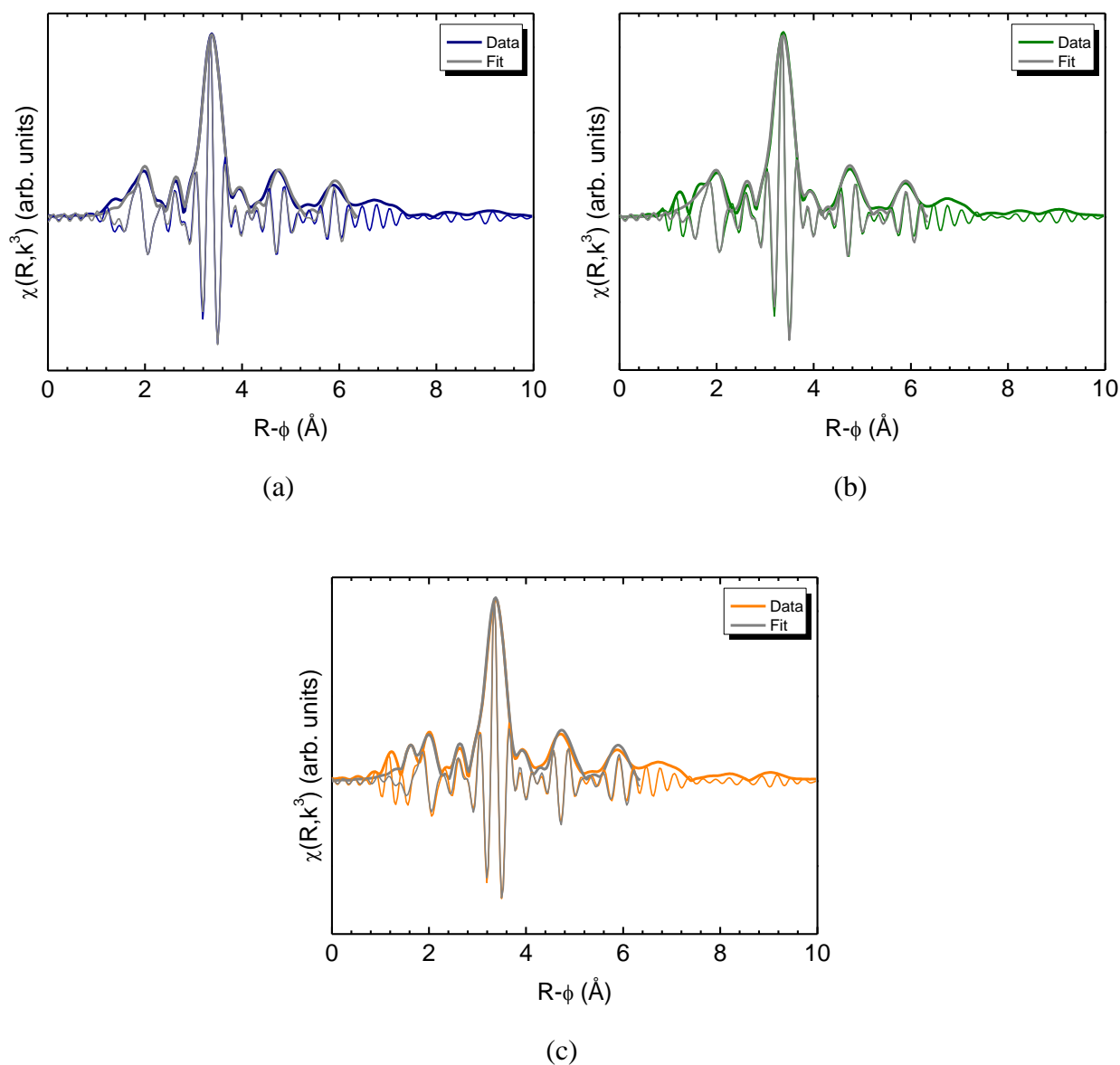
Figure 6.6: Modulus and real part of Fourier transforms of k^3-weighted EXAFS spectra at the UL$_{III}$ edge (a : UC$_{0.96}$; b : UC$_{1.00}$; c : UC$_{1.04}$).

Three intense peaks are observed in the FTs. The first at ~2.0 Å is due to the first C shell, the second at ~3.3 Å corresponds mostly to the first U neighbour atoms and the third peak at ~4.8 Å is attributed to multiple scattering paths.

As mentioned above, the NaCl type structure was clearly established for UC$_{1.00}$ [19] but the ZnS structure (F-43m) has not been completely discarded for non-stoichiometric

UC$_{1\pm x}$ compounds. Although the XRD results of the present paper suggest that UC$_{0.96}$ and UC$_{1.04}$ have actually the rocksalt structure, EXAFS should be able to confirm this assumption; this method is more sensitive to the local atomic range than XRD. Thus, NaCl and ZnS structural type EXAFS spectra of U were simulated with FEFF8.20[31] and are plotted in Figure 6.6. Significant discrepancies between NaCl and ZnS simulated EXAFS spectra are observed in the k range from 4 to 7 Å^{-1}. The oscillation at 4.8 Å^{-1} is shifted significantly, as shown by the vertical line in Figure 6.7.
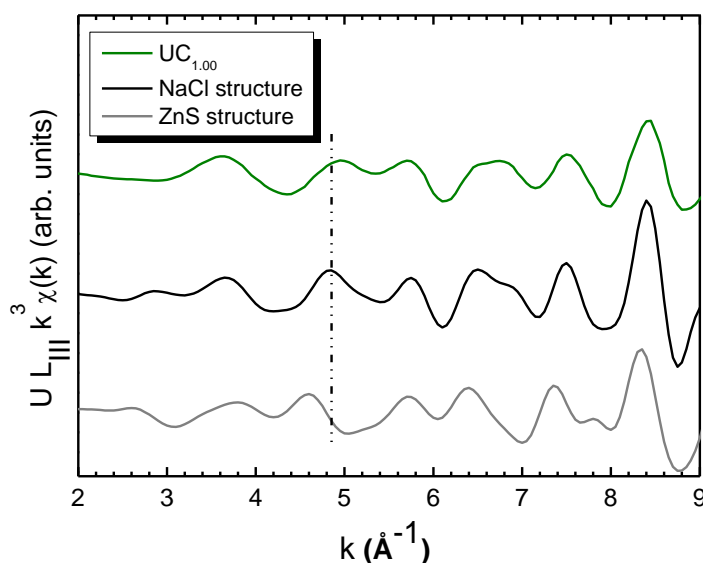
Figure 6.7: Experimental $\chi(k)k^3$ EXAFS spectrum of UC$_{1.00}$ compared with the simulated spectra based on NaCl and ZnS structural types. The dotted line evidences the significant discrepancy between the NaCl structure of UC$_{1.00}$ and the ZnS structure.

The comparison of these data with the experimental data collected on the UC$_{1.04}$ sample confirms that the non-stoichiometric UC$_{1\pm x}$ exhibit the rocksalt structure too.

For all the materials, one can assume that the presence of clustered defects can be discarded as no constant decrease of the amplitude of the experimental FTs EXAFS spectra is observed across the full R range. Actually, a particular amplitude decrease is observed at long distance. Indeed, the amplitude of the peaks does not decrease monotonically; this is particularly true for R values superior to 7.4 Å, where no peak can nearly be observed. This could support the presence of randomly distributed defects. Although the FTs are very similar, the region between 1.5 and 2.0 Å exhibits slight, but nevertheless, significant differences. Indeed, no peak is observed at ~1.8 Å for UC$_{0.96}$ while a small, but distinct, peak is detected at

this distance for both the $UC_{1.00}$ and $UC_{1.04}$ samples. This suggests the presence of two first U – C distances instead of one, as would be expected in a perfect rocksalt structure. Further, this bimodal environment is consistent with the two environments detected by NMR. Note that the peak amplitude increases with C content.

The splitting of the UC first neighbour shell is more apparent for the $UC_{1.04}$ sample. Figure 6.8 compares the experimental FT with various FTs calculated using different structural models.
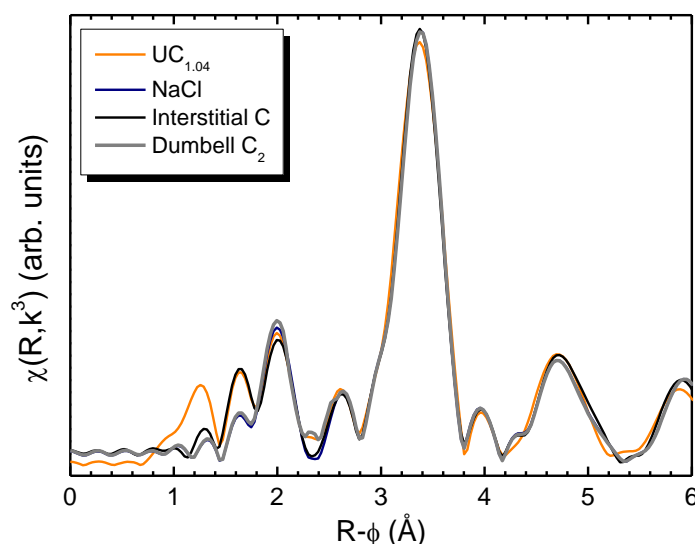
Figure 6.8: Modulus of Fourier transforms of $UC_{1.04}$ and fitted spectra using a perfect Fm-3m structure type, a Fm-3m structure type containing tetrahedral C interstitials and a Fm-3m structure containing C_2 dumbbells.

Firstly, considering a perfect NaCl type structure for the data fitting, the small peak at ~1.8 Å is not replicated at all. Indeed, evidence for two C environments, one of them being different to the NaCl structure, has been found and it has been assumed that the carbon can therefore occupy either interstitial or dumbbells positions. Therefore, the presence of C_2 dumbbell pairs, as defects in the structure, has been considered. In the case of the fit with dumbbell, the best fit was achieved by considering a mixture of a pure NaCl structure and a NaCl structure with one dumbbell per unit. Various concentrations, configurations (α-UC_2 [8, 39] and β-UC_2[40]) and orientations (<110>, <111> [37]) have been taken into account. Figure 6.7 presents only the best result achieved including excess carbon in dumbbell

configurations. One can note that the small peak at ~1.8 Å is still not replicated. Based on geometrical considerations, the presence of dumbbells in this type of material should result in the appearance of a multimodal distribution of the first U-C distance. The presence of carbon in interstitial positions was then considered and a significant improvement of the fit was observed, especially in the 1.8 Å region as shown in Figure 6.7. Using this structural model (NaCl structural with interstitial), the small peak is well fitted. Therefore, the present EXAFS study strongly suggests that excess carbon is accommodated on interstitial sites. As a consequence, such occupancy of such interstitial atomic positions was taken into account to fit the EXAFS spectra of UC$_{1.00}$ and UC$_{1.04}$.

In addition to the experimental data, the Figures 6.5 and 6.6 present the calculated and fitted k^3-weigthed EXAFS spectra and the associated FTs. In the fitting procedure, a model cluster (NaCl type) with a lattice parameter of 4.96 Å was considered in the FEFF calculations. The coordination number of the first U-C shell was allowed to vary but for the other shells this parameter was fixed according to the rocksalt structure. For UC$_{0.96}$, neither an additional distance nor an additional carbon position was included in the fitting procedure. For both UC$_{1.00}$ and UC$_{1.04}$, the presence of excess carbon in interstitial positions was permitted. Multiple scattering paths were considered, e.g. triangular triple paths and quadruple paths from the C and U first neighbours. Table 6.3 summarizes the crystallographical parameters derived from the FEFF calculations.

Table 6.3. Crystallographic parameters derived from the U L_{III} EXAFS spectra (R: interatomic distance; N: number of neighbours; σ^2: Debye-Waller factor, U - U_1: distance U-U in the first shell, U - C_{1a} and U - C_{1b}: first and second distance U - C in the first shell).

Shell	R (Å)	N	σ^2 (Å^2)	R factor (%)
Uranium carbide UC$_{0.96}$				1.9
U - C_1	2.47 (1)	5.7 (5)	0.008 (1)	
U - U_1	3.49 (1)	12	0.004 (1)	
U - C_2	4.15 (3)	8	0.009 (1)	
Uranium carbide UC$_{1.00}$				1.8
U - C_{1a}	2.31 (1)	0.2 (5)	0.007 (1)	
U - C_{1b}	2.47 (1)	6.0 (5)	0.007 (1)	
U - U_1	3.50 (1)	12	0.004 (1)	
U - C_2	4.16 (2)	8	0.008 (1)	
Uranium carbide UC$_{1.04}$				2.0
U - C_{1a}	2.31 (1)	0.9 (5)	0.007 (1)	
U - C_{1b}	2.48 (1)	6.0 (5)	0.007 (1)	
U - U_1	3.51 (1)	12	0.004 (1)	
U - C_2	4.16 (3)	8	0.008 (1)	

The low R-factor values (<2%) and the good agreement between experimental and fitted spectra confirm that $UC_{1\pm x}$ compounds all have a NaCl structure.

In the case of hypostoichiometric $UC_{0.96}$, the first U-C_1 and U-U_1 distances are equal to 2.47 (1) and 3.49 (Å), respectively. Note that metallic U atoms found in XRD are not detected in the EXAFS analysis, possibly as it is a very minority phase. Regarding the $UC_{1.00}$ material, the U-C_1 and U-U_1 first interatomic distances are consistent with those already determined by an earlier EXAFS study [19] and by neutron diffraction (U-C_1 = 2.48 Å; U-U = 3.50 Å [19]). However, evidence for an additional U-C first shell distance, noted UC_{1a} in Table 6.3, has been found in the present work. This bond length at 2.31 Å, as explained above, is attributed to the presence of excess carbon atoms in interstitial positions in the NaCl structure. For the hyperstoichiometric $UC_{1.04}$, two U-C first distances are observed as well; the U-C_{1a} and U-C_{1b} distances are 2.31 (1) and 2.48 (1) Å, respectively. The slight increase of the U –C_{1b} distance is in agreement with the slight increase of the lattice parameter and can be understood from the hyperstoichiometry.

6.6.2.   *Annealing of UC$_{0.96}$*

The hypostoichiometric sample of UC$_{0.96}$ exhibits vacancies in the fcc carbon sublattice. The corresponding NMR spectrum exhibits a sharper peak at 1448 ppm with width 28.7 ppm and a broader peak centred at 1483 ppm, but 110 ppm wide. The sharp peak is attributed to C in a UC octahedral environment, the broader peak is attributed to carbons in a UC octahedral site. There appear to be fewer vacancies associated with the carbons in the sharper peak and more vacancies associated with the broader peak in a more disordered arrangement. Thus the stoichiometry of this disordered material would be lower than 0.96 and the sharper peak closer to true stoichiometry. Assuming a 1.00 stoichiometry for the sharp peak and weighting by the areas under the two peaks this stoichiometry would be 0.92. However, the shift of 1448 ppm, compared with 1461 ppm for UC$_{1.00}$, may even indicate a slightly carbon rich region associated with this peak. Previous resistivity measurements have shown that annealing quenched non-stoichiometric UC$_{1-x}$ samples leads to an ordering in the sample and has been explained by a reorganisation of the vacancies [41]. Therefore, an annealing on the UC$_{0.96}$ sample was performed to confirm the link, in NMR spectra, between line broadening and disorder in the lattice. In the XRD patterns, annealing of the sample leads to an increase of the lattice parameter (see Figure 6.1), due to stress release, which is agreement with earlier literature observations [6,34].

The NMR spectra of the annealed, and of the as cast UC$_{0.96}$, sample are presented in Figure 6.9.
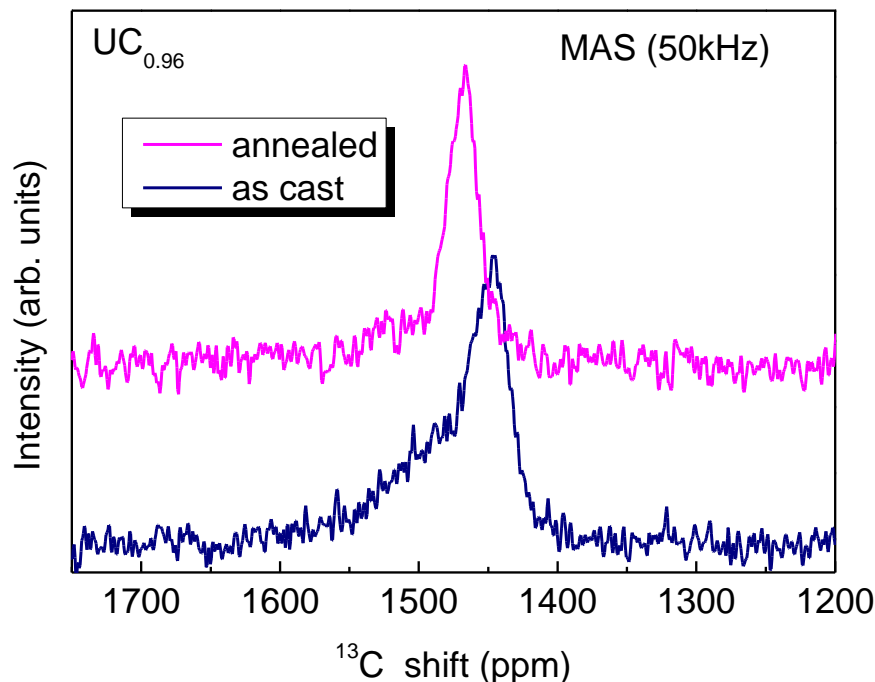
Figure 6.9: ^{13}C Hahn-echo MAS NMR spectra of $UC_{0.96}$ as cast and $UC_{0.96}$ annealed at 1450°C during 10 hours. (ν_r=55kHz, B_0=9.4 T).

After heat treatment, the majority of the sample has transformed to yield a main Lorentzian ^{13}C peak with a FWHM of 25.7 ppm at 1468 ppm. A small broad peak (FWHM=89.3 ppm) remains at 1481 ppm but it is clearly in the noise. Hence, ^{13}C NMR has indicates that the heat treatment has induced a substantial rearrangement of the carbon atoms across carbon deficient and carbon rich (possibly excess carbon) regions to produce one fairly uniform carbon environment with respect to vacancy ordering, as has been reported elsewhere [42]. The Lorentzian peak of the annealed $UC_{0.96}$ sample has a shift corresponding to the weighted average of the two peaks of the as cast sample. Matsui *et al.* [6] have shown that the resistivity of the as cast and hypostoichiometric samples ($UC_{0.98}$ and $UC_{0.96}$) is higher than for annealed samples, which they explained by the presence of stress and by the distribution of vacancies [43] in the lattice [39]. In this study, unlike XRD, the ^{13}C NMR spectra enable the observation of the transition from disordered (as cast) to ordered (annealed) sample by virtue of the broadening and position of the peaks (see Figure 6.9).

6.7.   Summary

In the present work, the local carbon environments of UC$_{1\pm x}$ samples (0.96 ≤ "1±x" ≤ 1.04) was investigated using a unique combination of techniques: XRD, MAS-NMR and EXAFS. To complement the long-range order analysis with XRD (structure, lattice parameters), both NMR and EXAFS are sensitive to short range order distance (interatomic distances, coordination numbers). XRD showed an evolution of the lattice parameter versus carbon content. EXAFS indicates the NaCl type structure was achieved for all compositions, distinctly excluding the ZnS structure. Also, EXAFS detects the presence of vacancies in the C sublattice and the full occupation of the U sublattice in the UC$_{0.96}$ sample. High resolution ^{13}C MAS NMR spectra exhibit two peaks corresponding to two types of carbon environment in the lattice for all the as cast samples independently of the composition. The preparation of pure uranium monocarbide UC$_{1.00}$ is not achievable, at least by this synthesis method. Coupling NMR and EXAFS, it was possible to show that the two environments could be attributed to a majority C atom sublattice in octahedral sites and to the excess of carbon atoms, which according to the EXAFS analysis, is preferentially in interstitial positions. The transition from disordered to ordered structure in UC$_{1\pm x}$ samples has been observed by MAS NMR. The carbon content affects the broadening of the ^{13}C peaks, showing a sharp difference between hypo- and hyperstoichiometric samples. The presence and really the heterogeneous distribution of vacancies in the as cast hypostoichiometric samples, leads to a broadening of the ^{13}C peaks. Only annealing could lift this disorder and provide a more ordered structure with the presence of a single ^{13}C peak and to a lattice parameter closer to that found for a C/U ratio of 1.00, as displayed by XRD. Coupling NMR and EXAFS to XRD is a powerful means to provide detailed unambiguous assignment of local structure. Unfortunately, the ^{235}U NMR active isotope has a low larmor frequency and large quadrupole moment making it unfavourable for high-resolution NMR, but the recent discovery of the ^{239}Pu NMR signal [44] bodes well for an even more powerful combination of these methods, whereby NMR and EXAFS can be used to probe identical nuclei.

6.8.   References

[1]   B. R. T. Frost, *J. Nucl. Mater., 10 (1963) pp. 265–300.*

[2]   A. S. Kolokol, S. L. Shimkevich, In *International Conference on Nuclear Engineering, Proceedings, ICONE; 2008; Vol. 1, pp. 759–763.*

[3]   M. K. Meyer, R. Fielding, *J. Nucl. Mater., 371 (2007) pp. 281-287*

[4]   H. Matsui, *J. Nucl. Sci. and Technol., 9 (1972) pp. 185–186.*

[5]   F. Le Guyadec, C. Rado, S. Joffre, S. Coullomb, C. Chatillon, E. Blanquet, *J. Nucl. Mater., 393(2009) pp.* 333–342.

[6]   H. Matsui, M. Horiki, T. Kirihara, *J. Nucl. Sci. and Technol., 18 (1981) pp. 922-929.*

[7]   O. Sisman, J. G. Morgan, *Irradiation Behaviour of High-Temperature Fuel Materials; 1968.*

[8]   V. V. Akhachinskii, S. N. Bashlykov, *Atom. Ener.27 (*1969) pp. 1317–1326.

[9]   H. M. Lee, L. R. Barbett, *J. Nucl. Mater., 27 (1968) pp. 275-284.*

[10]   H. Watanabe, T. Kikuchi, K. Furukawa, *J. Nucl. Mater., 43 (1972) pp. 321-329.*

[11]   I. A. Menzies, K. N. Strafford, *J. Nucl. Mater., 21 (1967) pp. 287-301.*

[12]   R. J. Gray, W. C. Thurber, C. K. H. DuBose, *Preparation of Arc- Melted Uranium Carbides, 1958.*

[13]   Tagawa, H.; Fujii, K.; Sasaki, Y. *J. Nucl. Sci. and Technol., 8 (1971) pp. 244-249.* Rodriguez, P. *Bulletin of Materials Science* 1999, *22*, 215–220.

[15]   Mukerjee, S. K.; Dehadraya, J. V.; Vaidya, V. N.; Sood, D. D. *Journal of Nuclear Materials* 1990, *172*, 37–46.

[16]   Maruya, K. *Journal of Nuclear Science and Technology* 1970, *7*, 13–18.

[17]   Catlow, C. R. A. *Journal of Nuclear Materials* 1976, *60*, 151–157.

[18]   Rundle, R. E. *Acta Crystallographica* 1948, *1*, 180–187.

[19]   Vigier; Den Auwer, C.; Fillaux, C.; Maslennikov, A.; Noël, H.; Roques, J.; Shuh, D. K.; Simoni, E.; Tyliszczak, T.; Moisy, P. *Chemistry of Materials* 2008, *20*, 3199–3204.

[20]   Ducher, R.; Dubourg, R.; Barrachin, M.; Pasturel, A. *Physical Review B* 2011, *83*, 104107.

[21]   Matsui, H.; Matzke, H. *Journal of Nuclear Materials* 1980, *88*, 317–321.

[22]   Harrison, J. W. *Journal of Nuclear Materials* 1969, *30*, 319–323.

[23]   Colby Jr., L. J. *Journal of the Less Common Metals* 1966, *10*, 425–431.

[24]   Schürenkämper, A. *Journal of Inorganic and Nuclear Chemistry* 1970, *32*, 417–429.

[25]   Farnan, I.; Cho, H.; Weber, W. J.; Scheele, R. D.; Johnson, N. R.; Kozelisky, A. E. *Review of Scientific Instruments* 2004, *75*, 5232–5236.

[26]   Slichter, C. P. *Principles of Magnetic Resonnance*; 1980th ed.; Springer-Verlag: New York.

[27]   Morcombe, C. R.; Zilm, K. W. *Journal of Magnetic Resonance* 2003, *162*, 479–486.

[28]   Massiot, D.; Fayon, F.; Capron, M.; King, I.; Le Calvé, S.; Alonso, B.; Durand, J.-O.; Bujoli, B.; Gan, Z.; Hoatson, G. *Magnetic Resonance in Chemistry* 2002, *40*, 70–76.

[29]   Rothe, J.; Butorin, S.; Dardenne, K.; Denecke, M. A.; Kienzler, B.; Löble, M.; Metz, V.; Seibert, A.; Steppert, M.; Vitova, T.; Walther, C.; Geckeis, H. *Review of Scientific Instruments* 2012, *83*.

[30]   Ravel; Newville, M. *Journal of Synchrotron Radiation* 2005, *12*, 537–541.

[31]   Rehr, J. J.; Ankudinov, A.; Zabinsky, S. I. *Catalysis Today* 1998, *39*, 263–269.

[32]   Manara, D.; De Bruycker, F.; Sengupta, A. K.; Agarwal, R.; Kamath, H. S. In *Comprehensive Nuclear Materials*; Oxford, 2012; pp. 87–137.

[33]   Storms, E. K.; Huber Jr., E. J. *Journal of Nuclear Materials* 1967, *23*, 19–24.

[34]   Williams, J.; Sambell, R. A. J.; Wilkinson, D. *Journal of the Less Common Metals* 1960, *2*, 352–356.

[35]   Potter, P. E. *Journal of Nuclear Materials* 1972, *42*, 1–22.

[36]   Levine, S. G. *J. Chem. Educ.* 2001, *78*, 133.

[37]   Freyss, M. *Physical Review B* 2010, *81*, 014101.

[38]   Lewis, W. B.; Rabideau, S. W.; Krikorian, N. H.; Witteman, W. G. *Phys. Rev.* 1968, *170*, 455–462.

[39]   Sarian, S.; Dalton, J. T. *Journal of Nuclear Materials* 1973, *48*, 351–359.

[40]   Chartier, A.; Van Brutzel, L. *Nuclear Instruments and Methods in Physics Research Section B: Beam Interactions with Materials and Atoms* 2007, *255*, 146–150.

[41]   Storms, E. K. *Analytical representation of the thermal conductivity and electrical resistivity of UC$_{1-x}$, PuC$_{1-x}$ and (U$_{1-y}$Pu$_{1-y}$)C$_{1-x}$*; 1982.

[42]   Kim, N.; Stebbins, J. F. *Chemistry of Materials* 2007, *19*, 5742–5747.

[43]   Hisayuki, M.; Ken-ichi, S.; Mitsuo, I.; Hiromi, A.; Tomoo, K. *Journal of Nuclear*

Materials 1975, *57*, 93–97.

[44]   Yasuoka, H.; Koutroulakis, G.; Chudo, H.; Richmond, S.; Veirs, D. K.; Smith, A. I.; Bauer, E. D.; Thompson, J. D.; Jarvinen, G. D.; Clark, D. L. *Science* 2012, *336*, 901–904.

Chapter 7

Structure of UC$_2$ and U$_2$C$_3$: XRD, ^{13}C NMR and EXAFS Study

ABSTRACT

In this study, uranium dicarbide (UC$_2$) has been prepared by arc melting and heat treated under vacuum to form uranium sequicarbide (U$_2$C$_3$) in the presence of a second phase UC$_{2-z}$. Both samples, as cast and heat treated, have been characterised by chemical analyses, X-ray diffraction (XRD), ^{13}C magic angle spinning nuclear magnetic resonance (MAS-NMR) and by extended X-ray absorption fine structure (EXAFS). The composition, the purity, the various environments of both U and C atoms as well as the bonds length with the coordination number have been determined. By combining a long-range order method (XRD) and short-range order spectroscopy techniques (EXAFS and NMR), a unique view on the microstructure of UC$_2$, before and after heat treatment, and of U$_2$C$_3$ phase has been achieved.

7.1. Introduction

Carbide materials are potential fuels for a number of advanced reactor designs [1] and for propulsion systems [2], as some of their properties are more favourable than oxides based fuels. Indeed, they are known for their high thermal conductivity [3], their higher structural stability and high fusion temperature [4,5,6]. Given the interest in uranium carbides for nuclear applications, a complete knowledge on the crystallographic properties of these materials is essential. Indeed, the presence of structural defects can affect the fuel properties

during irradiation and could lead eventually to a degradation of both reactor safety and fuel performance [7,8,9]. According to the U-C phase diagram [10,11] the main stoichiometries of uranium carbides are uranium monocarbide (UC$_{1\pm x}$ with x ≤ 0.05), uranium sesquicarbide (U$_2$C$_3$), and uranium dicarbide (UC$_2$). In our previous study [12] on UC$_{1\pm x}$, we investigated its structure with XRD, NMR and EXAFS techniques. It was possible to probe the order – disorder transition affected by the carbon content and the heat treatment. In this paper we extend this study to UC$_2$ and U$_2$C$_3$, the two other phases of the U-C system. Based on literature and the phase diagram the UC$_2$ phase exists in two different structures, a tetragonal form with a CaC$_2$ structure type (I4/mmm, space group (SG) n°139) [13,14] at lower temperature denoted α-UC2 and a cubic form with a NaCl structure type (Fm-3m, SG n°225) at higher temperatures, denoted the β-UC2. UC$_2$, when synthesised, is always sub-stoichiometric with a composition domain ranging from UC$_{1.75}$ to UC$_{1.95}$ [3].The lattice parameter increases with the carbon content and with heat treatment [15]. The U$_2$C$_3$ phase has the body-centred cubic Pu$_2$C$_3$–type structure (I-43d, SG n°220) [13,14] and cannot be obtained directly by arc melting [3]. Many controversies have been reported in the literature on the synthesis of U$_2$C$_3$ [16] and its magnetic properties [17]. Now it is well known that U$_2$C$_3$ can be generated from a starting material UC$_x$ (x = 1.5 to 2) by grinding, pressing, and heating under high vacuum [16]. Obtaining U$_2$C$_3$ as a single phase is difficult most likely due to the slow kinetics of the reaction. According to the starting composition, two mechanisms of reaction can take place to synthesize it, the synthetic and the decomposition reaction [18] described in equation 1 and 2 respectively:

$$UC_2 + UC \rightarrow U_2C_3 \qquad (1)$$

$$2\,UC_2 \rightarrow \quad U_2C_3 + C \qquad (2)$$

The decomposition reaction is slower than the synthetic reaction [19] and requires high vacuum to induce the departure of oxygen which in fact stabilises UC$_2$ [20]. Nickel *et al.* [19] argued that pure UC$_2$ sample does not lead directly to sesquicarbide (equation 2) but it decomposes first following the reaction: UC$_2$→UC + C. If this is correct, then the intermediate UC should appear and should be detected by XRD and/or NMR, provided it is not consumed quickly.

Thus, in this study we investigate the decomposition reaction starting with a C/U composition close to the UC$_2$ compound. While static ^{13}C NMR studies have been reported on UC$_2$ and U$_2$C$_3$ in the past [21,22], so far no MAS-NMR and no EXAFS studies have been performed on any of these phases.

Chemical analyses inform us about the carbon content; XRD about the nature of the present phases, EXAFS will inform us about the bond distances in U$_2$C$_3$, in UC$_2$ as cast and heat treated, whereas NMR provides information on the different C environments.

In the present work, we will first focus on the local structure of UC$_2$ as cast and then on UC$_2$ pressed and heat treated under high vacuum inducing the formation of U$_2$C$_3$ through an investigation coupling XRD, EXAFS and ^{13}C MAS-NMR.

7.2.   Experimental

7.2.1.   Synthesis

The sample of uranium dicarbide UC$_2$ was prepared by arc melting of uranium metal and graphite under a high purity argon atmosphere (6N) on a water-cooled copper hearth. Zirconium was placed in the preparation chamber and served as a getter for oxygen and nitrogen. The uranium dicarbide ingot was melted and turned around several times to achieve a homogenous sample. Synthesis of uranium sesquicarbide U$_2$C$_3$ is achieved by the heat treatment of the UC$_2$ sample. The latter was ball milled, pelletized and heat treated at 1450ºC for 48 hours under high vacuum (10^{-5} mbar) followed by a slow cooling at 20 °C . h^{-1}. In this article, the term "U$_2$C$_3$" is used to describe the sample obtained after heat treatment of UC$_2$ pellet and corresponds to a mixture of U$_2$C$_3$ and UC$_{2-z}$ phases. As carbides are easily oxidised in presence of humidity [23, 24], the as-synthesized samples were stored under helium (6N) to minimise oxygen contamination before performing the measurements.

7.2.2.   *Sample characterization methods*

7.2.2.1.   *Chemical analysis*

Chemical analyses of carbon contents have been performed on powdered samples by direct combustion using the infrared absorption detection technique with an ELTRA CS-800 instrument.

7.2.2.2.   *X-Ray Diffraction*

X-Ray diffraction analysis was performed on a Bruker D8 Bragg-Brentano advanced diffractometer (Cu K$_{\alpha1}$ radiation) equipped with a Lynxeye linear position sensitive detector and installed inside a glove box under inert atmosphere. The powder diffraction patterns were recorded at room temperature using a step size of 0.01973° with an exposure of 4s across the angular range $20° \leq 2\theta \leq 120°$. The operating conditions were 40 kV and 40 mA. Lattice parameters and quantification of the "U$_2$C$_3$" sample was performed by Rietveld refinement using Topas 4.1. software [25].

7.2.2.3.   *Nuclear Magnetic Resonnance (NMR)*

Uranium carbide ingots were crushed to a fine powder and loaded into 1.3 mm zirconia rotors under helium (6N) in a glove box. The particle size was sufficiently small not to affect the radiofrequency response of the sample due to skin-depth effects. The ^{13}C NMR spectra, with ^{13}C in natural abundance (1.1%), were recorded on a Bruker Advance 400 spectrometer operating at 9.4 T (Larmor frequency of ^{13}C 100 MHz). This apparatus has been adapted for the study of highly radioactive material using commercial NMR probes and rotors [26]. Despite the potential for eddy current effects during spinning of the semi-metallic uranium carbides, most of the ^{13}C MAS-NMR spectra were acquired at spinning rates of 55 kHz. A rotor-synchronised Hahn echo was used to acquire the spectra. In order to minimise baseline distortions the pulse durations were 2.5 μs ($\pi/2$) and 5 μs (π), respectively, with an echo delay of 18.2 μs (1 rotor period). Fully relaxed spectra could be acquired with a recycle delay of 150 ms due to the efficient paramagnetic relaxation mechanism provided by the

conduction electrons [27]. ^{13}C chemical shifts were calibrated relative to tetramethylsylane (0 ppm) by using adamantane as a secondary reference, with ^{13}CH and ^{13}CH$_2$ peaks at 29.45 ppm and 38.48 ppm [28], respectively. Due to safety restrictions on running the MAS-NMR system unattended overnight, the number of transients was limited to 51,200 for each spectrum. All the spectra were fitted using the dmfit software [29].

7.2.2.4.   Extended X-Ray Absorption Fine Structure

EXAFS measurements were performed on the uranium carbides powder co-milled with BN at the INE-Beamline at the Angströmquelle Karlsruhe (ANKA) [30]. A Ge(422) double crystal monochromator coupled with a collimating and focusing Rh-coated mirrors was used. X-ray absorption fine structure (XAFS) spectra were collected in transmission geometry at the U L$_{III}$ (17166 eV) edge. Energy calibration was provided by an yttrium (17038 eV) foil located between the second and the third ionization chamber. Each spectrum was aligned using the U reference foil XANES spectra before averaging scans. The ATHENA software [31] was used for data reduction, normalisation and extraction of EXAFS oscillations. Experimental EXAFS spectra were Fourier-transformed using a Hanning window within 2.5 – 8.8 Å^{-1} k-range. The ARTEMIS software [31] was used to perform the fits. Both scattering phases and amplitudes were calculated using the *ab initio* code FEFF8.20 [32]. Data fitting was performed in R space for R values ranging from 1.4 to 5.1 Å. The S_0^2 value was set at 0.9 and the shift in threshold energy was varied as a global parameter.

7.3.   Results and discussion

7.3.1.   Chemical and X-Ray Diffraction Analyses of UC$_2$ as cast and "U$_2$C$_3$" samples

The chemical analysis results, summarized in Table 7.1, indicate that the as cast UC$_2$ sample has a carbon content of 8.70 ± 0.26 wt% corresponding to a stoichiometry of UC$_{1.89 \pm 0.06}$.

Table 1.1: Chemical analyses of UC_2 as cast and "U_2C_3" samples

	UC_2	"U_2C_3"
Calculated C content (wt%)	8.91	-
C/U ratio	1.94	-
Measured C content (wt%)	8.70 (0.26)	8.20 (0.16)
Measured O content (ppm)	114(23)	6800(1360)
C/U ratio	1.89 (0.06)	1.77 (0.04)

Within uncertainty of the measurement this stoichiometry lies within the calculated value derived from the starting material, i.e. $UC_{1.94}$. This slight hypostoichiometry was expected however, as the composition domain of UC_2 ranges from $UC_{1.75}$ to $UC_{1.95}$ [3]. In the present manuscript, the nomenclature of the hypostoichiometric and as cast sample $UC_{1.94}$ will be simply UC_2. Also the analyses show that after heat treatment of pressed UC_2, the carbon content in "U_2C_3" sample decreased. This carbon can leave the matrix as CO through the application of the temperature and the high vacuum [33,34].

All peaks in the XRD pattern of the UC_2 sample, presented in Figure 7.1 (inset), could be assigned to a tetragonal structure and a space group of I4/mmm.
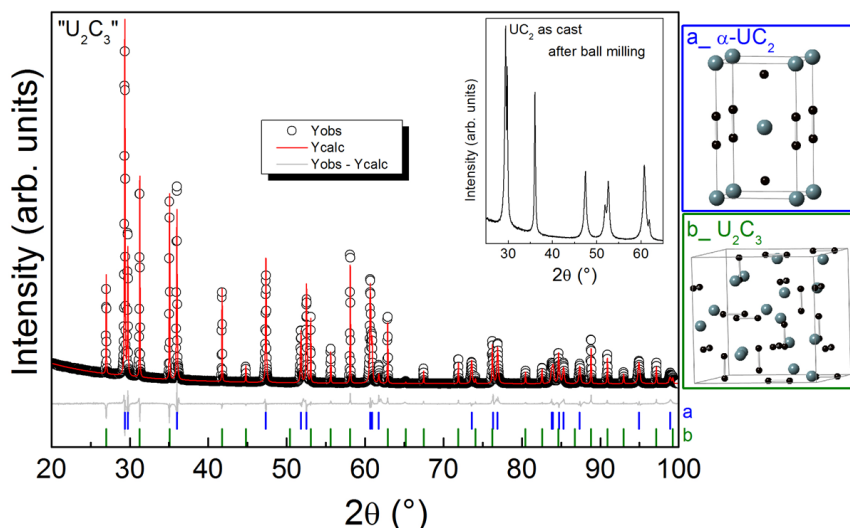

Figure 7.1 : Rietveld refinement of "U_2C_3" x-ray diffraction pattern (blue stick corresponding to UC_2 phase and green stick corresponding to U_2C_3 phase with their corresponding crystalline structure) _ insert : XRD pattern of UC_2 as cast

It shows that uranium dicarbide can be obtained directly as a single phase in this composition domain by arc melting. The broadening of the peaks, related to the crystallite size and the strain [35] present in the material, is linked out to the preparation using ball milling [36]. The high purity of the sample is also supported by the low oxygen content (<200 ppm). The associated lattice parameters were a = 3.5225 (1) Å and c = 5.994 (1) Å, which are in good agreement with literature data [37,38]. After ball milling and pressing of the as cast UC$_2$ sample, the heat treatment at 1450 °C – 48 h under high vacuum leads to the formation of a mixed phase sample, whose X-ray diffraction pattern is presented in Figure 4.1. All the peaks have been assigned to two phases, U$_2$C$_3$ with body-centred cubic Pu$_2$C$_3$ type *(I-43d)* and UC$_{2-z}$ with tetragonal structure, with an approximate composition of about 30 and 70wt% respectively, as determined by Rietveld refinement. This composition is also supported by the phase rule, considering the phase diagram [11] and the C/U ratio of the sample (UC$_{1.77 \pm 0.04}$) determined by chemical analyses. The lattice parameter of U$_2$C$_3$, a = 8.0889(3) Å, is in good agreement with literature data [30]. The lattice parameters of UC$_{2-z}$ after annealing increase to a = 3.5252(3) Å and c = 6.000 (2) Å.

7.4.   Local Structure

7.4.1.   Study of UC$_2$ as cast sample

The fitted U-L$_{III}$ edge EXAFS spectra in k- range and R space are presented in Figure 7.2. The calculated UC$_2$ crystallographic parameters are given in Table 7.2.
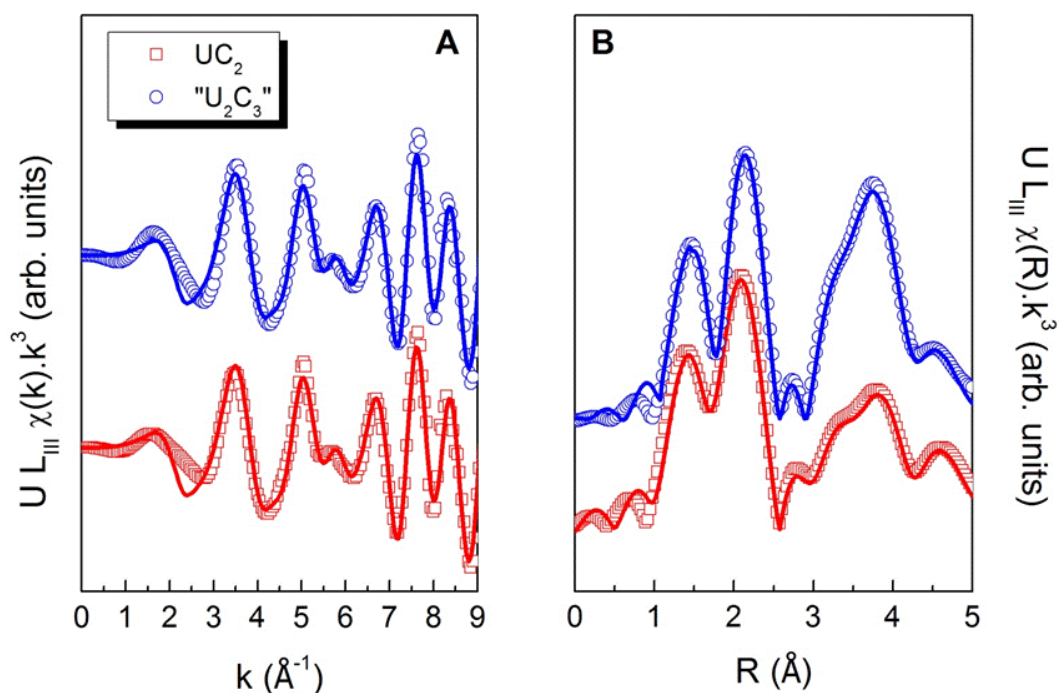
Figure 7.2: Experimental U-L$_{III}$ EXAFS spectra and their corresponding Fourier transforms of UC$_2$ as cast and "U$_2$C$_3$" samples.

Table 7.2: Crystallographic parameters derived from EXAFS analyses of UC$_2$ as cast sample(R: interatomic distance; N: number of neighbours; σ: Debye-Waller factor, (a) this work, (b) Calculated data [39]).

Shell	R (Å)		N	σ (Å^2)	R factor (%)
	(a)	(b)	(a)	(a)	
U - C$_{1a}$	2.30 (1)	2.32	2	0.0073 (3)	2.1
U - C$_{1b}$	2.58 (1)	2.59	8	0.0071 (6)	
U – U$_1$	3.53 (1)	3.54	4	0.0040 (4)	
U – C$_2$	3.71 (3)	3.88	2	0.008 (1)	
U – U$_2$	3.87 (3)	3.90	8	0.006 (2)	

Taking into account the results of the XRD analysis, the EXAFS experimental data were fitted using a FEFF model consisting of spherical clusters of atoms with 7.5 Å size and CaC$_2$ type structure *(I4/mmm)*. The following single scattering paths were taken into account: 2 U-C, 1 U-U and 1 U-C, 1 U-U corresponding to the first and second U coordination spheres, respectively. Both triangular and quadruple multiple scattering paths were included in the fit. The EXAFS analyses indicate that U is surrounded by C atoms at 2.30 (1), 2.58 (1) and 3.71 (3) Å and by U atoms at 3.53 (1) and 3.87 (1) Å. The U-U$_1$ distance, corresponding to the lattice parameter a, is in good agreement with the value derived from XRD. From these

derived interatomic distances, one can calculate that the C-C distance of the C$_2$ dumbbells is equal to 1.39 (1) Å, which is slightly higher than the previous reported value of 1.37 (1) Å [39].

In Figure 7.3, the ^{13}C Hahn-echo MAS NMR spectrum of UC$_2$ acquired at a spinning frequency of 55 kHz is presented.
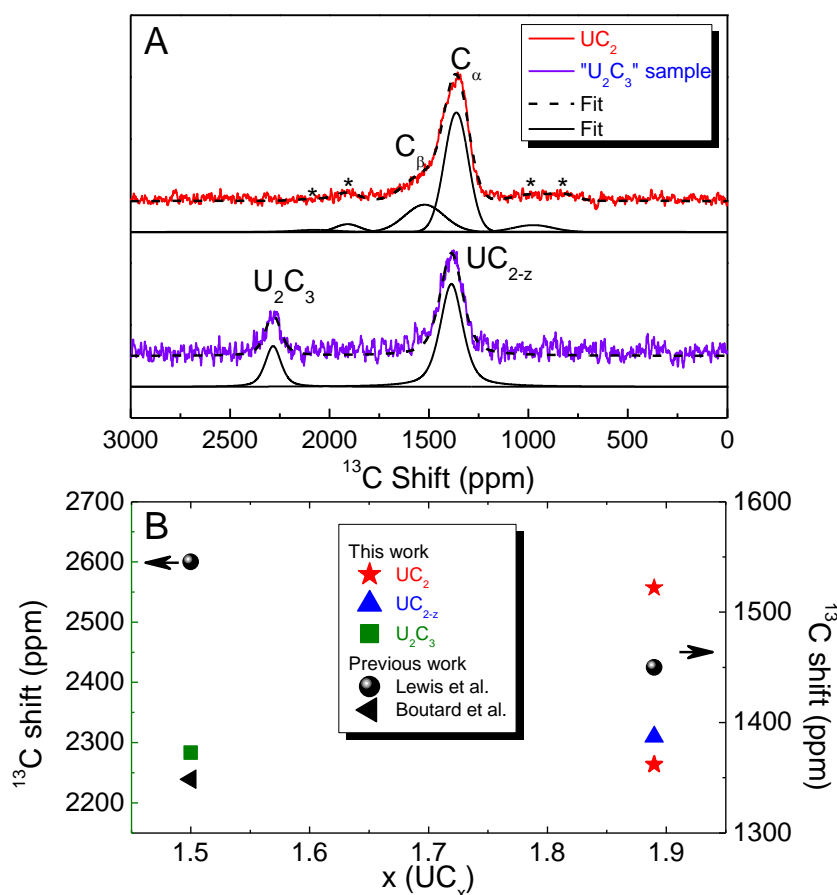
Figure 7.3: A. ^{13}C Hahn-echo MAS-NMR spectra of UC$_2$ and "U$_2$C$_3$" samples obtained at a spinning frequency of 55 kHz (B$_0$ = 9.4 T). The "U$_2$C$_3$" sample contains U$_2$C$_3$ and UC$_{2-z}$ phases. The stars correspond to the spinning sidebands. B. Comparison with literature of ^{13}C shifts in UC$_2$ and U$_2$C$_3$.

As the uranium carbides are semi-metals, large NMR shifts (Knight shifts) are expected due to the collective hyperfine shifts of unpaired electrons near the Fermi surface [40]. The spectrum has been fitted with two Gaussians at 1522 (70) ppm (C$_\beta$) and 1362 (10) ppm (C$_\alpha$) with full width at half maxima (FWHM) of 215 (4) and 142 (1) ppm, respectively (see Table 7.3).

Table 7.3: ^{13}C isotropic chemical shift (δ_{iso}), content of each ^{13}C species and Full Width at Half Maximum (FWHM) for the as cast UC$_2$ and "U$_2$C$_3$" samples acquired at a spinning frequency of 55 kHz. (For UC$_2$: C$_\alpha$: δ_{iso} of the main peak and C$_\beta$: δ_{iso} of the second peak).

Sample	δ_{iso} (ppm)		Content (mol%)		FWHM (ppm)	
	^{13}C$_\beta$	^{13}C$_\alpha$	^{13}C$_\beta$	^{13}C$_\alpha$	^{13}C$_\beta$	^{13}C$_\alpha$
UC$_2$	1522 (70)	1362 (10)	30	70	215 (4)	142 (1)
"U$_2$C$_3$"	^{13}C$_{U2C3}$	^{13}C$_{UC2\text{-}z}$	^{13}C$_{U2C3}$	^{13}C$_{UC2\text{-}z}$	^{13}C$_{U2C3}$	^{13}C$_{UC2\text{-}z}$
	2283 (50)	1387 (10)	25	75	106 (2)	148 (1)

Additional spinning sidebands have been identified and are indicated by stars. The second carbon environment, C$_\beta$, was detected with an intensity corresponding to 30 % of the total spectrum area. C$_\alpha$ could be attributed to carbons localized on the octahedral sites of the CaC$_2$ structure while C$_\beta$ to carbons in a more disordered environment (i.e. due to the presence of more vacancies or interstitials due to the rapid cooling). The value of the ^{13}C shifts found here are relatively similar to that found by Lewis *et al.* [22] (Figure 7.3B), who, only identified one peak, probably due to the lower signal to noise ratio.

To induce improved local ordering of the carbons as previously seen for UC$_{0.96}$ [12], an annealing of an ingot piece of UC$_2$ was made for 10 hours at 1450°C. The ordering of the structure in UC$_2$ (release of strain, vacancies ordering) should have led to a decrease of the C$_\beta$ peak intensity and width. Unfortunately, however, the annealed sample would not spin for further MAS-NMR analysis. This could have been due to an increased metallic property inducing a higher Eddy current and preventing the rotation of the sample in high field, as one might expect, as it has been shown that the resistivity of UC$_2$ decreases after annealing [41]. A static experiment (Figure 7.4) performed on the same sample shows a narrowing and a better resolution of the peaks C$_\alpha$ and C$_\beta$ in the annealed sample in agreement with an ordering of the structure.
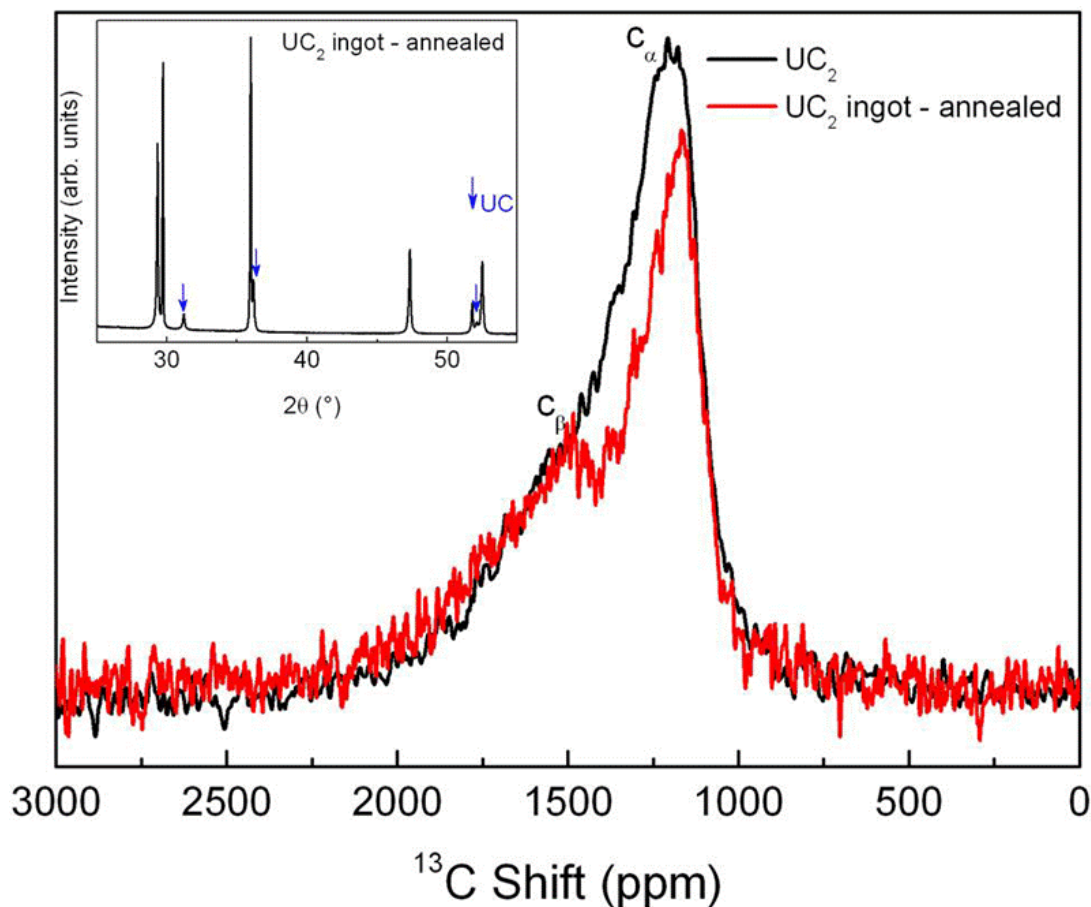
Figure 7.4: ^{13}C hahn-echo static spectra of UC$_2$ as cast and of an ingot piece of UC$_2$ annealed at 1450°C for 10h at 10^{-5} mbar (B$_0$=9.1T).

Also the heat treatment made on an ingot of UC$_2$ lead to lattice parameters of a = 3.5280(1) Å, c = 6.008 (6) Å and the precipitation of UC (as shown in the XRD data in the inset in Figure 7.4), showing that the process of grinding and pressing is indeed necessary to form U$_2$C$_3$ [42]. In our previous study [12], the static spectrum of UC displayed a ^{13}C shift of 1464 ppm. It overlaps with the C$_\beta$ peak of UC$_2$, and thus we cannot distinguish the two phases (UC and C$_\beta$ of UC$_2$) by this technique. The precipitation of UC in annealed ingot of UC$_2$ sample has been reported in literature [19, 43] and no explanation concerning the absence of U$_2$C$_3$ formation through synthetic reaction was provided so far.

7.4.2. Study of "U$_2$C$_3$" sample

113

The U-L$_{III}$ edge spectra of the "U$_2$C$_3$" sample in k and R space are plotted in Figure 7.2. The FT spectra of "U$_2$C$_3$" and UC$_2$ (Figure 7.2B) differ in the 3 - 5 Å R range due to variations of the number of U atoms in the second shell. The crystallographic parameters of U$_2$C$_3$ and UC$_{2-z}$ are summarized in Table 7.4 and Table 7.5, respectively.

Table 7.4: Crystallographic parameters derived from EXAFS analyses of U$_2$C$_3$ phase present in the "U$_2$C$_3$" sample (R: interatomic distance; N: number of neighbours; σ: Debye-Waller factor, (a) this work, (b) Calculated data [39]).

Shell	R (Å)		N	σ (Å^2)	R factor (%)
	(a)	(b)	(a)	(a)	
U - C$_{1a}$	2.45 (2)	2.50	3	0.0075 (4)	2.5
U - C$_{1b}$	2.57 (2)	2.56	3	0.0078 (5)	
U – C$_{1c}$	2.77 (2)	2.82	3	0.0076 (3)	
U – U$_{1a}$	3.35 (3)	3.34	3	0.005 (1)	
U – U$_{1b}$	3.53 (3)	3.48	2	0.004 (2)	
U – U$_{1c}$	3.70 (5)	3.68	6	0.005 (2)	

Table 7.5: Crystallographic parameters derived from EXAFS analyses of UC$_{2-z}$ phase present in the "U$_2$C$_3$" sample (R: interatomic distance; N: number of neighbours; σ: Debye-Waller factor, (a) this work, (b) Calculated data [39]).

Shell	R (Å)		N	σ (Å^2)	R factor (%)
	(a)	(b)	(a)	(a)	2.3
U - C$_{1a}$	2.31 (2)	2.32	2	0.008 (1)	
U - C$_{1b}$	2.58 (2)	2.59	8	0.008 (1)	
U – U$_1$	3.54 (2)	3.54	4	0.005 (1)	
U – C$_2$	3.72 (3)	3.88	2	0.009 (1)	
U – U$_2$	3.89 (3)	3.90	8	0.007 (2)	

Both U$_2$C$_3$ and UC$_{2-z}$ crystal phases were taken into account in the structural model used in the EXAFS analyses. Spherical clusters of 7.5 Å in size with a Pu$_2$C$_3$-type structure (I-43d, U$_2$C$_3$) and CaC$_2$ type structure (I4/mmm, UC$_2$) were employed in the FEFF calculations.

The experimental data and fit agree within 2.5 %, which confirms the validity of the used models. The interatomic distances derived from EXAFS are well in accordance with first principle calculation made by Shi *et al.* [39] on U$_2$C$_3$. Indeed, the first U-C interatomic distances are equal to 2.45 (2), 2.57 (2) and 2.77 (2) Å. The U-U interatomic distances are equal to 3.35 (3), 3.53 (3) and 3.70 (5) Å respectively (see Table 7.4 and Table 7.5).

Regarding the UC$_{2-z}$ phase, the interatomic distances seem slightly larger than those observed in the as cast UC$_2$ sample. Although the experimental error is significant, these EXAFS results are consistent with the increase of the lattice parameter observed by XRD.

Figure 7.3A (bottom) presents the ^{13}C Hahn-echo MAS-NMR spectrum of "U$_2$C$_3$" acquired at spinning frequency of 55 kHz. Two peaks are identified, one at 1387 (10) ppm and another at 2283 (50) ppm. The first peak is attributed to UC$_{2-z}$ based on the previous NMR spectrum (Figure 7.3A (top)) and on XRD data. It should be noticed that the peak is slightly shifted (~30 ppm) compared to that of the as cast UC$_2$ sample. This difference should be due to a different carbon environment characterised by a different lattice parameter. The second peak can be attributed to U$_2$C$_3$ phase. Its shift is lower than that obtained in the static experiment by Lewis *et al.* [22], but very close to that obtained by Boutard and De Novion [21] (Figure 7.3B). The quantification of the two phases as obtained by NMR (UC$_{2-z}$/U$_2$C$_3$: 75 mol%/25 mol%) confirms that derived from XRD analysis (UC$_{2-z}$/U$_2$C$_3$: 70 wt%/30 wt%). If free carbon is present in the sample, it is below the detection limits of both NMR and XRD. The "U$_2$C$_3$" sample has a carbon content of 8.20 ± 16 wt%, and it has been reported [18] that free carbon appears in samples containing more than 8.6 wt% of C.

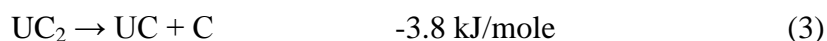### 7.4.3. *Synthesis mechanism of U$_2$C$_3$ from UC$_2$*

Taking into account the quantification of the two phases obtained by XRD (UC$_{2-z}$/U$_2$C$_3$: 70 wt%/30 wt%), the carbon content in "U$_2$C$_3$" sample determined by chemical analyses (Table 1) and considering the atomic mass of carbon is negligible relative to uranium so that in terms of molar mass $M_{UC2-z} \sim \frac{1}{2} M_{U2C3} \sim M_{UC1.77}$, then one finds that the C/U ratio of UC$_{2-z}$ is about 1.89. This value is, within the experimental error of the chemical analysis, identical to the starting UC$_2$ as cast sample. Thus under our experimental conditions, we can represent the reaction of the crushed and pelletized sample under heat treatment (Δ) at 1450 °C, during 48 h and 10^{-5} mbar nominally as,

$$UC_2 \ (UC_{1.89}) \xrightarrow{\triangle} 0.12 \ \overset{\nearrow}{C} + \text{"U}_2\text{C}_3\text{"} \ (UC_{1.77}) = UC_{2-z} \ (UC_{1.89}) + U_2C_3$$

115
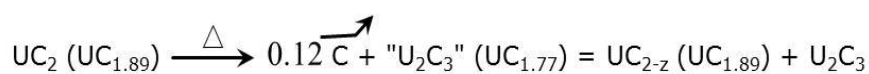
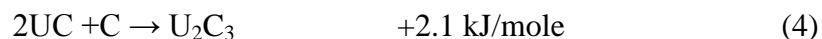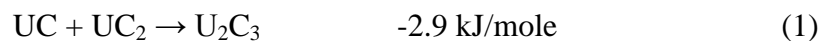We can also exclude that the ratio C/U in UC$_{2-z}$ is superior to the ratio present in the starting material UC$_2$. Indeed, as argued by Imoto et al. [18], this should only take place when UC precipitates after heat treatment of UC$_2$, just as we observed when heating an ingot of UC$_2$ (Figure 7.4).

The carbon content decrease is related to the decarburisation of UC$_2$ which can take place along reactions 2 and 3, having the change in Gibbs free energy as reported in reference [44]:

$$\Delta G_f^{\circ}(1300 \text{ K}) \text{ [44]}$$

$$2 \text{ UC}_2 \rightarrow \text{U}_2\text{C}_3 + \text{C} \qquad -7.9 \text{ kJ/mole} \qquad (2)$$

$$\text{UC}_2 \rightarrow \text{UC} + \text{C} \qquad -3.8 \text{ kJ/mole} \qquad (3)$$
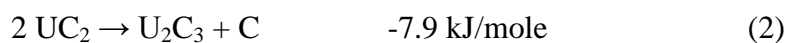
When reaction 3 occurs, UC could react along two reaction paths, 1 and 4, to form U$_2$C$_3$:

$$\text{UC} + \text{UC}_2 \rightarrow \text{U}_2\text{C}_3 \qquad -2.9 \text{ kJ/mole} \qquad (1)$$

$$2\text{UC} + \text{C} \rightarrow \text{U}_2\text{C}_3 \qquad +2.1 \text{ kJ/mole} \qquad (4)$$

Reaction 4 is from a thermodynamic perspective not favourable and thus if UC is present then it contributes only to the formation of U$_2$C$_3$ via the synthetic reaction (1). Within the detection limit of XRD, we did not observe a UC phase as an intermediate on heating a pellet formed from a crushed sample and this may exclude the process of synthetic reaction as a requirement for the decomposition reaction, as has been proposed by Nickel et al. [19]. The detection limit of XRD and NMR, however, does not exclude the later assumption completely. Nevertheless, the precipitation of UC in a matrix of UC$_2$, when heating an as cast ingot directly, does not lead to the formation of U$_2$C$_3$ (Figure 7.4). The grinding and the pressing of UC$_2$ before heat treatment are essential to synthesize U$_2$C$_3$.

Apart from the slow rate of the decomposition reaction, the U$_2$C$_3$ yield may be limited due to either insufficient oxygen in the sample to remove C as CO and possibly drive the reaction. It could also be speculated that the absence of excess carbon in the starting material to precipitate the C in the sample could hinder the reaction. Monitoring the reaction as a

116

function of time would be necessary, together with an analysis of the gas formed during the reaction, to elucidate this matter.

It is interesting to note, however, that the heat treatment on the UC_2 pellet (Figure 7.1), leads to a highly crystallised "U_2C_3" sample as displayed by very narrow diffraction peaks. The thermal energy obviously permits C diffusion and the growth of U_2C_3 crystallites during the process [42,45,46].

7.5.   Conclusion

A structural investigation of UC_2 (= $UC_{1.89 \pm 0.05}$) and U_2C_3 phases has been performed using a unique combination of different techniques (XRD, NMR and EXAFS). EXAFS determination of the first U-C and U-U bond distances is in agreement with the tetragonal CaC_2 structure. ^{13}C MAS NMR of the UC_2 sample identified a major carbon contribution at 1362 ppm, and a small contribution to the signal at 1522 ppm, which we attribute to a well ordered and less ordered phases, respectively. Heat treatment of such as cast ingots results in its partial decomposition to UC. In contrast heat treatment of a pulverised ingot, repressed into a pellet yields a U_2C_3 phase coexisting with a second phase of UC_{2-z}, with the latter having a slightly different lattice parameter than the as cast sample. EXAFS studies could distinguish between the CaC_2 and Pu_2C_3 type phase's present, while ^{13}C NMR identified the shift of the U_2C_3 at 2283 ppm. The mechanisms of the reaction leading to U_2C_3 are not clear, but the results of this study suggest that a simple decomposition mechanism is most likely.

7.6.   References

[1] M. K. Meyer, R. Fielding, J. Gan, J. Nucl. Mater. 371 (2007) 281–287.

[2] D.R. Koenig, LANL LA-10062-H, (1986).

[3] B.R.T. Frost, J. Nucl. Mater. 10 (1963) 265–300.

[4] H. Matsui, J. Nucl. Sci. Technol. 9 (1972) 185–186.

[5] A. S. Kolokol, A. L. Shimkevich, Inter. Conf. Nucl. Engin., Proceedings, ICONE; 1(2008) 759–763.

[6] P. Rodriguez, Bull. Mater. Sci. 22 (1999) 215–220.

[7] F.J. Homan, T. B. Lindemer, E. L. Long, T. N. Tiegs, R. L. Beatty, Nucl. Techn. 35(1977) 428-441.

[8] K. Minato, T. Ogawa, K. Sawa, A. Ishikawa, T. Tomita, S. Iida, and H. Sekino, Nucl. Technol. 130 (2000) 272-281.

[9] E. K. Storms, Jr. E. J. Huber, J. Nucl. Mater. 23 (1967) 19–24.

[10] P.-Y. Chevalier, E. Fischer, J. Nucl. Mater. 288 (2001) 100–129.

[11] D. Manara, F. De Bruycker, A. K. Sengupta, R. Agarwal, H. S. Kamath, Comprehensive Nuclear Materials, Edited by R. Konings. Elsevier, Amsterdam, Holland, 2012, pp. 87–137.

[12] U. Carvajal-Nunez, L. Martel, D. Prieur, E. Lopez Honorato, R. Eloirdi, I. Farnan, T. Vitova, J. Somers, Inorg. Chem. 52 (2013) 11669-11676.

[13] C. De Novion, J.-P. Krebs, P. Meriel, C. R. Acad. Sc. Paris, ser. B 263 (1966) 457-459

[14] A. E. Austin, Acta Cryst. 12 (1959) 159–161.

[15] H. Tagawa, K. Fujii, Y. Sasaki, J. Nucl. Sci. Technol. 8 (1971) 244-249.

[16] A. Buschinelli, A. Naoumidis, H. Nickel, J. Nucl. Mater. 58 (1975) 67–77.

[17] R. Eloirdi, A.J. Fuchs, J.-C. Griveau, E. Colineau, A. B. Shick, D. Manara, R. Caciuffo, Phys. Rev. B 87 (2013) 214414_1-214414_9.

[18] S. Imoto*, T.* Sano*, Y.* Takada**,** K. Yamamoto, K. Watanabe, T. Isoda, and H. Uchikoshi, in L. E. Russell et al., Eds., Carbides in Nuclear Energy, Maunillan, London, 1 (1964) 7-21.

[19] H. Nickel, H. Saeger, J. Nucl. Mater. 28 (1968) 93-104.

[20] J. Henney, D.T. Livey, N.A. Hill, Trans. Brit. Ceram. Soc. 62 (1963) 955.

[21] J.-L. Boutard, C.-H. De Novion, Solid State Comm. 14 (1974) 181–185.

[22] W. B. Lewis, S. W. Rabideau, N. H. Krikorian, W. G. Witteman, Phys. Rev. 170 (1968) 455–462.

[23] L. J. Colby Jr., J. Less Common Metals 10 (1966) 425–431.

[24] A. Schürenkämper, J. Inorg. Nucl. Chem. 32 (1970) 417–429.

[25] A. Coelho, TOPAS-Academic, V. 4.1, Coelho Software, Brisbane (2007).

[26] L. Martel, J. Somers, C. Berkmann, F. Koepp, A. Rothermel, O. Pauvert, C. Selfslag, I.Farnan, Rev. Sci. Instrum. 84 (2013) 55112–55112-5.

[27] C. P. Slichter, Principles of Magnetic Resonnance; 1980th ed.; Springer-Verlag: New York.

[28] C. R. Morcombe, K. W. Zilm, J. Magn. Reson. 162 (2003) 479–486.

[29] D. Massiot, F. Fayon, M. Capron, I. King, S. Le Calvé, B. Alonso, J.-O. Durand, B. Bujoli, Z. Gan, G. Hoatson, Magn. Reson. Chem. 40 (2002) 70–76.

[30] J. Rothe, S. Butorin, K. Dardenne, M. A. Denecke, B. Kienzler, M. Löble, V. Metz, A. Seibert, M. Steppert, T. Vitova, C. Walther, H. Geckeis, Rev. Sci. Instrum. 83 (2012) 43105-43117.

[31] B. Ravel; M. Newville, J. Synchrotron Radiat. 12 (2005) 537–541.

[32] J. J. Rehr, A. Ankudinov, S. I. Zabinsky, Catal. Today 39 (1998) 263–269.

[33] K. Maruya, S. Takahashi, J. Nucl. Sci. Technol. 5 (1968) 605-609.

[34] V.K. Orlov, V.S. Sergeev, M.A. Fomishkin, A.A. Rostovtsev, A.K. Kruglov, Atomic Energy 95 (2003) 536-539.

[35] M.A. Meyers, A. Mishra, D.J. Benson, Prog. Mater. Sci. 51 (2006) 427.

[36] J.S. Benjamin, T.E. Volin, Metall. Trans. 5 (1974) 1929-1931.

[37] V.V. Akhachinskii, S.N. Bashlykov, Atomic Energy 27 (1969) 524-532.

[38] J. Henney, D.T. Livey, N.A. Hill, Trans. Brit. Ceram. Soc. 62 (1963) 955-973.

[39] H. Shi, P. Zhang, S.-S. Li, B. Wang, B. Sun, J. Nucl. Mater. 396 (2010) 218–222.

[40] S. G. Levine, J. Chem. Educ. 78 (2001) 133.

[41] M. Horiki, S. Miyama, H. Matsui, T. Kirihara, J. Nucl. Sci. Techn. 19 (1982) 83-86.

[42] J. Laugier, P.L. Blum, J. Nucl. Mater. 39 (1971) 245–252.

[43] T. Kurasawa, H. Watanabe, T. Kikuchi, J. Nucl. Mater. 43 (1972) 192–204.

[44] M.C. Krupka, Ceram. Bull. 48 (1969) 1133-1136.

[45] L. M. Litz, A. B. Garrett, F. C. Croxton, J. Am. Chem. Soc. 70 (1948) 1718–1722.

[46] A. E. Austin, A. F. Gerds, The Uranium-nitrogen-carbon System; Battelle Memorial Institute, (1958).

Chapter 8

Summary, Conclusions and outlook

The results from the experimental research obtained in this thesis demonstrated the feasibility of the synthesis of nitride and carbide fuels bearing Am.

This is an important achievement as neither compound had been made before, It was only possible by coupling sol gel methods to prepare $(U,Pu)O_2$ porous beads, americium nitrate solution infiltration therein, and carbothermal reduction steps. Therefore, the set of results presented in this thesis, constitute an important contribution to the existing experimental knowledge on the synthesis and the characterization of uranium-plutonium-carbide and nitride fuels. New structural and thermodynamical properties data on these advanced fuels have also been determined.

8.1.   Nitride materials

The successful synthesis of the fuel samples was of paramount importance for their characterisation, though a minority oxide phase was present in the (U,Pu)N. XRD, XANES and EXAFS investigations have shown that the synthesis process leads to solid solutions, To complete the structural studies on the nitrides, a Raman spectroscopy study analysis was performed, for the first time, on UN and (U,Pu)N. It revealed the presence of Raman active modes similar to other mono-nitrides. Furthermore, local micro-Raman analysis also provided evidence for the irregular presence of carbon and oxygen impurities (artefacts of the synthesis and oxidation) on the sample surface.

Considering the importance of the high temperature behaviour for in-pile operation, the melting and freezing temperatures of both UN and (U,Pu)N have been studied. For the first time, a fast laser heating and multi-wavelength pyrometry method using a self-crucible approach was deployed. The transition temperatures obtained by this unquestionably accurate technique are in agreement with those previously proposed on the basis of more traditional measurements. According to the results, the melting point temperatures of UN and $U_{0.75}Pu_{0.25}N$ are 3120 ± 30 and 3045 ± 25 K, respectively. Pre- and post-melting XRD analysis performed on the laser irradiated samples shows that new phases are present in the UN samples after fast cooling from the liquid state but they are not observed for (U,Pu)N. This could imply that the UN melts incongruently while (U,Pu)N with this specific composition melts congruently.

(U,Pu,Am)N samples were synthesised for the first time by coupling external gelation, infiltration and carbothermal reduction methods. The resulting material was characterized by XRD. Although further improvements remain to be made, these first results look very promising to ensure the synthesis of these potential transmutation fuels.

In addition, a study on the self-irradiation damage after 25 years of storage in $U_{0.80}Pu_{0.20}N$ from the NIMPHE programme has been conducted also. Combined XRD and EXAFS measurements has shown that the self-irradiation leads to a slight increase of the interatomic distances and ultimately to an expansion of 0.3 % of the lattice parameter. The TEM analyses indicate that the nitride material exhibits a good radiation tolerance, in comparison to oxides of equivalent composition. The formation of nanometric He bubbles was observed as is the case for equivalent self-damaged oxides, but few (in comparison to oxides) extended defects were observed.

8.2. Carbide materials

Similar to the nitrides, the synthesis of (U, Pu)C and (U, Pu,Am)C was undertaken in the frame of this thesis, again by coupling external gelation, infiltration and carbothermal reduction methods. The results indicated that in all cases a multiphase material was formed, including a significant fraction of oxide impurities. Carbides of different stoichiometry (MC, M'C and M_2C_3) were found also, revealing that the carbides present more difficulties for the

synthesis at laboratory scale, particularly in controlling the composition (see Figure 8.1). This is related to the much more complex phase relations in the carbide phase diagrams, with the presence of MC, MC_2, and M_2C_3. For this reason, this study has been concentrated on these uranium compounds, employing the synthesis of UC with different stoichiometries by arc melting methods
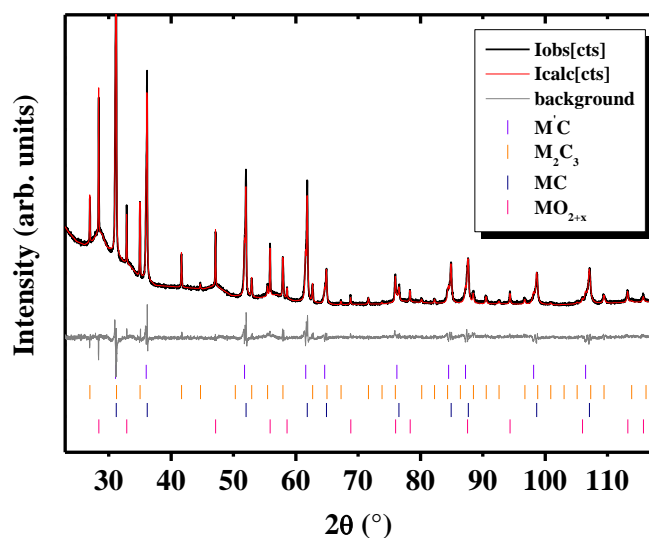

Figure 8.1: XRD pattern of the the (U,Pu,Am)C sample.

In the present thesis, the local carbon environments in $UC_{1\pm x}$ samples (0.96 ≤ "1±x" ≤ 1.04) has been investigated using a unique combination of XRD, NMR and EXAFS techniques. XRD showed an evolution of the lattice parameter with carbon content. EXAFS indicates the NaCl type structure was achieved for all compositions, distinctly excluding the ZnS structure. Also, EXAFS indicated the presence of vacancies in the C sublattice and the full occupation of the U sublattice in the $UC_{0.96}$ sample. High resolution ^{13}C MAS NMR spectra also identified two types of carbon environment in the lattice for all the as cast samples independently of the composition. The joint NMR and EXAFS study of the hyperstoichiometric samples demonstrated that the different carbon environments could be attributed to C atoms in regular octahedral lattice positions and to the excess carbon atoms, located preferentially in interstitial positions. MAS NMR proved extremely sensitive to the transition from partially disordered to ordered structures in $UC_{1\pm x}$ samples. Unfortunately, the

[235]U NMR active isotope has a low Larmor frequency and large quadrupole moment making it unfavourable for high-resolution NMR, but the recent discovery of the [239]Pu NMR signal ($I=1/2$) bodes well for an even more powerful combination of these methods.

In addition, a structural investigation of UC_2 (= $UC_{1.89 \pm 0.05}$) and U_2C_3 phases was performed using XRD, NMR and EXAFS. Whilst UC_2 could be obtained directly by arc melting, its thermal treatment was necessary to obtain the U_2C_3 phase, however, coexisting with a second phase of UC_{2-z}. EXAFS results have shown that CaC_2 and Pu_2C_3-type structures were achieved for UC_2 and U_2C_3, respectively.

8.3.   *Final remarks and outlook*

Research on the characterization of nitride and carbide fuels must be continued in the future to validate and extend the knowledge on the structural and thermal properties of these materials. This is required to ensure the safe operation of such fuel, and to predict its behaviour under irradiation. In particular, the synthesis of highest quality material is of paramount to any property study. Although, this work has been eminently successful in reaching the goals set at the outset, there is still room for improvement. The carbothermal reduction route is simple, but highest purity samples can only obtained, with a radical innovation, at least for nuclear fuels. Namely organometallic routes to precursors eliminating oxygen as a potential impurity are worthy of consideration.

Concerning the material properties, much progress has been made, but better Am bearing nitride and carbide samples are needed to address the high temperature vaporisation behaviour of these fuel forms. It is not just the margin to melt that is decisive for safe nuclear fuel operation, relocation should not occur, and if it does, it must be predictable.

These fuels are complex, but their interesting intrinsic properties provide the necessary motivation for further study.

Hoofdstuk 8

Samenvatting, conclusies en Vooruitzicheten

De resultaten van het experimenteel onderzoek verkregen in dit proefschrift tonen aan dat de synthese van americium-bevattende nitride en carbide brandstoffen haalbaar is. Dit is een belangrijke mijlpaal, aangezien deze verbindingen nooit eerder zijn gemaakt. Daarom vormen de reeks resultaten gepresenteerd in dit proefschrift een belangrijke bijdrage aan de bestaande experimentele kennis over de synthese en de karakterisering van uranium-plutonium-carbide en nitride brandstoffen. Nieuwe structuur en thermodynamische eigenschappen van deze geavanceerde brandstoffen werden eveneens bepaald.

8.1.   Nitride materialen

De geslaagde synthese van de brandstof monsters was van groot belang met betrekking tot de gedetailleerde karakterisering, hoewel een kleine hoeveelheid oxidefase aanwezig was in de (U,Pu)N monsters. De XRD, XANES en EXAFS metingen hebben aangetoond dat de synthese resulteert in vaste oplossingen. Om de studies van de kristalstructuur van de nitriden te complementeren is voor de eerste keer Raman spectroscopie aan UN en (U,Pu)N uitgevoerd. Deze metingen toonden de aanwezigheid van Raman actieve vibraties, vergelijkbaar met andere mono-nitriden. Daarnaast leverde lokale micro-Raman analyse tevens het bewijs voor de aanwezigheid van koolstof en zuurstof onzuiverheden (artefacten van de synthese en oxidatie) op onregelmatige wijze verdeeld op het oppervlak van het monster.

Gezien het belang van het hoge-temperatuur gedrag tijdens gebruik van splijtstof in de reactorkern, zijn de smelt- en stoltemperaturen van zowel UN en (U,Pu)N bestudeerd. Voor het eerst is gebruik gemaakt van een methode waarin een snelle verhitting met behulp van een laser en temperatuurmeting met behulp van een pyrometer wordt toegepast in een zogenaamde "self-crucible" methode. De overgangstemperaturen verkregen door deze onbetwist nauwkeurige techniek zijn in overeenstemming met de eerdere resultaten op basis van traditionele thermische analyse metingen. Volgens de resultaten zijn de smeltpunten van UN en $U_{0.75}Pu_{0.25}N$ respectievelijk 3120±30 K en 3045±25 K. Uit XRD metingen uitgevoerd voor en na de smeltexperimenten met de laser blijkt dat in de UN monsters nieuwe fasen zijn waargenomen na de snelle afkoeling vanuit de vloeibare toestand, terwijl dat niet het geval is voor (U,Pu)N. Dit zou kunnen betekenen dat UN incongruent smelt, en (U, Pu)N met deze samenstelling daarentegen congruent smelt.

Voor het eerst werden (U,Pu,Am)N monsters gesynthetiseerd door het koppelen van een sol-gel methode om poreuze $(U,Pu)O_2$ kogeltjes te bereiden, infiltratie van die kogeltjes met een americiumnitraat oplossing, en een carbothermisch reductie proces. Het resulterende materiaal werd gekarakteriseerd met behulp van XRD. Hoewel verdere verbeteringen nodig zijn, zijn de eerste resultaten voor de synthese van deze potentiële transmutatie brandstoffen veelbelovend.

Daarnaast is ook een studie uitgevoerd naar de schade in $U_{0.80}Pu_{0.20}N$ als gevolg van zelfbestraling gedurende 25 jaar opslag. Uit gecombineerde XRD en EXAFS metingen is gebleken dat de zelfbestraling leidt tot een lichte toename van de interatomaire roosterafstanden en uiteindelijk tot een toename van de roosterparameter van 0,3%. Uit TEM analyse is gebleken dat het nitride materiaal een goede verdraagzaamheid tegen straling vertoont, vergelijkbaar met oxiden van vergelijkbare samenstelling. De vorming van nanometrische Helium belletjes is waargenomen met TEM, zoals ook het geval is voor oxiden met vergelijkbare stralingsschade, maar weinig (ten opzichte van oxiden) twee- en driedimensionale roosterdefecten zijn waargenomen.

8.2.   *Carbide materialen*

In het kader van dit onderzoek werd de synthese van (U,Pu)C en (U,Pu,Am)C uitgevoerd, door het koppelen van externe gelering, infiltratie en carbothermische reductie, vergelijkbaar met de nitriden. Alle resultaten gaven aan dat een mengsel van meerdere fasen werd gevormd, waaronder ook een aanzienlijk deel oxide verontreinigingen. Ook werden carbiden van verschillende stoichiometrie (MC, M'C en M_2C_3) gevonden, waaruit blijkt dat de synthese van carbiden op laboratoriumschaal meer moeilijkheden met zich meebrengt, met name bij het controleren van de samenstelling (zie figuur 8.1). Dit houdt verband met de veel complexere faserelaties in de actinide-koolstof fasediagrammen, waarin de fasen MC, MC_2, en M_2C_3 allen kunnen voorkomen. Daarom is het onderzoek geconcentreerd op deze uraniumverbindingen, gebruik makend van de synthese van UC met verschillende stoichiometrie met behulp van een vlamboog methode.
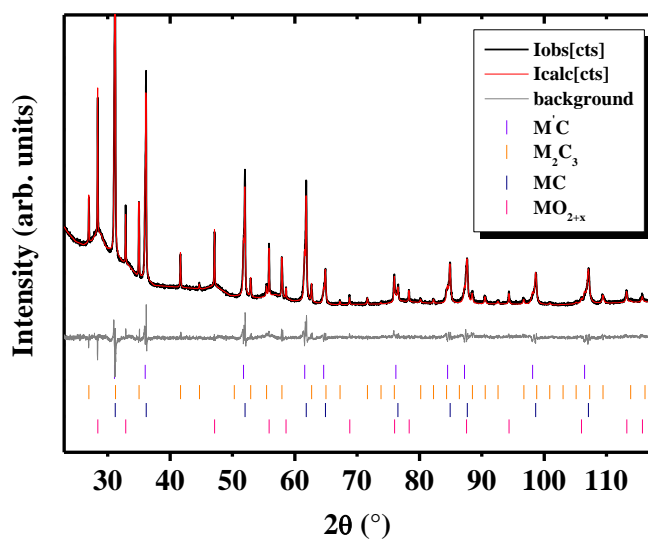
Figuur 8.1: XRD-patroon van het (U,Pu,Am)C monster.

In dit proefschrift is de lokale omgeving rondom de koolstofatomen in $UC_{1\pm x}$ monsters ($0,96 \leq$ "$1\pm x$" $\leq 1,04$) onderzocht met behulp van een unieke combinatie van XRD, NMR en EXAFS technieken. XRD metingen toonden een afhankelijkheid van de

roosterparameter en het koolstofgehalte. EXAFS metingen gaven aan dat voor alle samenstellingen het NaCl structuurtype werd verkregen, en dat de ZnS structuur eenduidig kon worden uitgesloten. Ook wees EXAFS op de aanwezigheid van vacatures in het koolstof-subrooster en de volledige bezetting van het uranium-subrooster in een $UC_{0.96}$ monster. Ook werden in hoge resolutie ^{13}C MAS NMR spectra twee soorten koolstof configuraties in het kristal rooster geïdentificeerd aan alle met de vlamboog gesynthetiseerde monsters, onafhankelijk van de samenstelling. De gecombineerde NMR en EXAFS studie van de hyperstoichiometrische monsters hebben aangetoond dat de verschillende koolstofomgevingen kunnen worden toegeschreven aan koolstofatomen op reguliere octaëder roosterposities, en exces koolstofatomen, die volgens de EXAFS analyse bij voorkeur in interstitiële posities gelokaliseerd zijn. MAS NMR bleek zeer gevoelig voor de overgang van gedeeltelijk ongeordende structuur naar een geordende structuur in $UC_{1\pm x}$ monsters. Helaas heeft de NMR actieve ^{235}U isotoop een lage Larmorfrequentie en groot quadropoolmoment en is daardoor ongeschikt voor hoge resolutie NMR, maar de recente ontdekking van het ^{239}Pu NMR-signaal ($I = 1/2$) is een goed voorteken voor de veelbelovende combinatie van deze methoden.

Bovendien werd structureel onderzoek van UC_2 (=$UC_{1.89 \pm 0,05}$) en U_2C_3 fasen uitgevoerd met XRD, NMR en EXAFS. Terwijl UC_2 direct door boogsmelten verkregen kon worden, was een thermische behandeling noodzakelijk om de U_2C_3 fase te verkrijgen, alhoewel in aanwezigheid van een tweede UC_{2-z} fase. EXAFS resultaten hebben aangetoond dat de CaC_2- en Pu_2C_3-structuur werden verkregen voor respectievelijk UC_2 en U_2C_3.

8.3. Slotopmerkingen en vooruitzichten

Onderzoek naar de karakterisering van nitride en carbide brandstoffen moet worden voortgezet in de toekomst om de beschikbare kennis over structuur en thermische eigenschappen te bevestigen en te verbreden. Meer gegevens zijn nodig om de veilige inzet van deze brandstoffen te waarborgen, en om hun gedrag tijdens bestraling te voorspellen. Vooral de synthese van materiaal van hoogste kwaliteit is van het grootste belang voor het onderzoek van materiaaleigenschappen. Hoewel het werk beschreven in dit proefschrift zeer succesvol was in het bereiken van de gestelde doelen is er nog ruimte voor verbetering. De

carbothermische reductie route is eenvoudig, maar zeer zuivere monsters kunnen alleen worden verkregen met een radicale innovatie, althans voor splijtstoffen. Voornamelijk het gebruik van organometaalcomplexen die leiden tot tussenproducten waarbij zuurstof als een potentiële onzuiverheid wordt geëlimineerd, zijn het overwegen waard.

Veel vooruitgang geboekt met betrekking tot de materiaaleigenschappen, maar betere Am-houdende nitride en carbide monsters zijn noodzakelijk om het verdampingsgedrag van deze brandstofvormen bij hoge temperaturen te bepalen. Niet alleen de marge tot smelten is bepalend voor het veilige gebruik als nucleaire brandstof, maar materiaal herverdeling mag niet voorkomen, en als het plaatsvindt, dan moet het voorspelbaar zijn.

Deze brandstoffen zijn complex, maar hun interessante intrinsieke eigenschappen leveren de nodige motivatie voor verdere studie.

Acknowledgements

I never realized how difficult a task it would be to say "thank you" for all the help, support, understanding, grief and argument given by so many people over the time it took to finish this dissertation. Simply and tritely put, I could not have done it on my own, it took a large community to help me through this thesis. But the mistakes are mine alone.

During this three years, my dissertation has always been a priority, but as most know, there are several priorities in a person,s life at any one time. Unfortunately, due to life,s challenges and the changes that followed, my dissertation could not always be the number one priority. I am very glad to say, that I have finished, and I could not have succeeded without the invaluable support of a several. Without all the supporters, I may not have gotten to where I am today!.

When I started the writing of acknowledgments, I thought…I will start chronologically, but I have to admit that one of the first person that I really would like to thank you was my (un)official supervisor, Damien. He has always there, helping unconditionally all the time, reading, re-writing and pushing me to finish this dissertation. I really appreciate his help and all the hard work that he made on this thesis. I feel, that thanks to his support, I am writing now, the acknowledgments.

I would like to express my gratitude to Rudy Konings. He found the way to solved all the administrative problems and give me the opportunity to defend the thesis in Delft. Many thanks for the constructive comments that he gave me on the thesis.

I would like to give specially thanks to Joe, who gave me the opportunity to start this project. Y solo espero, que este contento y satisfecho con el trabajo que he realizado. Nunca olvidare, "trabajo no publicado, trabajo no realizado".

I wish to thanks my supervisors during this time (yes, it is really difficult to keep one supervisor during a PhD), Matteo Rini, who believed in me to start this project and Eddie who guided me during his time at ITU. Thanks to both of you, I learnt a lot with them, and I demonstrated me that I could count on them for everything.

A warm thank to all the NF technicians and colleagues for the help in performing measurements and analysis. Especially to Co for his patience to explaining how the CTR works and to be always there for doubts and help. Thanks to the "French group" (Sarah, Anthony, Emmanuel, Patrick, and Serge) for the useful discussions we had together regarding the experimental facilities, especially related with the sol-gel. I am thankful to Herwin and Michael for their help in the lab and interpretation in the measured data.

Many thanks to Dario Manara, Thierry Wiss, Arne Janssen, Rachel Eloirdi, Tonya Vitova, who have contributed to the experimental, the writing of the publications, and the scientific discussions. Thanks you to Ian Farnan, Oliver Pauvert and L. Martel who assisted with NMR experiments),

I am thankful to the people who made possible the beamtime at ANKA (Rothe, Tonya and Katherine) and ESRF (Andrea S.). Many thanks to Emmanuel and Andrea for the good time spent in Grenoble. Also thanks to the people from ITU who made possible the preparation (thanks to Christian who made the design of the containers, Patrick and Sebastian who help with the preparation of the samples) and transport of all the samples.

Thank you Dr. Vitova and Prof. Dr. H.Geckeis, I will always remember with pleasure your help to find a solution with the problem of the university at the end of my thesis.

A warm thank you to the secretaries of the two departments, Anna (ITU) and Ine (TU Delft) for the help, patience and assistance concerning all the administrative issues.

Raquel, que empezó siendo "mi compañera de oficina" para convertirse en una gran amiga y confidente, con la que he compartido tanto lloros como risas. Gracias a ella, siento, que muchos de los problemas personales, familiares y profesionales se hicieron mucho mas llevaderos tanto dentro como fuera de la oficina.

Los "neiborjud" Rosa y Ernesto, que tanto para lo bueno y lo malo han sido un gran apoyo tanto personal como profesional.

Carmencita, Ivana e Simona, ho preso due amici, dentro e fuori del lavoro.

Muchas gracias a la gente que he conocido fuera o en ITU y me han aportado mucho (Johnny, Sylvain, Mattia, Doroteya, Valentino, Zeynep, Peter and Doris). Especialmente, gracias al apoyo de Maria I., y a las largas conversaciones que hemos tenido, siento que he crecido personal y profesionalmente.

Especial agradecimiento a los amigos que han estado ahí durante este tiempo y de alguna manera me han ayudado a seguir con esto adelante, han sido un gran apoyo. Especialmente a Isi, Jose, Patri, Elisa y Maria V.

Expreso mi gran agradecimiento a mi familia y mis hermanas, sin duda, fundamental para haber podido llevar esto adelante, que a pesar de los problemas, he sentido su incondicional apoyo.

Enfin, je tiens à remercier Alexis, ton soutien, ta patience et d'être là a fait beaucoup plus facile à terminer cette thèse!.

With the experience during this time, I learnt that it is better not plan everything, never decide the future, because when you look back, you realize that the way that you have left is far from the plan that you made at the beginning.

"Caminante no hay camino, se hace camino al andar" (Antonio Machado).

Curriculum vitae

EDUCATION

2010-2014   **PhD in Synthesis and Characterization of Advanced Nuclear Fuels.** The research was performed at the European Commission, Institute for Transuranium Elements, Germany.

2007-2009   **MSc in Materials Engineering**- Complutense University of Madrid, Spain.

2003-2007   **BSc in Chemistry** – Complutense University of Madrid, Spain**.**

PUBLICATIONS

Publications   **1.-U. Carvajal-Nuñez** et al**.** Melting Point Determination of Uranium Nitride and Uranium Plutonium Nitride: a Laser Heating Study, Journal of Nuclear Materials, in press, 2014.

2.-U. Carvajal-Nuñez et al., Structure of UC_2 and U_2C_3: XRD, ^{13}C NMR and EXAFS study, Journal of Alloys and Compounds, 589 (2014) 234-239.

3.-U. Carvajal-Nunez et al., Chemical and structural characterization of uranium nitride produced by external gelation. Journal of Nuclear Materials submitted, 2013.

4.-U. Carvajal-Nunez et al.,The high-temperature behaviour of nitride nuclear fuels: a laser heating characterization, Journal of Nuclear Materials, accepted, 2013.

5.-U. Carvajal-Nunez et al., Preparation and Characterization of (U,Pu)N and (U,Pu,Am)N, Journal of Nuclear Materials, accepted, 2014.

6.-U. Carvajal-Nunez et al., Characterization of self-damaged (U,Pu)N fuel used in the NIMPHE program, Journal of Nuclear Materials, (2013), 443, pp 491-496.

7.-U. Carvajal-Nunez et al., Coupling EXAFS and 13C NMR to study the effect of carbon content on the local structure of $UC_{1\pm x}$. Inorganic

Chemistry, 2013, 52 (19), 11669–11676

8.-U. Carvajal-Nunez et al., Charge distribution and local structure of Am bearing thorium oxide solid solutions, Inorganic Chemistry 51 (2012) 11762-11768.

9.-D. Prieur, **U. Carvajal-Nunez** et al., Charge distribution and local structure of Am bearing PuO_2, European Journal of Inorganic Chemistry, 9 (2013)1518–1524

10.-D. Prieur, **U. Carvajal-Nunez** et al., O/M determination and oxidation behaviour of Am bearing ThO_2 solid solution, Journal of Nuclear Materials 435(2013)49-51

Conferences proceeding **11.-U. Carvajal-Nunez** et al., Safety in the synthesis of nitride and carbide fuels. Transactions of the American Nuclear Society. American Nuclear Society-Annual Meeting 2012, Chicago, IL.

PROFESSIONAL EXPERIENCES

September 2010-June 2014 **PhD thesis:** *Synthesis and Characterization of Nuclear Advanced fuels.* European Comission, Joint Research Centre, Institute for Transuranium Elements. Germany ((JRC-ITU).

October 2009-March 2010 **Trainee:** *Coated particles fuel fabrication for HTR reactors*. European Comission ,Joint Research Centre, Institute for Transuranium Elements, Germany (JRC-ITU).

April 2010 – August 2010 **Trainee:** *Safety on synthesis of nitrides and carbides fuels*. European Commission, Joint Research Centre, Institute for Transuranium Elements, (JRC-ITU), Germany.